Study on Metal Oxide Nanomaterials for Automotive Catalysts(Dissertation_全文)

AUTHOR(S):

Imagawa, Haruo

Study on Metal Oxide Nanomaterials for Automotive Catalysts

HARUO IMAGAWA

2012

Preface

Over the past 100 years, automobiles have become one of the main means of transportation all over the world, and the number of automobiles is still increasing, especially in developing countries. Although the convenience brought about by automobiles is well understood, several negative impacts of the widespread use of automobiles have become apparent. Two serious issues are the emission of poisonous gases, such as carbon monoxide, hydrocarbons and nitrogen oxides (NO_x), from combustion engines, which causes air pollution, and the emission of carbon dioxide (CO_2) by the large consumption of limited fossil resources, which causes global warming.

Automotive catalysis is one of the most successful applications of catalysts in industry, which has resulted in the successful removal of poisonous exhaust gases. Catalysts that are active for the removal of NO_x have also contributed to a reduction of CO_2 emissions when used with lean-burn gasoline or diesel engine systems. However, more severe regulations on the emission of both exhaust gases and CO_2 still require technological improvements based on the current catalysts, and further innovation inspired by different research fields. Recent advances in the nanoscale synthesis of metals and metal compounds have affected not only academia, but also industry. As downsized electronic storage devices have completely changed our lifestyle with the advent of nanoscale technology, the nanoscale control of catalyst components in chemical synthesis has the potential to significantly change the performance of catalysts due to their size effects. The current research project was determined on the basis of this background.

Here, the author presents a study on metal oxide nanomaterials for automotive catalyst application. The controlled synthesis of a homogenous mixture of multi-metal

oxides and highly dispersed nanoparticles was accomplished, which is expected to result in novel advances in automobile catalysts.

The present study was conducted in a catalyst laboratory at Toyota Central Research and Development Laboratories Inc. (TCRDL) from 2000 to 2007, and in a nanoscale materials laboratory at Brown University from 2008 to 2010. From the viewpoint of material synthesis on the nanoscale, the author has engaged in studies on the synthesis of metal oxide nanocomposites for NO_x storage and reduction catalysts at TCRDL, and also on the synthesis of metal oxide nanoparticles for O_2 storage and release at Brown University.

The author would like to thank his supervisors, Professor Tsunehiro Tanaka at Kyoto University, Dr. Hirofumi Shinjoh at TCRDL, and Professor Shouheng Sun at Brown University, for their valuable advice and suggestions, and for the opportunity to undertake the research. The author would like to express special thanks to Professor Tanaka for his useful discussions and comments regarding the present thesis, publication and manuscript.

The author would also like to express his gratitude to Professor Satohiro Yoshida and Professor Takuzo Funabiki for providing the required basic knowledge and skills during his undergraduate and graduate research at Kyoto University. The author acquired an academic curiosity at Kyoto University that has led to his current attitude toward research at TCRDL.

The author would like to express his appreciation to his managers, Dr. Masaya Kawasumi, Mr. Takahiko Asaoka, Dr. Tohru Shiga, and Mr. Hideo Sobukawa, and to his co-workers, Dr. Naoki Takahashi, Dr. Akihiko Suda, Mr. Shin'ich Matsunaga, Mr. Toshiyuki Tanaka, Dr. Yasutaka Nagai, and Mrs. Kae Yamamura, for their helpful discussions and collaboration in the research at TCRDL. The author would like to offer

special thanks to Dr. Takahashi and Dr. Nagai for their advice on the preparation of the present thesis. The author would also like to express his appreciation to the catalyst group members, Dr. Jaemin Kim, Dr. U-Hang Lee, Dr. Youngmin Lee, Dr. Mazmudar Vishmadeb, Dr. Tetsunori Koda, and Mr. Anthony McCormick, for their interesting discussions and collaboration in the research at Brown University.

Finally, the author would like to offer his heartfelt gratitude to his parents, Eiichi and Chiyoko, for their sincere support.

Haruo Imagawa

Aichi,

February, 2012

- CONTENTS –

Chapter 1: General introduction……..……...……-1-

Part I: Nanocomposite of Al_2O_3 and ZrO_2-TiO_2 (AZT) as a support for NO_x storage reduction catalyst

Chapter 2: Synthesis and characterization of AZT and its application as a support for NO_x storage reduction catalyst…….…….…..….-19-

Chapter 3: Analysis of NO_x storage materials on AZT for thermal stability and sulfur durability…….…….-39-

Chapter 4: The effect of titanium-doping in AZT on sulfur durability for NO_x storage reduction catalyst…….…….…..-63-

Part II: CeO_2 nanostructure formation for O_2 storage and release

Chapter 5: Synthesis of monodisperse CeO_2 nanoparticles and their application to O_2 storage and release……..……...-87-

Chapter 6: Controlled synthesis of monodisperse CeO_2 nanoplates and nanorods ……..……...…-105-

Chapter 7: General Conclusions...…….…….…..-129-

List of publications...……..…….....-137-

Chapter 1

General Introduction

1. General background of automotive catalysts

Since automobiles appeared in the late 19th century, they have used as one of the main transportation systems all over the world, and no one denies the convenience of automobiles. On the other hand, negative impacts such as poisonous exhaust gases, carbon dioxide (CO_2) emission, and huge energy consumption have been focused on and discussed for a long time. The emission of poisonous exhaust gases has been an issue since 1960s, especially in the city area both in Japan and the United States of America (USA). One specific phenomenon caused by the exhaust gases is a photo synthetic reaction of ozone originated from nitrogen oxide species (NO_x), which resulted in the sudden headache and shock symptom. In order to overcome such a situation, first emission regulation called Muskie Act was proposed in the USA, and similar regulation was also enacted soon in Japan in the late 1970s, and lately in Europe in the mid 1980s. Table 1 shows the exhaust emission standards for passenger cars in the USA, Japan and the European Union (EU). Hydrocarbon (HC), carbon monoxide (CO) and NO_x are usually designated as poisonous exhaust gas species in the emission control. Under ideal condition, products after combustion should be CO_2, H_2O and N_2. But real exhaust gases contain a mixture of HC from the residual uncombusted gasoline, CO from the partial combustion product, and NO_x from the reaction of N_2 with O_2 in the engine cylinder at combustion temperature. From the ideal point of view,

Table 1. Emission standards in the USA, Japan and EU.

Federal standards in the USA

Effective year	HC (g/km)	CO (g/km)	NOx (g/km)
1968	6.63	5.25	2.56
1981	0.25	2.13	0.63
1994	0.16	2.13	0.25
2004	0.06	2.62	0.04

Japanese standards

Effective year	HC (g/km)	CO (g/km)	NOx (g/km)
1973	18.4	2.94	2.18
1978	0.25	2.10	0.25
2000	0.08	0.67	0.08
2005	0.05	1.15	0.05

EU standards

Effective year	HC (g/km)	CO (g/km)	NOx (g/km)
1992	1.13	3.16	-
1996	0.50	2.20	-
2005	0.10	1.00	0.08

HC and CO should be oxidized to CO_2 and H_2O, whereas NO_x reduced to N_2 and O_2. In the early stage of the emission control, many devices such as the arrangement of combustion system, exhaust gas recirculation system and fuel reforming were developed. But those mechanical orientated trials were not able to become a decisive technology, mainly due to the difficulty in the reduction of different type of gases, mixture of reductive gases and oxidative one, at a time. First catalyst as a feedback from chemistry was an oxidation catalyst for the removal of HC and CO. Second generation of automotive catalysts is called the three-way catalyst (TWC), which is the most common technology for the automobile emission control today. Figure 1 is an overview

of automotive catalyst. Such catalysts are usually equipped under the floor of automobiles, and connected to the exhaust pipe from engine to muffler. Catalytic converter is mainly composed of monolithic honeycomb substrates made of cordierite ($2MgO\text{-}2\ Al_2O_3\text{-}5\ SiO_2$) or metals (stainless steel) and catalysts coating on the monolithic wall. TWC is able to reduce NO_x as well as HC and CO at once. Most of current practical automotive catalysts are based on the TWC technology, and further development for the reduction of poisonous gases has been needed still now, because of more strict regulations for global environment protection.

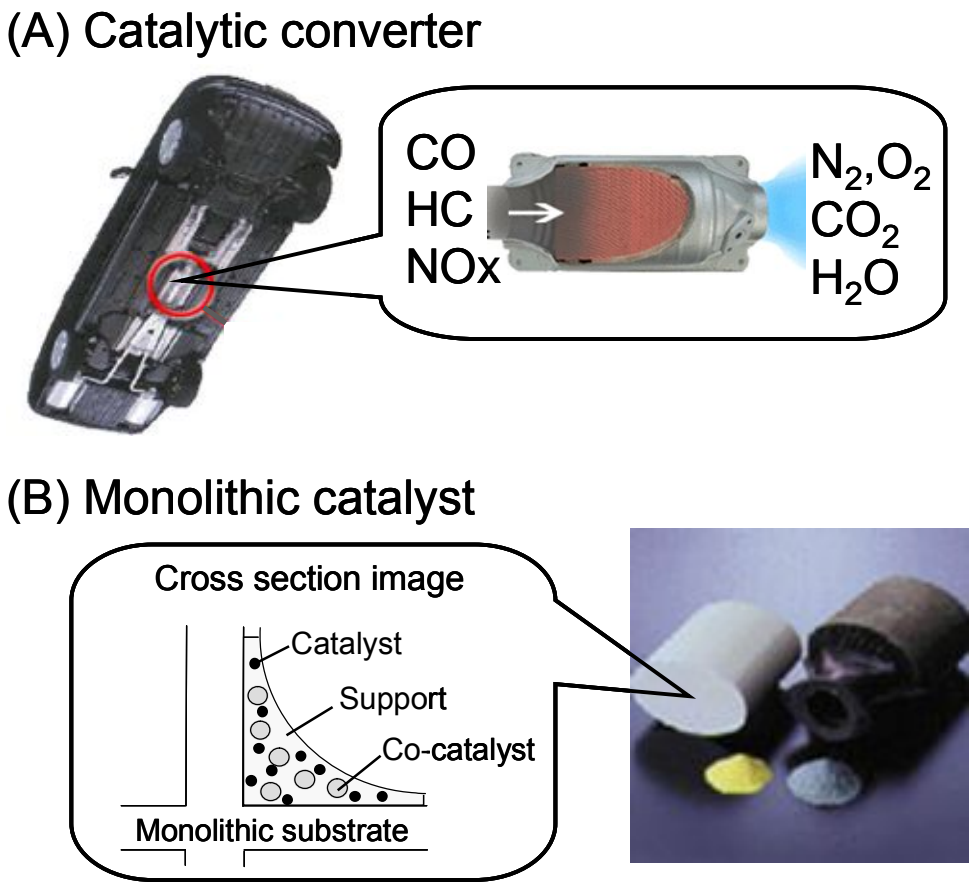

Fig.1. Overviews of (A) an automotive catalytic converter and (B) a monolithic automotive catalyst.

Table 1 also shows the current standards in the USA, Japan and the EU. Especially in Japan, the current upper limit of both HC and NOx is almost 1/5 of the standard in 1978 and is decreasing further compared to that of the standards in 2000. Therefore, automobile companies and related institutions have been working aggressively on the development of catalysts, and the improvement based on new concepts has been expected continuously.

In the following section, detailed function of automotive catalysts for gasoline fueled engines is shown according to the difference of air to fuel ratio (A/F ratio) in combustion. Application of nanomaterials to automotive catalysts is also touched upon, and some of the helpful aspects are shown along with this thesis," metal oxide nanomaterials" for the novel improvement of automotive catalysts using precise morphology control.

2. Automotive catalysts for stoichiometric A/F ratio: three way catalyst

Figure 2 shows concentrations of CO, HC, NO_x, CO_2 and O_2. Composition of exhaust gases depends on A/F ratio. In the fuel rich condition (A/F<14.6), CO and HC are the dominant species. On the other hand in the fuel lean condition (A/F>14.6), NO_x become the dominant gas. The TWCs remove such gases under the following reactions.

1) Oxidation of CO: $CO + 1/2\ O_2 \rightarrow CO_2$

2) Oxidation of HC: $CaHb + O_2 \rightarrow aCO_2 + b/2\ H_2O$

3) Reduction of NO_x: $NO_x \rightarrow 1/2\ N_2 + x/2\ O_2$

Total three way reaction:

$$NO_x + CO \rightarrow CO_2 + 1/2\ N_2$$

$$NO_x + CaHb \rightarrow aCO_2 + b/2\ H_2O + 1/2\ N_2$$

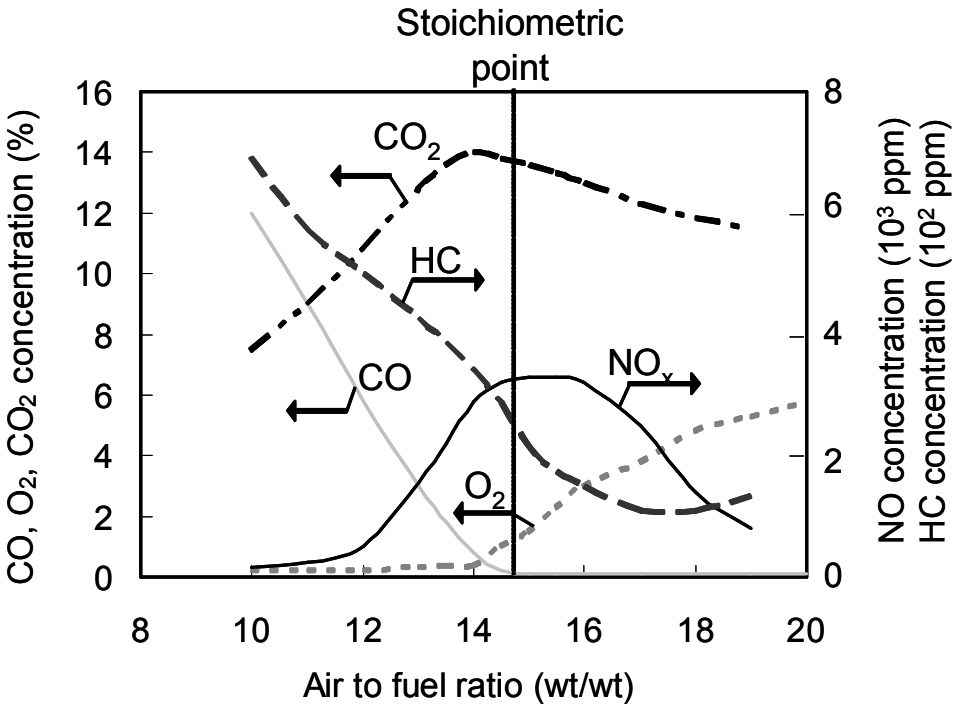

Fig.2. Typical concentrations of CO, NO_x, HC, CO_2 and O_2 from gasoline engine as a function of air to fuel ratio.

Precious metals such as platinum (Pt), rhodium (Rh) and palladium (Pd) are often selected as catalysts, and thermally stable metal oxides such as aluminum oxide (Al_2O_3) are used as supports. Such components are mixed and wash-coated on the monolithic substrate as shown in Fig. 1B. The light off temperature of TWC reaction is around 150 – 200 °C, and the TWCs are usually exposed from 300 °C at engine idling state to 800 °C at engine running state [1].

The performance of the TWC is strongly affected by A/F. Figure 3 shows the typical catalytic efficiency as a function of A/F ratio. The TWCs reduce all kinds of

exhaust gases under the stoichiometric condition (A/F=14.6). Therefore, precise A/F ratio control is indispensable in order to keep the stoichiometric condition. Figure 4 shows the outline of the TWC system including electronic devices. O_2 concentration after passing the catalyst depends on the A/F ratio. For example, O_2 concentration is large at less than the stoichiometric point, and small at more than that point, which becomes a good indicator for A/F ratio. That is why O_2 concentration is monitored using O_2 sensor such as zirconium oxide or cerium oxide based ceramics, and A/F ratio is controlled in combustion owing to the computer aided feedback system. Figure 5 exhibits the effect of the feedback control on total NO_x and CO emissions during the Japanese 10 mode exhaust test. Both NO_x and CO emission amounts decrease owing to TWC, and the trend is enhanced with the combination of TWC and the feedback control system.

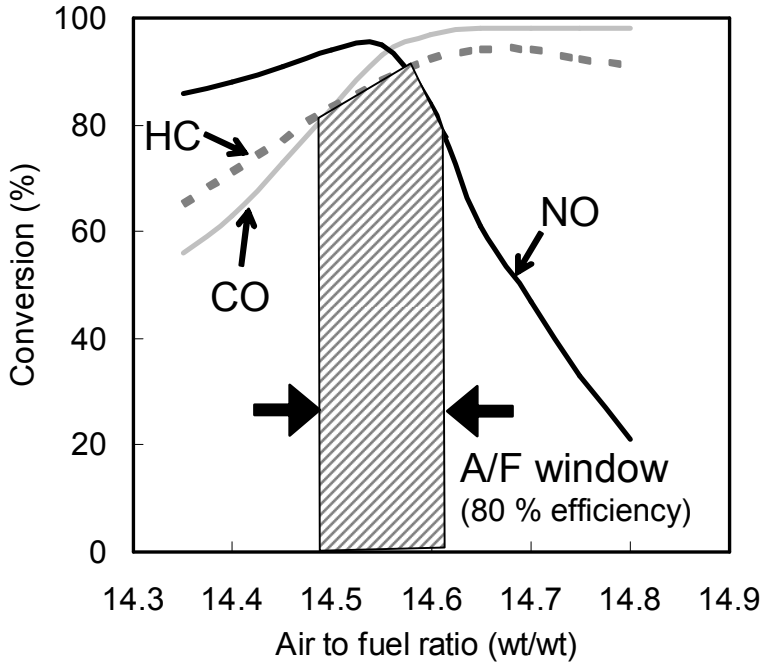

Fig.3. Removal efficiency of TWC as a function of air to fuel ratio.

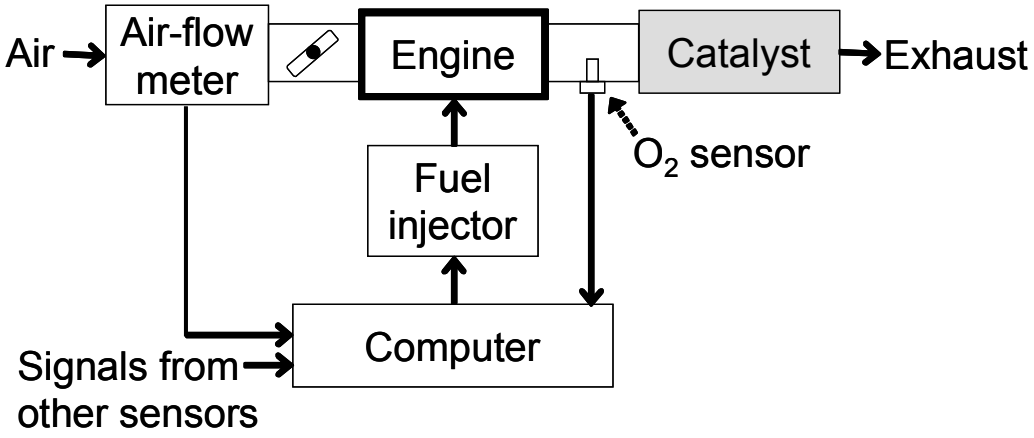

Fig.4. Typical TWC system with electronic feedback control devices.

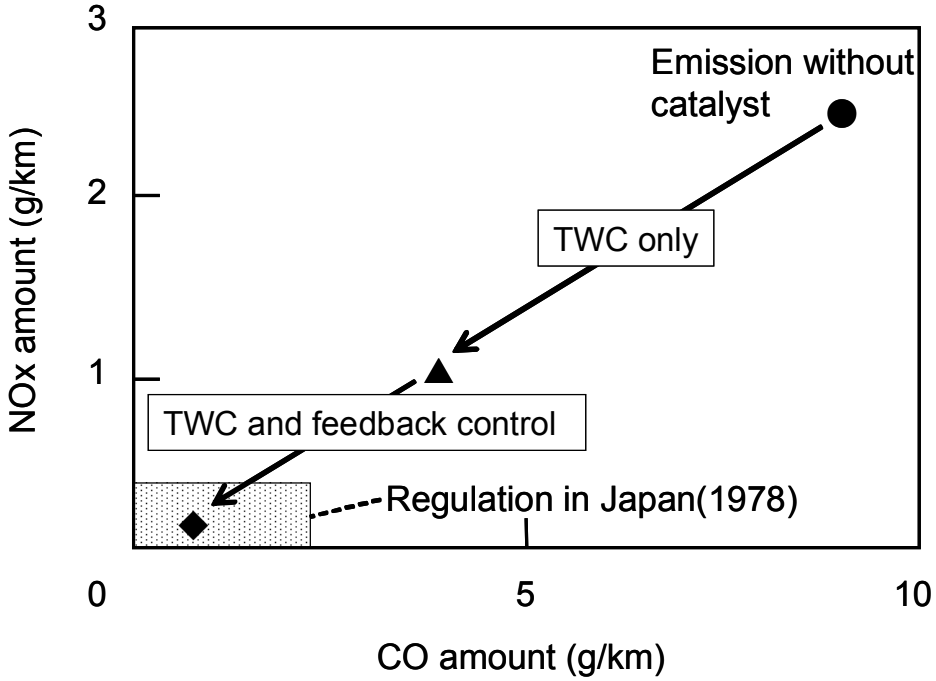

Fig.5. NO_x and CO amounts in Japanese 10 mode emission; (●) without TWC, (▲) with TWC without feedback control, and (◆) with TWC and feedback control.

But the A/F ratio is continuously fluctuated in spite of the feedback system. In such a case, cerium oxide (CeO_2) has been used as a co-catalyst for O_2 storage and release reaction [2]. Cerium atoms in cerium oxide can easily redox between Ce^{3+} and Ce^{4+} according to atmosphere, because CeO_2 is one of the non-stoichiometric oxides. The reversible reaction is shown as follows,

$$CeO_2 \leftrightarrow CeO_{2-x} + x/2O_2, \quad x = 0 - 0.5$$

Under slightly lean A/F condition, CeO_2 releases O_2 to atmosphere, and under slightly rich A/F condition, CeO_2 stores O_2. Therefore, O_2 concentration is held at around A/F = 14.6 owing to the inhibition of the fluctuation of O_2 concentration, which enables to enlarge the A/F window of raw exhaust gases and leads to improve the catalytic performance.

O_2 storage and release function in CeO_2 is known to be enhanced with the addition of ZrO_2 or other metal oxides as a solid solution [3]. The size of Zr^{4+} ion is larger than that of Ce^{4+} ion, which expands the pathway of oxygen atoms in lattice and facilitates O_2 storage and release reaction. In addition to other metal doping as a solid solution, crystal structure also has been known to effect on O_2 storage and release reaction. For example, κ-CeO_2-ZrO_2 synthesized from $Ce_2Zr_2O_{7+\delta}$ with pyrochlore-type structure shows larger O_2 storage and release capacity (OSC) than other CeO_2 crystal structure due to the ordered arrangement of Ce and Zr ions [4], although the surface area of κ-CeO_2-ZrO_2 is smaller than that of others. Therefore, both the additives and the structure of OSC materials are closely related to O_2 storage and release reaction.

3. Automotive catalysts for lean A/F ratio: NO_x storage and reduction catalysts

The reduction of CO_2 from combustion engines is urgently necessary for the global environmental protection. One of the best ways to reduce the fuel consumption is the combustion under lean A/F condition. Figure 6 shows the fuel consumption as a function of A/F ratio. The fuel consumption decreases with the increase of A/F ratio, which corresponds to the almost 10 % of reduction of fuel consumption. In terms of the engine management, A/F ratio from 15 to 30 is preferable for keeping suitable torque in running. But the main exhaust gas is NO_x under lean A/F condition (A/F > 14.6) as shown in Fig. 2. In such a situation, it is difficult to reduce NO_x alone using the TWC, because the TWC works at around A/F = 14.6 with the coexistence of CO and HC as reducing agents for NO_x.

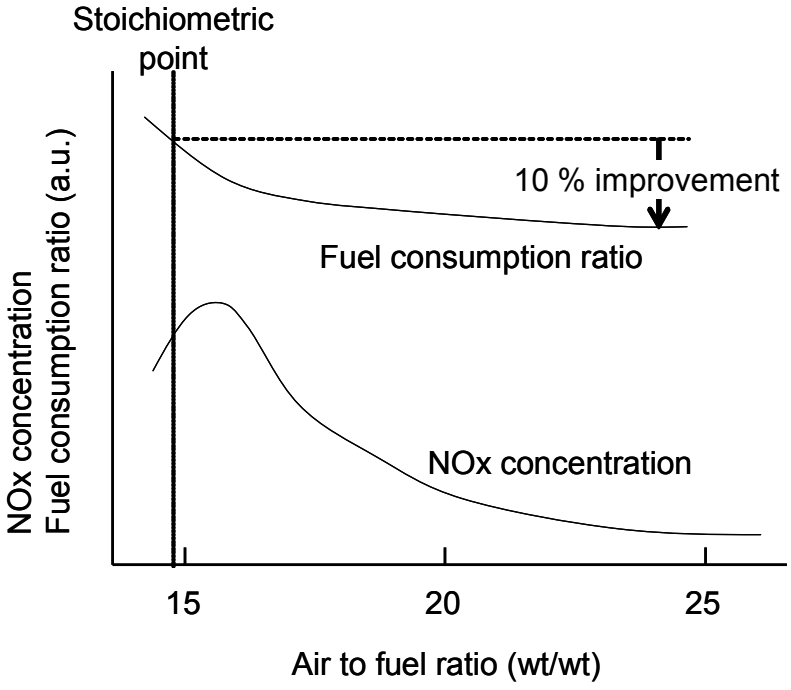

Fig.6. NO_x concentration and fuel consumption rate as a function of air to fuel ratio.

A number of catalyst systems such as direct NO_x decomposition using Cu/ZSM-5 [5], H-zeolite [6] or Al_2O_3 catalysts [7], and a variety of NO_x selective catalytic reduction (NO_x-SCR) with reducing agents has been researched. Direct NO_x decomposition is one of the most attractive and ideal methods for the NO_x reduction under the lean A/F condition. But the system has been under investigating for a long time and not been commercialized, mainly due to the deactivation with the coexistence of O_2 and the poor thermal stability. The NO_x-SCR has been also well studied and applied to commercialized automobiles with diesel engine. But the reducing agents, which is mainly urea, need to be stored in a tank and supplied at once a twice or three times of gas charge (3-5 vol % of consumed fuel). Therefore, the NO_x-SCR is applied to large-sized vehicles with large spare space, and there is difficulty in the application to passenger cars.

NO_x storage-reduction (NSR) catalyst is another solution for the reduction of NO_x under the lean A/F condition. This system was developed and commercialized for use in lean-burn engine systems by Toyota in 1994 [8,9]. The NSR catalyst is composed of precious metals as catalysts, alkaline and alkaline earth metal compounds as the NO_x storage materials, and metal oxides as the support. The reaction mechanism of the NSR catalyst is shown in Fig. 7. Firstly, during the lean A/F condition, excess NO_x is oxidized to NO_2 on the precious metals and stored in the form of nitrate in storage materials. Secondly, when the engine condition is switched to the operation of rich or stoichiometric A/F ratio, nitrate stored in storage material is reduced to N_2 by hydrogen (H_2), CO, and HC. That is why NSR catalyst has become the solution for the reduction both of fuel consumption as energy source and of NO_x emission as exhaust gas.

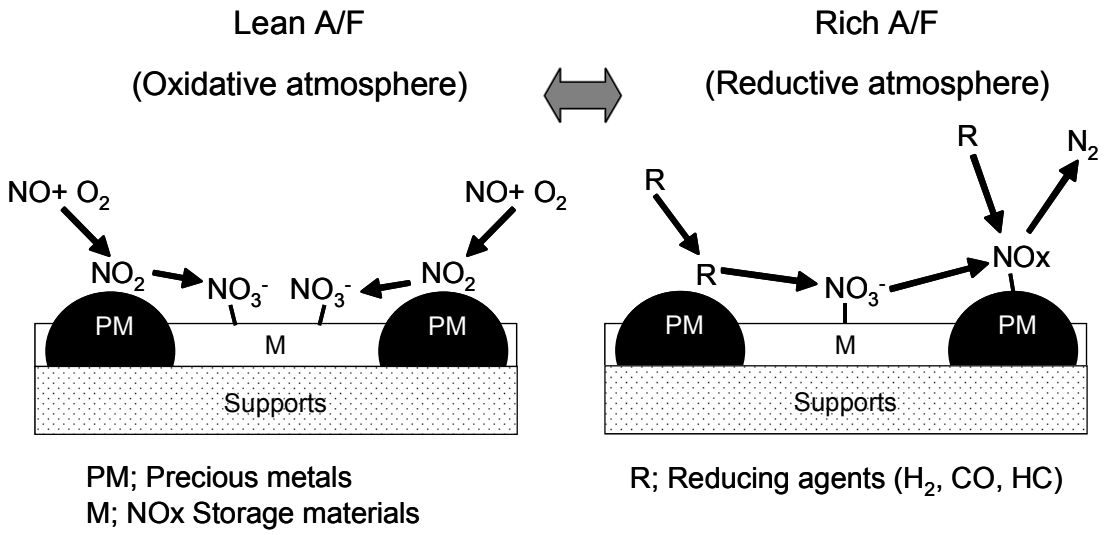

Fig. 7. The mechanism of NO_x storage reduction catalyst.

Although the NSR catalyst must be a convenient solution for the NO_x reduction, this catalyst has two main technical problems; one is sulfur poisoning and the other is thermal deterioration. Sulfur dioxide (SO_2) is derived from the combustion of sulfur compounds in fuel. SO_2 reacts with storage materials and formed sulfate. Therefore, NO_x cannot be stored in the storage materials sufficiently. But these days, in studies of sulfur durability, TiO_2 in supports has been found to be high tolerance against sulfur poisoning because of its high acidity [10]. The thermal deterioration results from the reaction of NO_x storage materials with supports and aggregation and sintering of support materials with deactivation of precious metals and NO_x storage materials. ZrO_2 has been added as ZrO_2-TiO_2 solid solution to avoid the reaction of TiO_2 with storage materials by heat [11]. Recently, the suitable composition of ZrO_2-TiO_2 on durability was examined, and ZrO_2-TiO_2 has been found to inhibit the formation of sulfate and

solid-phase reaction of storage material [12,13]. For the total improvement against heat, the NSR catalysts also contain thermally stable γ-Al_2O_3 as a main support.

4. Application of nanomaterials with controlled synthesis for automotive catalysts

These days, catalysts and catalyst supports are designed on the nanoscale owing to a variety of novel synthesis approach and analytical methods. At the beginning of the automotive catalysts history, catalysts, mainly TWC, had a simple structure such as merely the mixture of one kind of precious metal as catalyst and powder as catalyst support. But demands for the upcoming exhaust regulation require more improved catalysts, which brought both catalysts and supports with several elements mixture. For example, the current TWCs contain precious metals such as Pt, Rh and/or Pd (sometimes Ni), and catalyst supports like Al_2O_3, CeO_2-ZrO_2, and so on. Components were usually physical mixture of several powders, or were obtained by simple annealing of immersing powder to precious metal solution. Therefore, automotive catalysts have been also studied in nanoscale, owing to the development of nanotechnology in catalysts based on the precise morphology control for nanoparticles and nanocomposites. Bimetallic and trimetallic precious metal catalysts as nanoparticles have often studied well.

Regarding catalyst supports, nanocomposite of thermally stable Al_2O_3 and CeO_2-ZrO_2 as an OSC material has been developed [11,14]. Sintering of CeO_2-ZrO_2 was inhibited with higher specific surface area relative to CeO_2-ZrO_2 without Al_2O_3, which lead the fast O_2 release rate especially after durability test at high temperature.

Core-shell structure of CeO_2 and Ag as a complex of catalysts and catalyst support is also interesting approach for improving catalysts on the nanoscale [15,16].

The CeO_2-Ag complex was fabricated by a one-pot selective redox reaction using cerium(III) and silver(I) autocatalyzed by silver metal without surfactants or organic compounds. The nanostructure is unique and suitable as a catalyst for carbon oxidation in diesel-engine emission due to the combination of closely located CeO_2 and Ag.

5. Scope of this thesis

The main topic in this thesis is the development of automotive catalysts with new approach owing to controlled morphology of metal oxides on the nanoscale. This thesis consists of two main parts. In Part I, from Chapter 2 to 4, novel nanocomposite of Al_2O_3 and ZrO_2-TiO_2 (AZT) is characterized, and its application as a support for NSR catalysts is discussed. Al_2O_3, ZrO_2 and TiO_2 are important materials for NSR catalyst as support components as shown in the previous section. But they were only physically mixed powder of each metal oxide in the conventional NSR catalysts, and it was expected that the nanoscale mixture of their primary particles will bring more enhanced performance both in terms of thermal stability owing to Al_2O_3 and ZrO_2 and sulfur durability derived from TiO_2 due to their homogeneous distribution.

In Chapter 2, the author writes the synthesis of AZT with detailed characterization and evaluation as a NSR catalyst support. Nanocomposite of Al_2O_3 primary particles and ZrO_2-TiO_2 primary particles is synthesized by coprecipitation method, and the sintering behavior of ZrO_2-TiO_2 based on the diffusion barrier created by primary Al_2O_3 is investigated after thermal aging. Such structural advantage of AZT is expected to have a large NO_x storage capacity relative to the physically mixed oxide support after aging.

Chapter 3 is written for the clarification of the reason why AZT support shows

excellent NSR performance, based on the analysis of NO_x storage materials. NO_x storage materials such as potassium and barium complexes are often poisoned because of thermal deterioration and sulfur poisoning. Thermal stress affects potassium compound caused by the solid phase reaction with support materials such as TiO_2, and SO_2 mainly deactivates barium compounds because of the $BaSO_4$ formation. Therefore, it is possible to clarify factors for thermal stability and sulfur durability, which leads to the optimization of the synthesis method of AZT for the increased NSR performance.

The author also explains the effect of titanium-doping in Al_2O_3 of AZT for improved sulfur durability in Chapter 4. Original AZT is synthesized mainly for thermal stability based on diffusion barrier of Al_2O_3. But the detailed characterization and experimental data clarified the high sulfur durability of AZT due to low basicity from the presence of TiO_2 in Al_2O_3. This trend of AZT is expected to be enhanced using titanium-doping in Al_2O_3 synthesized by impregnating AZT into titanium citrate solution with following annealing step.

In the Part II, from Chapter 5 to 6, the author discusses the synthesis of monodispersed CeO_2 nanostructures such as nanoparticles, nanorods and nanoplates. CeO_2 is known as an important O_2 storage material for TWCs as written in the previous section. O_2 storage and release property often depends on the primary particle size and its crystal phase, according to CeO_2 powder synthesized using conventional synthesis methods. In order to synthesize monodisperse primary particles, thermal decomposition of metal complexes in organic solvent with organic surfactants becomes one of the powerful tools, because of precise control of particle size and crystal phase. Monodispersed nanoparticles can be used not only for building blocks of powders, but also for highly dispersed catalysts or co-catalysts on supports.

In Chapter 5, the author shows the synthesis of two different sizes of

monodispersed CeO_2 nanoparticles synthesized by thermal decomposition of cerium(IV) salt in an organic solvent using surfactants. CeO_2 nanoparticles are expected to disperse homogeneously on γ-Al_2O_3 without aggregation, owing to their monodispersity, which will lead to excellent O_2 storage and release performance.

Finally, the author exhibits synthesis of monodisperse CeO_2 nanoplates and nanorods in Chapter 6. CeO_2 nanoplates and nanorods have specific phase, (100) of cubic fluorite CeO_2 structure, by the thermal decomposition of cerium(III) salts in organic solvent with surfactants. The mechanism of CeO_2 nanostructures formation is discussed especially based on the effect of surfactants on their morphologies.

References

[1] C. K. Narula, J. E. Allison, D. R. Bauer and H. S. Gandhi, *Chem. Mater.* 8 (1996) 984.

[2] H.S.Gandhi, A.G.Piken, M.Selef, R.G.Delesh, *SAE Paper* (1976) 76021.

[3] M. Ozawa, M. Kimura, A. Isogai, *J. Alloys Compd.* 193（1993）73.

[4] Y. Nagai, T Yamamoto, T. Tanaka, S. Yoshida, T. Nonaka, T. Okamoto, A. Suda, M. Sugiura, *Catal. Today* 74 (2002) 225.

[5] M. Iwamoto, H. Yahiro, Y. Mine, S. Kagawa, *Chem. Lett.* (1989) 273

[6] Y. Kintaichi, H. Hamada, M. Tabata, M. Sasaki, T. Ito, *Catal. Lett.* 6 (1990) 239.

[7] H. Hamada, Y. Kintaichi, M. Sasaki, T. Ito, M. Tabata, *Appl. Catal.* 70 (1991) L1.

[8] N. Miyoshi, S. Matsumoto, K. Katoh, T. Tanaka, J. Harada, N. Takahashi, K. Yokota, M. Sugiura, K. Kasahara, *SAE Paper* (1995) 950809.

[9] N. Takahashi, H. Shinjoh, T. Iijima, T. Suzuki, K. Yamazaki, K. Yokota, H. Suzuki, N. Miyoshi, S. Matsumoto, T. Tanizawa, T. Tanaka, S. Tateishi, K. Kasahara, *Catal. Today* 27 (1996) 63.

[10] S. Matsumoto, Y. Ikeda, H. Suzuki, M. Ogai, N. Miyoshi, *Appl. Catal. B: Environ.* 25 (2000) 115.

[11] T. Kanazawa, *Catal. Today* 96 (2004) 171.

[12] N. Takahashi, A. Suda, I. Hachisuka, M. Sugiura, H. Sobukawa, H. Shinjoh, *Appl. Catal. B: Environ.* 72 (2006) 187.

[13] I. Hachisuka, T. Yoshida, H. Ueno, N. Takahashi, A. Suda, S. Sugiura, *SAE paper* (2002) 2002-01-0732.

[14] A. Morikawa, T. Suzuki, T. Kanazawa, K. Kikuta, A. Suda, H. Shinjoh, *Appl. Catal. B: Environ.* 78 (2008) 210.

[15] T. Kayama, K. Yamazaki, H. Shinjoh, *J. Am. Chem. Soc.* 132 (2010) 13154.

[16] K. Yamazaki, T. Kayama, F. Dong, H. Shinjoh, *J. Catal.* 282 (2011) 289.

Part I

Nanocomposite of Al_2O_3 and ZrO_2-TiO_2 (AZT) as a support for NO_x storage reduction catalyst

Chapter 2

Synthesis and characterization of AZT and its application as a support for NO_x storage reduction catalyst

Abstract

To improve the thermal stability of NO_x storage reduction catalysts, a novel support containing Al_2O_3, ZrO_2, and TiO_2 was synthesized by the coprecipitation method. The XRD and TEM results indicated that primary particles of γ-Al_2O_3 and a solid solution of ZrO_2-TiO_2 coexisted as secondary particles, that is, the synthesized support was a nanocomposite of γ-Al_2O_3 and ZrO_2-TiO_2 (AZT). AZT had a characteristic single meso-pore, derived from the structure of the secondary particle. The basicity of AZT was lower than that of the physically mixed oxide. After thermal treatment, aggregation of the ZrO_2-TiO_2 particles in the support was inhibited relative to that in the mixture of Al_2O_3 powder and ZrO_2-TiO_2 powder. This was attributed to the diffusion barrier (against ZrO_2-TiO_2) created by primary Al_2O_3 in AZT. After a thermal aging test, the NO_x storage reduction catalyst containing the synthesized support had a larger NO_x storage capacity than the catalyst containing the physically mixed oxide.

1. Introduction

In an effort to protect the environment, and minimize the effects of greenhouse gases, a reduction in the emission of carbon dioxide (CO_2) from automobiles is necessary. The lean-burn engine system is one of the most effective methods to improve the fuel efficiency of vehicles. However, one major drawback of this system is that conventional three-way catalysts cannot reduce nitrogen oxides (NO_x) into nitrogen (N_2) due to the existence of excessive oxygen in the exhaust gases. A number of catalyst systems have been explored to reduce NO_x in lean systems [1-3].

The NO_x storage reduction catalyst (NSR catalyst) is one of the most attractive methods to purify exhaust gases from the lean-burn engine [4, 5]. The mechanism of the NO_x storage and reduction reactions on the NSR catalysts is as follows [6]. First, during the lean condition, excess NO_x is oxidized to NO_2 on the precious metals and stored in the form of nitrate in storage materials. Second, when the engine is switched to operate on a rich air-fuel ratio, nitrate stored in the storage material is reduced to N_2 by hydrogen (H_2), carbon monoxide (CO), and hydrocarbons (HC).

The NSR catalyst has two main technical problems: sulfur poisoning and thermal deterioration. Sulfur dioxide (SO_2) contained in gas exhaust reacts with the storage materials and forms sulfate. However, recent studies on sulfur durability have reported that TiO_2 in supports has been found to be provide a high tolerance against sulfur poisoning due to its high acidity [7].

Thermal deterioration of the catalyst occurs due to both solid-phase reaction of NO_x storage materials with TiO_2 and aggregation of the support particles. In an effort to avoid solid-phase reaction, ZrO_2 is typically added as ZrO_2-TiO_2 solid solution [6, 8]. On the other hand, Al_2O_3, which has excellent thermal stability, is added to the support.

Typically, Al_2O_3 is physically mixed with other support materials, and does not contribute to the thermal stability of other support components. Nanocomposites of Al_2O_3 and CeO_2-ZrO_2 solid solution have been used as a support for three-way catalysts, and have been shown to inhibit the thermal aggregation of CeO_2-ZrO_2 [8], because Al_2O_3 acts as the diffusion barrier for CeO_2-ZrO_2 particles in the secondary particles. As a result, particle growth of not only CeO_2-ZrO_2, but also precious metals on the supports is prevented. This concept of the nanocomposite can be applied to ZrO_2-TiO_2, that is, the thermal aggregation of ZrO_2-TiO_2 particles may be inhibited in the presence of Al_2O_3 particles (Fig. 1).

The purpose of this investigation is to improve the thermal stability of a support for NSR catalysts. In this work, the effects of the novel support on the thermal stability in both powder and catalyst are examined.

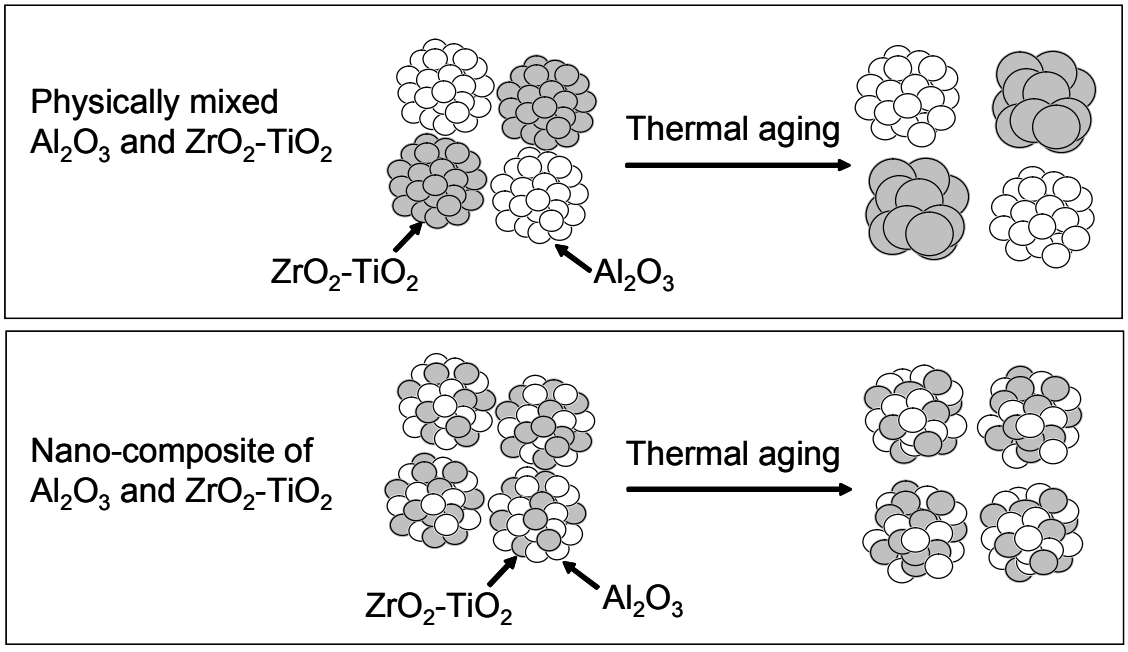

Fig. 1. Concept chart of AZT.

2. Experimental

2.1. Preparation of supports

The nanocomposite oxide containing Al_2O_3, ZrO_2, and TiO_2 (AZT) was prepared by conventional coprecipitation. $Al(NO_3)_3 \cdot 9H_2O$, $ZrO(NO_3)_2 \cdot 2H_2O$, and $TiCl_4$ (Wako Pure Chemical Industries) were dissolved in ion-exchanged water, and then an ammonia solution was added for coprecipitation. The obtained product was dried at 673 K for 5 h and calcined at 1073 K for 5 h in air. The weight ratio of Al_2O_3 to ZrO_2-TiO_2 was 50:50. The mole ratio of ZrO_2 to TiO_2 was 60:40, which showed maximal durability against heat [6].

Pure γ-Al_2O_3 was prepared by the same method. Pure ZrO_2-TiO_2 was prepared by the same method, as reported in literature [6]. Reference support was obtained by physically mixing pure γ-Al_2O_3 and ZrO_2-TiO_2. The composition of the physically mixed oxide was the same as that of AZT.

2.2. Characterization of supports

The crystal structure was characterized by powder X-ray diffraction (XRD). XRD patterns were recorded using a Rigaku RINT-2100 (CuKα radiation (λ=1.5418 Å), 40 kV, 30 mA). To analyze the distribution of Al_2O_3 and ZrO_2-TiO_2, field-emission transmission electron microscopy (FE-TEM) was performed on a Hitachi HF-2000.

The BET surface area was measured by N_2 adsorption at 77 K using Micro Data MICRO SORP 4232II.

The pore size distribution was calculated from the intrusion curve obtained with a mercury porosimetry using Quantachrome Pore Master GT60-1.

The surface acid-base properties of the supports were measured by NH_3- and

CO_2-temperature programmed desorption (TPD). Samples were formed into 0.3-0.7 mm diameter pellets. In NH_3-TPD, after pretreatment at 773 K under a N_2 atmosphere, NH_3 was added in the stream of N_2 at 373 K, and then samples were heated to 773 K at a rate of 20 K/min. NH_3 desorbed from samples under the N_2 atmosphere were observed using a non-dispersive infrared (NDIR) type analyzer, Best Sokki CATA5000. CO_2-TPD was measured in the same method with NH_3-TPD. Helium (He) was used as balance gas instead of N_2, and desorbed CO_2 was observed using a NDIR type analyzer, Horiba MEXA-7100.

2.3. Analysis of supports after thermal treatment

Samples used were heated at 1073 K, 1173 K and 1273 K for 5 hours in air containing 3 % water. The crystal structure after thermal treatment was analyzed by XRD and the particle size of ZrO_2-TiO_2 was calculated using Scherrer's formula [9]. The samples calcined at 1173 K were analyzed by FE-TEM in order to investigate the state of ZrO_2-TiO_2.

2.4. Catalytic application

Catalysts were prepared by impregnating $Pt(NH_3)_2(NO_2)_2$ and $Rh(NO_3)_3$ (Tanaka Precious Metals), then dried at 383 K for 12 h and finally calcined at 523 K for 3 h in air. The loading amounts of platinum and rhodium were 1.23 and 0.06 wt%. The powder obtained was then added to an aqueous solution containing $(CH_3COO)_2Ba$ and CH_3COOK (Wako Pure Chemical Industries) as precursors to the storage materials. The loading amounts of barium as BaO and potassium as K_2O were 18.8 and 5.8 wt%. After the catalysts were dried at 383 K for 12 h, they were calcined at 773 K for 3 h in air. The powder obtained was formed into 0.3-0.7 mm diameter pellets.

In thermal aging tests, the catalyst was exposed to a feedstream as shown in Table 1, which simulated the actual engine exhaust gas, and heated at 1073 K for 5 hours. The lean and rich atmospheres were switched every 2 minutes. The gas flow rate was 1000 cm^3/minute and the gas hourly space velocity was 30 000 h^{-1}.

The amount of NO_x stored was measured using a conventional fixed-bed flow reactor system at atmospheric pressure. Table 1 shows the composition of the feedstreams simulating the actual engine exhaust gas for this measurement. Overview of the measurement is shown in Fig. 2. After the catalyst was heated at 573 K under a rich atmosphere, the gas was switched to the lean atmosphere until the outlet NO_x concentration reached a constant value. Then a 3s-rich spike was introduced to the catalyst. Subsequently, the gas was switched to the lean atmosphere until the outlet NO_x concentration reached a constant value. The amount of NO_x stored was calculated as the difference in the NO_x amount between the inlet and the outlet gases after the rich spike (shaded area in Fig. 2). Measurement of the amount of NO_x stored at 673 K and 773 K was similar to that at 573 K. The gas flow rate was 3000 cm^3/minutes and the gas hourly space velocity was 180 000 h^{-1}. The NO_x concentration was measured using a chemiluminescent NO_x meter attached to a Horiba MEXA-7100.

The noble metal dispersion was obtained from CO pulse chemisorption at 323K with Ohkura Riken R6015-S. The pulse gas was 100 vol% CO for fresh catalysts or 2 vol% CO in He for aged catalysts. The metal dispersion was calculated by assuming a CO to surface metal atom ratio was 1:1 for convenience [10].

Table 1. Gas composition for thermal aging test and NOx storage measurement

Atmosphere	C_3H_6 (%C)	CO (%)	H_2 (%)	NO (ppm)	CO_2 (%)	O_2 (%)	H_2O (%)
Thermal aging test [a]							
Lean	0.065	0	0	800	11	6.6	3
Rich	0.34	5.6	1.9	50	11	0	3
NOx storage measurement [b]							
Lean	0.02	0	0	800	11	6.6	3
Rich	0.11	5.6	1.9	0	11	0.3	3
Rich Spike	0.11	5.6	1.9	50	11	0	3

[a] N_2 balance.

[b] He balance.

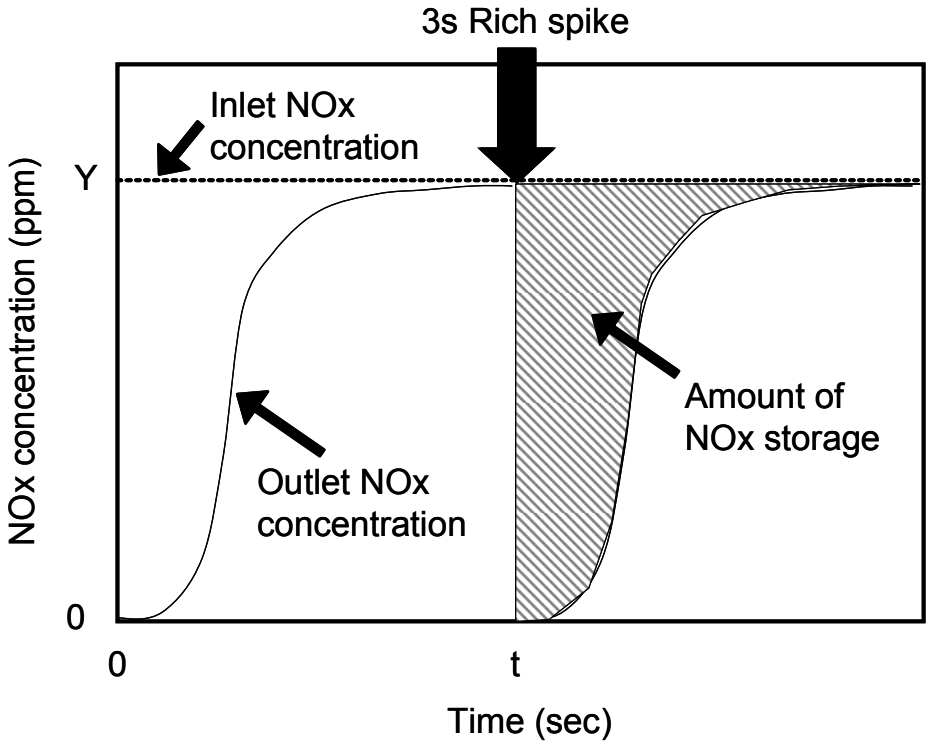

Fig. 2. Measurement of the amount of NOx storage. Inlet NOx concentration Y: 800 ppm for pelletized catalysts, 400 ppm for monolith catalysts; inlet NOx concentration (▪▪▪▪▪); outlet NOx concentration (——).

3. Results and discussion

3.1. Analysis of the structure of AZT

The XRD pattern of the sample is shown in Fig. 3. AZT consists of an amorphous γ-Al_2O_3 phase and a crystalline tetragonal ZrO_2 phase after calcination at 1073 K. The peak assigned to tetragonal ZrO_2 (101) phase shifted from $2\theta = 30.22^o$ to 30.42^o. Therefore, this peak shift suggests that TiO_2 has been solved in the ZrO_2 phase and ZrO_2-TiO_2 solid solution has formed in the synthesis step.

The TEM image of AZT is shown in Fig. 4. Al_2O_3 primary particle (pale gray particle) and ZrO_2-TiO_2 primary particle (dark gray and clear-shape particle) coexisted in the same secondary particles. Each of the primary particles was less than 20 nm. This structure is attributed to the condition under which precipitation of Al_2O_3 and ZrO_2-TiO_2 begins to develop at the same time. In brief, this novel synthesized support consists of a nanocomposite of amorphous γ-Al_2O_3 and ZrO_2-TiO_2 solid solution

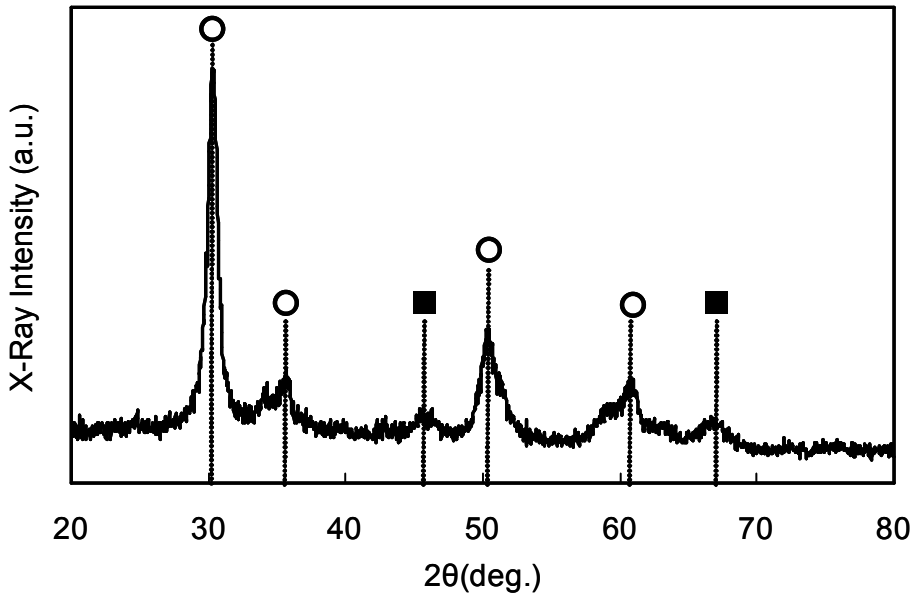

Fig. 3. XRD spectra of AZT calcined at 1073 K. ○: tetragonal ZrO_2, ■: γ-Al_2O_3

.

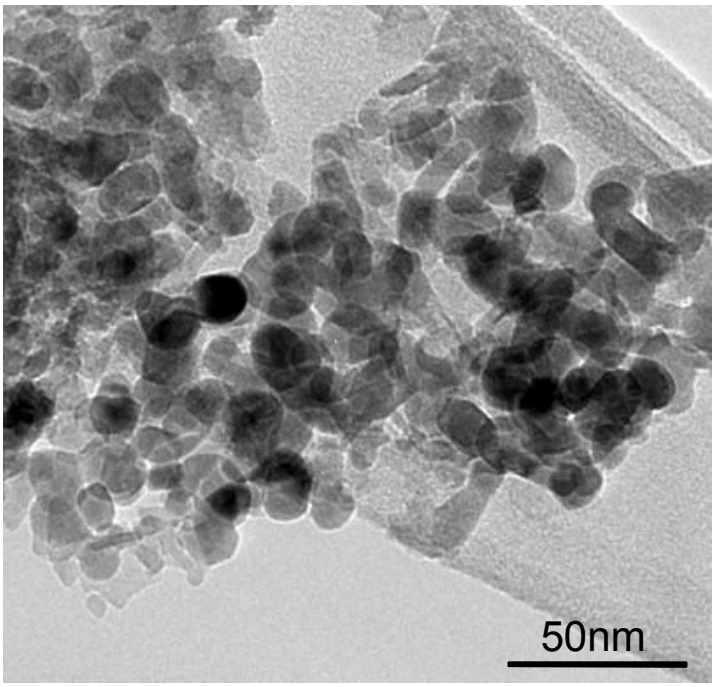

Fig. 4. FE-TEM micrograph of AZT calcined at 1073 K.

3.2. Characterization of AZT

3.2.1. Surface area

Figure 5 shows the BET surface area at each calcination temperature. Even at 1073 K, AZT had a large surface area, approximately 130 m^2/g. Compared with the change of the BET surface area in pure ZrO_2-TiO_2, the surface area of AZT decreased linearly as the calcination temperature increased, and did not show a sharp drop between 873 and 973 K. This sharp drop in pure ZrO_2-TiO_2 results from the rapid crystallization and sintering of ZrO_2-TiO_2. The Al_2O_3 particle acts as the diffusion barrier of the ZrO_2-TiO_2 particle in AZT, which prevents rapid sintering of the ZrO_2-TiO_2 particle. Therefore, such a sharp drop of the surface area is prevented and a large surface area in AZT is maintained.

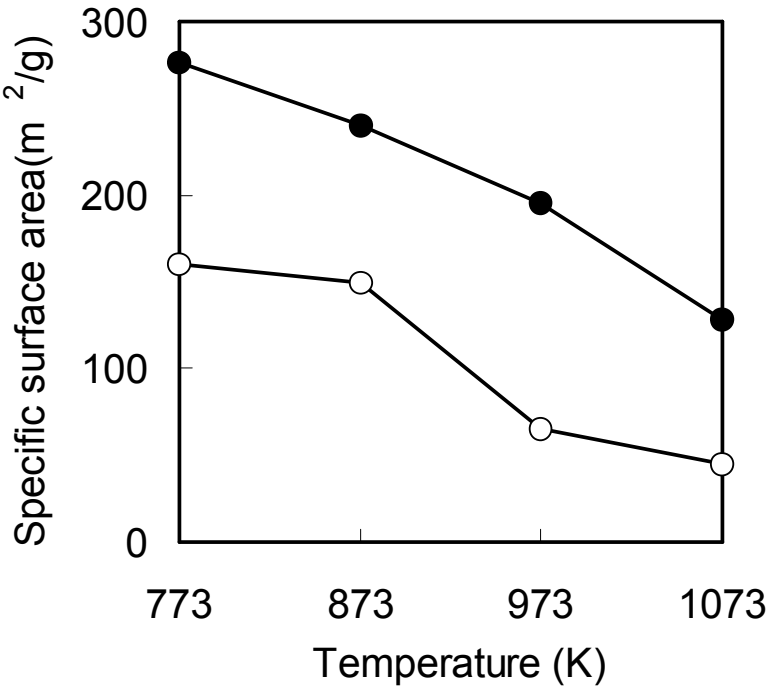

Fig. 5. BET-specific surface area of samples versus calcination temperature.●: AZT, ○: Pure ZrO_2-TiO_2

3.2.2. Pore diameter distribution

Figure 6 shows the pore diameter distribution of each sample. AZT had a single sharp meso-pore around 15 nm (Fig. 6(a), black line). In AZT, Al_2O_3 and ZrO_2-TiO_2 exist in the same secondary particle and there is only one kind of pore in the secondary particle. This pore diameter distribution is in good agreement with that of the structure.

On the other hand, the mixture of Al_2O_3 and ZrO_2-TiO_2 (physically mixed oxide) had a broad pore distribution from 9 nm to 40 nm (Fig. 6(b), gray line). This broad distribution is brought about by the mixture of the two different kinds of pores derived from the Al_2O_3 secondary particle and ZrO_2-TiO_2 secondary particle. After calcination of

the physically mixed oxide at 1073 K, two characteristic peaks were clearly observed (Fig. 6(c), black broken line). As the ZrO_2-TiO_2 particle is easily sintered with the increase in calcination temperature, the larger diameter peak is derived from the ZrO_2-TiO_2 secondary particle and the smaller one is derived from Al_2O_3 secondary particle.

The meso-pore volume after calcination at 1073 K is shown in Table 2. AZT had a larger meso-pore volume than the physically mixed oxide, because ZrO_2-TiO_2 particles in AZT has been inhibited from aggregating and held the large spacing among the primary particles.

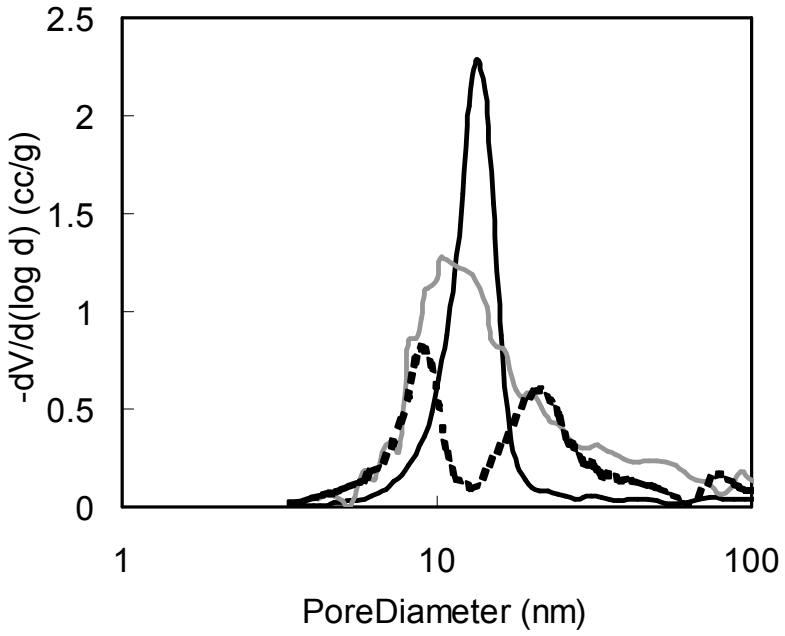

Fig. 6. Pore distribution of samples: (a) AZT calcined at 1073K (——), (b) Physically mixed Al_2O_3 calcined at 1073 K and ZrO_2-TiO_2 calcined at 773K (——), (c) Physically mixed Al_2O_3 and ZrO_2-TiO_2 calcined at 1073 K (– –).

Table 2. Meso-pore volume and acid-base amount of samples

	Meso-pore volume (cc/g)	Acid amount (μmol/g)	Base amount (μmol/g)
Nano-composite oxide	0.415	96.7	2.7
Physically mixed oxide	0.318	105.4	12.1

3.2.3. Acid-base property

It has been reported that TiO_2 in supports has high tolerance against sulfur poisoning, because TiO_2 is one of the acidic oxides [7]. Therefore, in this system, TiO_2 is involved as a ZrO_2-TiO_2 solid solution. In an effort to observe the effect of the structure of AZT on the acid-base properties, the surface acidity and basicity were measured by a NH_3- and CO_2-TPD experiment, respectively.

Table 2 shows the amount of acid in each sample. The amount of acid in AZT was almost the same as those composed of the physically mixed oxide and both NH_3-TPD spectra had a peak around 450 K, indicating that the conformation of the Al_2O_3 particle and ZrO_2-TiO_2 particles had no effect on the acidity of the material.

In the CO_2-TPD spectra, the maximum CO_2 concentration of AZT was quite smaller than that of the physically mixed oxide. Table 2 shows the amount of base determined by the CO_2 desorption from the samples. The amount of base in AZT was 1/5 times as large as that in the physically mixed oxide. This result suggests the possibility of inhibition of adsorption of SO_x on the surface in NSR catalysts using AZT as a support.

The CO_2 adsorbed onto ZrO_2-TiO_2 is nearly negligible [6]. Therefore, the difference in the basicity between AZT and the physically mixed oxide is derived from the Al_2O_3 state. In the physically mixed oxide, CO_2 is easily adsorbed to the basic surface of the Al_2O_3 particle due to the pure Al_2O_3 secondary particle. On the other hand, in AZT, it can be inferred that the basicity of Al_2O_3 was decreased due to the existence of trace amounts of impurity such as TiO_2 and/or ZrO_2. The method of synthesizing AZT is coprecipitation, therefore, it is possible that a trace amount of Ti and/or Zr exist on the surface of the Al_2O_3 particle. However, the acidity of ZrO_2 is significantly lower than TiO_2, and ZrO_2 is highly basic [6]. On the other hand, TiO_2 has a high acidity and negligible basicity. Thus, the basicity of Al_2O_3 is canceled by the acidity of TiO_2 to some

degree. To clarify this point, further experiments must be performed.

3.2.4. ZrO_2-TiO_2 particle after thermal treatment

Figure 7 shows the average particle size for ZrO_2-TiO_2 determined by XRD after thermal treatment. At temperatures less than 1073 K, the particle size of AZT could not be determined with XRD because the ZrO_2-TiO_2 phase was amorphous. Therefore, the average particle size of ZrO_2-TiO_2 was examined at temperatures greater than 1073 K.

The particle size of ZrO_2-TiO_2 in AZT was smaller than that in the physically mixed oxide at each temperature measured. The difference in ZrO_2-TiO_2 particle size between AZT and the physically mixed oxide increased with the increase in temperature in the thermal treatment. At 1273 K, the ZrO_2-TiO_2 particle size in AZT oxide was about half the size of that in the physically mixed oxide.

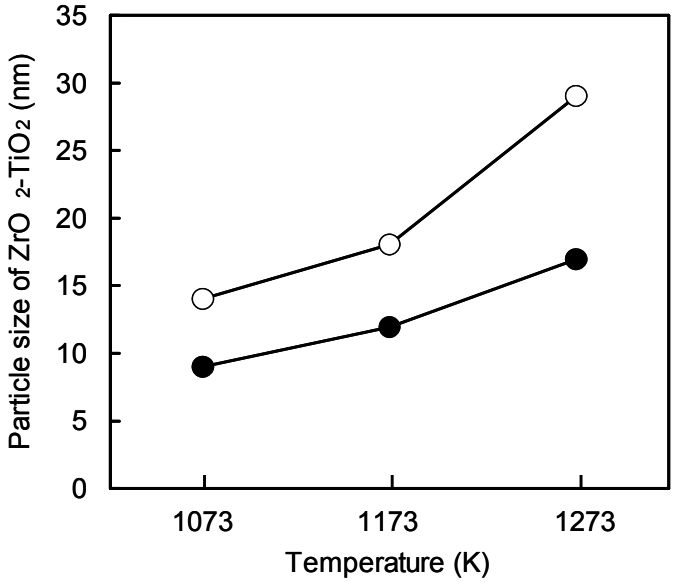

Fig. 7. Average particle size of ZrO_2-TiO_2 determined by XRD data versus thermal treatment temperature. ●: AZT, ○: Physically mixed Al_2O_3 and ZrO_2-TiO_2

Figure 8 shows the TEM image after thermal treatment at 1173 K. In AZT (Fig. 8(a)), the particle size of the primary ZrO_2-TiO_2 particles was less than 30 nm on average. On the other hand, the aggregation of the ZrO_2-TiO_2 particles in the physically mixed oxide was observed compared with that in AZT (Fig. 8(b)).

ZrO_2-TiO_2 primary particles in AZT are surrounded by Al_2O_3 primary particles, which serve as the diffusion barrier for ZrO_2-TiO_2. Therefore, the aggregation of ZrO_2-TiO_2 primary particles by heat is inhibited in AZT in accordance with the concept showed in Fig. 1.

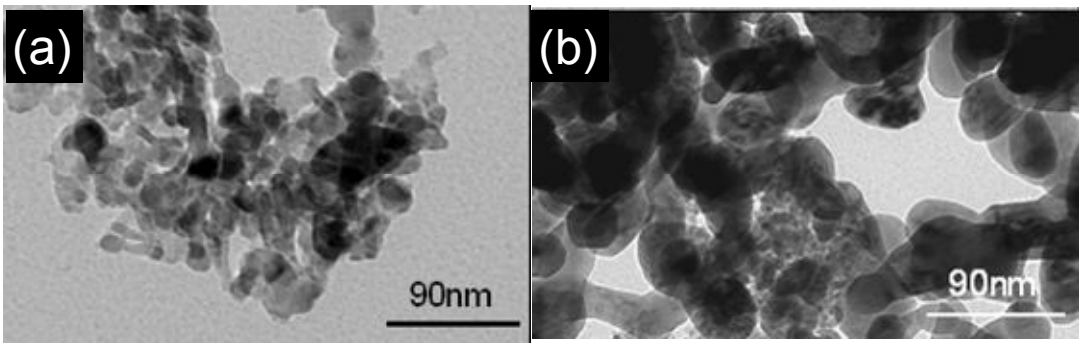

Fig. 8. FE-TEM micrographs of samples after thermal treatment at 1173 K. (a) AZT, (b) Physically mixed Al_2O_3 and ZrO_2-TiO_2.

3.3. Catalytic application

To confirm the effect of thermal resistance of AZT as a support for a NO_x storage reduction catalyst, the NO_x storage amount of catalysts thermally aged was measured. The NO_x storage amount at each temperature is shown in Fig. 9(a) and the NOx concentration profile in the outlet gas at 673K is depicted in Fig. 9(b). The catalyst containing AZT (AZT catalyst) had larger amount of NO_x storage than that containing the physically mixed oxide (Physically mixed catalyst). At 673 K, the NO_x storage of AZT

catalyst was twice as large as that of physically mixed catalyst. The Ba and K species under lean condition are assumed to be nitrate species such as $Ba(NO_3)_2$ and KNO_3, as reported in literatures [5, 11, 12].

The particle size of ZrO_2-TiO_2 in catalysts was analyzed by XRD after a thermal aging test. Compared with the result at 1073 K in Fig. 7, the ZrO_2-TiO_2 particle size in AZT was almost the same, even in the catalyst that underwent the thermal aging test. On the other hand, in the physically mixed oxide, the particle size of ZrO_2-TiO_2 became twice the size of the powder after the thermal aging test.

The aggregation and deterioration of precious metal on AZT are expected to be inhibited relative to those in physically mixed oxides. To confirm this point, the noble metal dispersion of catalysts was measured by CO pulse chemisorption. In fresh catalyst, the noble metal dispersion of AZT catalyst was 6.8% and that of physically mixed catalyst was 10.3%. But after thermal aging test, the dispersion of AZT catalyst was 2.5% and that of physically mixed catalyst was 1.3%. Therefore, AZT catalyst has a higher density of catalytically active sites after thermal aging test relative to physically mixed catalyst.

For practical purposes, a NO_x storage reduction catalyst is mainly exposed to temperatures such as 673 K [11], that is, AZT is a promising material for high performance in real exhausted gases from lean-burn engines.

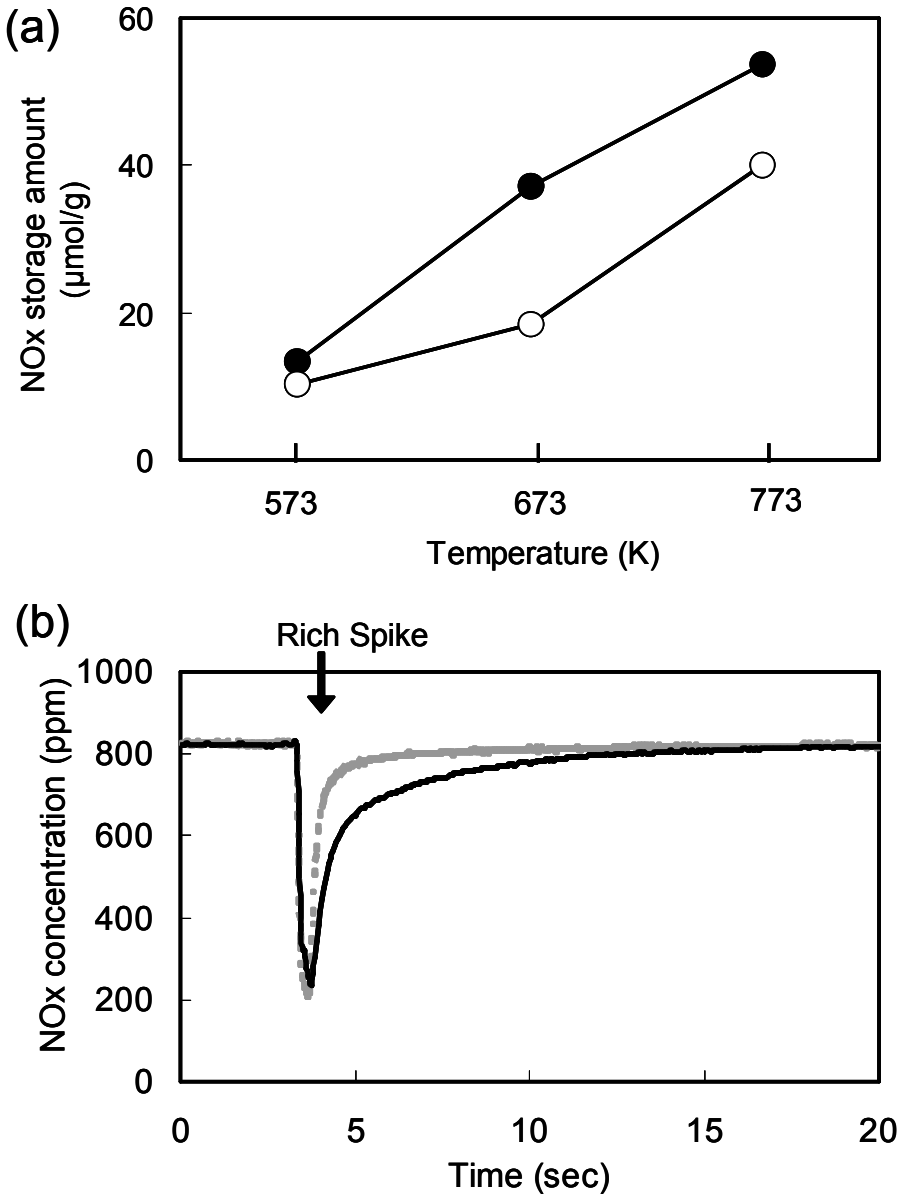

Fig. 9. (a) NO_x storage performance versus reaction temperature after thermal aging test. ●: AZT catalyst; Catalyst using AZT as a support, ○: physically mixed catalyst; Catalyst using physically mixed Al_2O_3 and ZrO_2-TiO_2 as support. (b) NO_x concentration profile in the outlet gas at 673K under lean-rich cycle after thermal aging test: AZT catalyst (━━━), physically mixed catalyst (▬ ▬).

4. Conclusion

A nanocomposite of γ-Al_2O_3 and ZrO_2-TiO_2 solid solution was synthesized. After thermal treatment, the aggregation of ZrO_2-TiO_2 particles in AZT was inhibited relative to that in the physically mixed Al_2O_3 and ZrO_2-TiO_2. This was thought to be because Al_2O_3 particles act as a diffusion barrier to ZrO_2-TiO_2 particles in AZT.

After a thermal aging test using simulated model exhausted gas from lean-burn engines, the catalyst containing AZT as a support for NO_x storage reduction catalysts had a larger amount of NO_x storage than that containing the physically mixed oxide. This result suggests that using the nanocomposite of Al_2O_3 and ZrO_2-TiO_2 as a support is a better method for a NO_x storage reduction catalyst.

References

[1] S. Sato, Y. Yu-u, H. Yahiro, N. Mizuno, M. Iwamoto, *Appl. Catal.* 70 (1991) L1.

[2] Y. Kintaichi, H. Hamada, M. Tabata, M. Sasaki, T. Ito, *Catal. Lett.* 6 (1990) 239.

[3] R. Burch, P. J. Millington, *Catal. Today* 26 (1995) 185.

[4] W. Bögner, M. Krämer, B. Krutzsch, S. Pischinger, D. Voigtländer, G. Wenninger, F. Wirbeleit, M. S. Brogan, R. J. Brisley, D.E. Webster, *Appl. Catal. B: Environ.* 7 (1995) 153.

[5] N. Takahashi, H. Shinjoh, T. Iijima, T. Suzuki, K. Yamazaki, K. Yokota, H. Suzuki, N. Miyoshi, S. Matsumoto, T. Tanizawa, T. Tanaka, S. Tateishi, K. Kasahara, *Catal. Today* 27 (1996) 63.

[6] N. Takahashi, A. Suda, I. Hachisuka, M. Sugiura, H. Sobukawa, H. Shinjoh, *Appl. Catal. B: Environ*. 72 (2006) 187.

[7] S. Matsumoto, Y. Ikeda, H. Suzuki, M. Ogai, N. Miyoshi, *Appl. Catal. B: Environ*. 25 (2000) 115.

[8] T. Kanazawa, *Catal. Today* 96 (2004) 171.

[9] Y. Xie, C. Yuan, *Appl. Catal. B: Environ.* 46 (2003) 251.

[10] J. A. Anderson, R. A. Daley, S. Y. Christou, A. M. Efstathiou, *Appl. Catal. B: Environ.* 64 (2006) 189.

[11] M. Takeuchi, S. Matsumoto, *Top. Catal.* 28 (2004) 151.

[12] N. Takahashi, K. Yamazaki, H. Sobukawa, H. Shinjoh, *J. Chem. Eng. Jpn.* 39 (2006) 437.

Chapter 3

Analysis of NO_x storage materials on AZT for thermal stability and sulfur durability

Abstract

A nanocomposite of Al_2O_3 and ZrO_2-TiO_2 solid solution (AZT) was synthesized for NO_x storage-reduction (NSR) catalysts Pt/Rh/Ba/K/AZT, and the effect of calcination temperature on thermal stability was investigated. The catalyst containing AZT calcined at 1073 K (AZT catalyst) had a high NO_x storage capacity after thermal aging. This enhanced storage capacity was attributed to the fact that ZrO_2-TiO_2 solid solution (ZT) was crystallized and stabilized. The solid-state reaction of potassium, which was added as a NOx storage material, was inhibited in the AZT catalyst, relative to those containing AZT calcined at a low temperature. The AZT catalyst also showed excellent NO_x storage performance after sulfur aging at 973 K or higher, compared with the catalyst containing physically mixed Al_2O_3 and ZT (physically mixed catalyst). Furthermore, AZT catalysts inhibited the solid phase reaction of potassium with support materials and kept a high ratio of active potassium, which can store NO_x. Further, because the barium in the AZT catalyst prevented sulfur poisoning, the ratio of active barium in the AZT catalyst was also larger than that in the physically mixed catalyst, probably because of the low basicity and high Pt dispersion of AZT.

1. Introduction

The lean-burn engine is a promising means for reducing carbon dioxide (CO_2) emissions from automobiles. However, since lean-burn combustion produces excess oxygen in the process of combustion, conventional three-way catalysts cannot completely reduce nitrogen oxides (NO_x) to nitrogen (N_2) under lean conditions. To overcome this problem, a variety of catalysts for reducing NO_x in lean systems have been investigated [1-4].

The NO_x storage-reduction catalyst (NSR catalyst) is one of the most attractive methods for reducing NO_x emissions from lean-burn engines [5,6]. The NSR catalyst operates as shown in the introduction part in Chapter 2, according to the following reaction mechanism [7]: First, excess NO_x is oxidized to NO_2 on precious metal catalysts and stored in the form of nitrate in the storage materials. When the engine operation is switched to a rich air-fuel ratio, the nitrates stored in the storage material are reduced to N_2 by hydrogen (H_2), carbon monoxide (CO), and hydrocarbons (HCs).

The NSR catalyst has two technical disadvantages: sulfur poisoning and thermal deterioration. Sulfur poisoning is caused by sulfur dioxide (SO_2) in the exhaust gas. SO_2 adsorbs onto the catalysts and reacts with the storage materials, forming sulfate salts, and the NO_x storage materials can no longer store NO_x. Consequently, the effect of sulfur on storage materials has been extensively investigated [8-14]. Recent studies on sulfur durability in catalysts have reported that TiO_2 in support materials provides high tolerance against sulfur poisoning due to the high acidity/low basicity of TiO_2 [8,15-17]. Furthermore, TiO_2 is used in the fabrication of ZrO_2-TiO_2 solid solution (ZT) to prevent the solid-phase reaction of the NO_x storage materials with TiO_2 upon heating [7,16]. ZT has also been shown to have low basicity for sulfur durability without losing TiO_2

properties [7,17]. Al_2O_3 is indispensable in automobile catalysts because of its excellent thermal stability; however, since it tends to adsorb SO_2 due to its high basicity, the addition of TiO_2 to Al_2O_3 has been investigated in order to prevent SO_2 from adsorbing on the catalyst surface [18]. TiO_2 doped Al_2O_3 with sulfur resistance is thus an important consideration affecting the sulfur durability of the NSR catalyst.

Thermal deterioration of the catalyst is not only caused by the aggregation of support materials and precious metals [19], but also by the solid-phase reaction of the NO_x storage materials [20,21]. In Chapter 2, the author developed a novel nanocomposite of Al_2O_3 and ZT (AZT) as a support material [22]. In this nanocomposite, primary Al_2O_3 and ZT particles coexist within the same secondary particle. AZT has been found to inhibit the thermal aggregation of ZT, because Al_2O_3 acts as a diffusion barrier to ZT particles in secondary particles. Therefore, the particle growth of ZT as well as the sintering of precious metals on the supports can be prevented. In addition, since AZT has been shown to have low basicity due to the presence of a small amount of TiO_2 in Al_2O_3 [18], the NSR catalyst containing AZT as a support material exhibits both higher sulfur durability and excellent thermal stability.

However, in order to further improve the NSR catalyst, it is necessary to confirm the mechanism of the superior NSR performance using AZT with an ideal structure. Although basic characterization of AZT as a support has been already carried out in the previous chapter, detailed characterization of AZT catalyst for NSR reaction has not yet been conducted. Investigation of the relationship between supports and NOx storage materials after aging tests will lead to new findings not only for thermal stability, but also for sulfur durability.

The purpose of this investigation is to analyze and improve the thermal stability and sulfur durability of the NSR catalyst using AZT through the analysis of storage

materials. This chapter consists of two topics. In the first section, the effect of the calcination temperature of AZT on thermal stability was investigated. In the second section, a monolithic catalyst containing AZT after sulfur aging at high temperature was analyzed. The evaluation of catalysts using a monolithic substrate is a useful method for determining the practicability of a real NSR catalyst. These findings are of particular interest for determining the state of NO_x storage materials.

2. Experimental

2.1. Preparation of supports

AZT was prepared using a conventional co-precipitation method [22], with the mole ratio for Al_2O_3:ZrO_2:TiO_2 being 50:30:20 (mol%). The obtained powder was calcined at 773, 873, 973, 1073, and 1173 K for 5 h, and is referred to herein as AZTn (n=773, 873, 973, 1073, and 1173).

Pure γ-Al_2O_3 was prepared using the same method described for AZT [22], and pure ZT was prepared as described in the literature [7]. A reference support was obtained by physically mixing pure γ-Al_2O_3 and ZT (physically mixed oxide). The composition of the physically mixed oxide was the same as that of AZT.

The Brunauer-Emmett-Teller (BET) surface area of AZTn was measured by N_2 adsorption at 77 K using an automatic surface area analyzer (Micro Data, Micro Sorp 4232II). The crystal structures of AZTn and pure ZT were characterized by powder X-ray diffraction (XRD). XRD patterns were recorded using an X-ray diffractometer (Cu Kα radiation λ= 1.5418 Å, 40 kV, 30 mA) (Rigaku, RINT-2100). The particle size of ZrO_2-TiO_2 was calculated using Scherrer's formula [23]. The peak at 2θ = 30.4°, assigned to the tetragonal ZrO_2 (101) phase, was used to calculate the particle size of ZT.

The base surface properties of the supports were measured using CO_2-temperature programmed desorption (CO_2-TPD). Samples were formed into 0.3-0.7 mm diameter pellets. The CO_2-TPD samples were pretreated at 773 K in a helium (He) atmosphere. After the samples had been exposed to CO_2 under a stream of He at 373 K, they were heated to 773 K at a rate of 20 K/min. CO_2 desorbed from samples in a He atmosphere was observed using a non-dispersive infrared (NDIR) analyzer attached to an exhaust gas analyzer (Horiba, MEXA-7100).

2.2. Effect of AZT calcination temperature on thermal stability

Pellet catalysts were prepared by impregnating $Pt(NH_3)_2(NO_2)_2$ and $Rh(NO_3)_3$ (Tanaka Precious Metals) with the AZT prepared in section 2.1, drying at 383 K for 12 h, and finally calcining at 523 K for 3 h in air. The Pt and Rh loadings were 1.23 and 0.06 wt%, respectively. The powder obtained was then added to an aqueous solution containing $(CH_3COO)_2Ba$ and CH_3COOK (Wako Pure Chemical Industries) as precursors to the storage materials. The loading amounts of barium as BaO and potassium as K_2O were 18.8 and 5.8 wt%, respectively. After the catalysts were dried at 383 K for 12 h, they were calcined at 773 K for 3 h in air. The powder obtained was formed into 0.3-0.7 mm diameter pellets, resulting in the catalyst using AZTn being referred to as the pelletized AZTn catalyst (P-AZTnCat).

For thermal aging, the fresh pelletized catalysts were exposed to a feed-stream, as shown in Table 1. The stream simulated actual engine exhaust gas, and was heated at 1073 K for 5 h. The lean and rich atmospheres were cycled at 2 min intervals using a flow rate of 1000 cm^3/min and a gas hourly space velocity (GHSV) of 30 000 h^{-1}.

The sulfur-aging tests for the fresh pelletized catalysts were carried out at 873 K in a sulfur-containing atmosphere for the two gas compositions shown in Table 1.

Table 1. Gas composition for thermal and sulfur aging test, and NOx storage measurement for pelletized catalysts.

Atmosphere	C_3H_6 (%C)	CO (%)	H_2 (%)	NO (ppm)	CO_2 (%)	SO_2 (ppm)	O_2 (%)	H_2O (%)
Thermal aging test [a]								
Lean	0.065	0	0	800	11	0	6.6	3
Rich	0.34	5.6	1.9	50	11	0	0	3
Sulfur aging test [a]								
Lean	0.15	1.43	0.47	800	9.6	480	7.7	3
Rich	0.16	4.5	1.5	50	10	500	0	3
NO_x storage measurement [b]								
Lean	0.02	0	0	800	11	0	6.6	3
Rich	0.11	5.6	1.9	0	11	0	0.3	3
Rich Spike	0.11	5.6	1.9	50	11	0	0	3

[a] N_2 balance.

[b] He balance.

The lean and rich atmospheres were alternated every 30 s, and a gas flow rate of 4000 cm^3/min and a GHSV of 240 000 h^{-1} were used. The mole ratio of SO_2 to storage materials was S/(Ba+0.5K) = 1.5.

The amount of NO_x stored in the aged pelletized catalysts was measured using a conventional fixed-bed flow reactor system at atmospheric pressure. Table 1 shows the composition of the feed-streams used to simulate actual engine exhaust gases for this measurement [22]. After 0.5 g of the pelletized catalyst was heated to 573 K under the rich atmosphere condition, the gas was switched to the lean atmosphere condition until the outlet NO_x concentration became constant, and then the catalyst was exposed to a 3 s rich spike. During rich spike injection, NOx storage sites are regenerated, and the gas was

subsequently switched to the lean atmosphere until the outlet NO_x concentration became constant. The amount of NO_x stored was calculated as the difference in NO_x between the inlet and the outlet gases after introduction of the rich spike. The molar amount of total reducing agents during a 3 s rich spike is more than that of all NOx storage sites, given NOx storage materials form $Ba(NO_3)_2$ and KNO_3.

The amounts of NO_x stored at 673 and 773 K were measured in the same manner as for 573 K, and these measurements were carried out sequentially after the experiment at 573 K. The gas flow rate was 3000 cm^3/min and the GHSV was 180 000 h^{-1}. The NO_x concentration was measured using a chemiluminescence NO_x meter attached to a gas exhaust analyzer (Horiba, MEXA-7100).

The state of potassium in the pelletized catalysts was analyzed using an inductively coupled plasma emission (ICP) spectrometer (Rigaku, CIROS 120EOP) as described elsewhere in the literature [7].

2.3. Analysis of the AZT catalyst for sulfur durability

A 7 g quantity of support powder was wash-coated on a hexagonal cell cordierite monolithic substrate (62 cells/cm^2) with a diameter of 30 mm and a length of 50 mm. AZT1073 was selected as a support, and a physically mixed oxide was used as a reference support. Catalysts were prepared by impregnating $Pt(NH_3)_2(NO_2)_2$ and $Rh(NO_3)_3$, drying at 383 K for 12 h, and finally calcining at 573 K for 3 h in air. The amounts of Pt and Rh were 0.8 and 0.2 wt%, respectively. The coated substrates were then added to an aqueous solution containing $(CH_3COO)_2Ba$ and CH_3COOK as precursors of the storage materials. The loading amounts of barium as BaO and potassium as K_2O were 12.8 and 2.9 wt%, respectively. Once catalysts had been dried at 383 K for 12 h, they were calcined at 573 K

for 3 h in air. The catalyst using AZT1073 as a support is referred to as the monolithic AZT catalyst, and that using the physically mixed oxide is referred to as the physically mixed catalyst in section 3.2.

Sulfur aging of the monolithic catalysts at high temperature was carried out at 973, 1023, and 1073 K for 5 h under a sulfur-containing atmosphere (Table 2). The 110 s lean and the 10 s rich atmospheres were then cycled alternately for the duration of the aging test. The gas flow rate was 10 000 cm^3/min and the GHSV was 17 140 h^{-1}.

As described in section 2.2, the amount of NO_x stored on the aged monolithic catalysts was measured in the same manner as that at 673 K, under the gas composition shown in Table 2. The gas flow rate was 30 000 cm^3/min and the GHSV was 51 500 h^{-1}. The gas composition and gas flow rate in this measurement is slightly modified based on that for pelletized catalysts shown in the section 2.2 in order to reflect more practical condition suited for monolithic catalysts [21,24]. The NO_x concentration was measured using a chemiluminescence NO_x meter attached to a gas exhaust analyzer (Best Sokki, CATA-5000).

Table 2. Gas composition for sulfur aging test, and NOx storage measurement for monolithic catalysts.

Atmosphere	C_3H_6 (%C)	CO (%)	H_2 (%)	NO (ppm)	CO_2 (%)	SO_2 (ppm)	O_2 (%)	H_2O (%)	N_2 (%)
Sulfur aging test									
Lean	0	0	0	0	11	50	6.5	3	Balance
Rich	0	6	2	0	11	0	0	3	Balance
NO_x storage measurement									
Lean	0.06	0	0	400	11	0	7	5	Balance
Rich / Rich Spike	0.32	6	1.6	400	11	0	0	5	Balance

The residual amount of sulfur in the sulfur-aged monolithic catalysts was measured using a combustion infrared absorption analyzer (Horiba, EMIA-1200). After the sulfur-aging test, mapping of the residual S in the wash-coat layer was carried out by electron probe micro analysis (EPMA) using an electron probe micro analyzer (Shimadzu, EPMA-V6). The ratio of S to Ba in the sulfur-aged AZT catalyst powder was analyzed using an energy-dispersive X-ray (EDX) analyzer equipped with a field-emission transmission electron microscope (Hitachi, HF-2000). The diameter of the EDX analysis area was approximately 10 nm. The analyzed part contained a Pt particle and neighboring barium species. The ratio of S to Ba was observed as a function of the distance from a Pt particle. The state of the storage material was analyzed using the same method as that described in section 2.2. The states of the potassium species were as follows: the active state, K_2CO_3, the sulfate state, K_2SO_4, and the solid phase-reacted state with support materials, mainly TiO_2 [7]. The barium species were classified as the active state, $BaCO_3$, and the other states, including the sulfate-formed state and the solid phase-reacted state, as described in the literature [8].

3. Results and Discussion

3.1. Effect of AZT calcination temperature on thermal stability

In order to confirm the most thermally stable AZT structure, five samples calcined at different final temperatures were synthesized. The specific surface areas (SSAs) of AZT calcined from 773 K to 1173 K are shown in Table 3. These samples were evaluated as NSR catalysts composed of Pt/Rh/Ba/K/AZTn after thermal aging at 1073 K. The SSAs of catalysts after thermal aging are also shown in Table 3. Figure 1 shows the NO_x storage capacities of pelletized catalysts at 573, 673 and 773 K after thermal aging.

Table 3. SSA of AZTn as prepared and their catalysts after thermal aging.

	Calcination temperature (K)	SSA (m^2/g)	SSA of P-AZTnCat after thermal aging (m^2/g)
AZT773	773	277	46.7
AZT873	873	224	50.0
AZT973	973	195	51.2
AZT1073	1073	128	58.1
AZT1173	1173	80	53.8

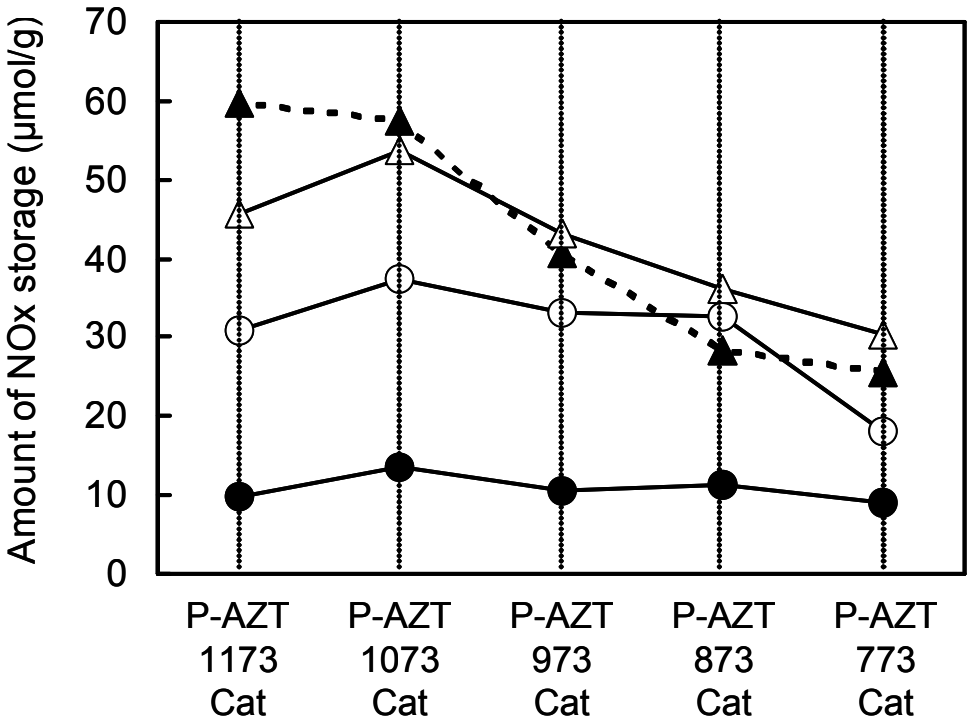

Fig. 1. NO_x storage using AZT catalysts after thermal aging as a function of specific surface area of supports.

●: NO_x storage measured at 573 K, ○: 673 K, Δ: 773 K after thermal aging, ▲: 773 K after sulfur aging.

At 673 and 773 K, NSR performance is almost proportional to the size of SSA of catalysts after thermal aging. The P-AZT1073Cat shows the maximum NO_x storage especially at 673 and 773 K. This maximal storage capacity can be attributed to the structure of AZT1073, because structural changes tend to occur depending on the calcination temperature. Therefore, powder XRD patterns of AZTn were analyzed and these are shown in Fig. 2. The tetragonal ZrO_2 peak derived from ZT starts to appear weakly at 973 K, and then becomes clearly sharp at 1073 K or higher, demonstrating that ZT in AZT1073 is both crystallized completely and stable at high temperatures.

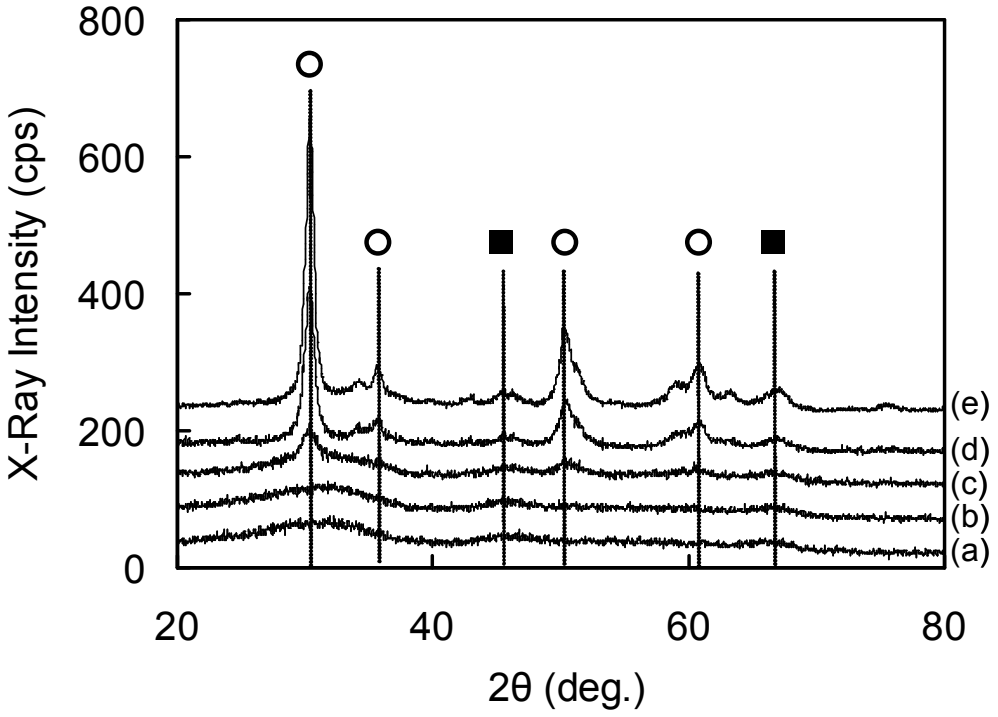

Fig. 2. XRD patterns of AZT at various calcination temperatures. (a) AZT773, (b) AZT873, (c) AZT973, (d) AZT1073, (e) AZT1173. ○: tetragonal ZrO_2 and ■: γ-Al_2O_3.

The crystallization of ZT has been reported to start at temperatures lower than 923 K, and catalysts containing ZT, which calcined at 923 K, have been shown to exhibit considerably high NO_x storage performance [25]. Therefore, since it could be inferred that the crystallization process for ZT in AZT was different to that in pure ZT, the XRD pattern of AZT1073 was compared with the pure ZT powder calcined from 873 K to 1073 K. The XRD patterns around the tetragonal ZrO_2 (101) peak at $2\theta = 30.4°$ of AZT 1073 and pure ZT are shown in Fig. 3. The particle size of ZT calculated from the XRD results is shown in Table 4. The particle size of ZT in AZT1073 is less than half of that of pure ZT calcined at the same temperature and corresponds to the particle size of pure ZT calcined between 873 K and 923 K. These findings show that AZT1073 can be crystallized and that it forms a stable structure with maximal NSR performance. The small size of ZT corroborates the finding that AZT inhibits sintering of ZT [22], because Al_2O_3 acts as a diffusion barrier to ZT particles. In AZT1173, although ZT has already crystallized, the SSA is 40 % smaller than the AZT1073. Furthermore, the SSA of P-AZT1173Cat is also smaller than P-AZT1073Cat after thermal aging, as shown in Table 3. Once AZT has crystallized thoroughly, NSR performance is presumed to be proportional to the size of the SSA after thermal aging, as this affects the number of catalytic active sites.

Furthermore, the amount of NOx storage of P-AZT1073Cat at 673 and 773 K is distinctly larger than that of other samples. The main reason of deactivation of storage materials after thermal aging is the deterioration of potassium, and potassium works as a NOx storage material around this temperature region [26, 27]. Compared with amorphous ZT, there is a possibility that crystallized ZT is stabilized, thus inhibiting the solid phase reaction with potassium. In order to confirm this point, the P-AZT1073Cat was selected for a crystallized AZT support, and the P-AZT773Cat for a amorphous AZT support. As a

result, the ratio of solid phase-reacted potassium for the P-AZT1073Cat was 22 %, whereas that of P-AZT773Cat was 52 %. The primary source for the solid phase reaction with potassium is TiO_2 [7]. The ZT in AZT773 is amorphous and tends to induce a solid phase reaction with storage materials. Therefore, the initial reason for the high NSR performance of the P-AZT1073Cat at 773 K is the difference in the amount of deactivated potassium, because AZT1073 inhibits the reaction of storage materials with TiO_2 based on the crystallization of ZT. This result is also one of the reasons why P-AZT1073Cat has the largest SSA in spite of the same thermal aging condition for all samples.

Although the P-AZT1073Cat has the best NSR performance relative to thermal stability, it also requires durability with respect to sulfur if it is to be applied as an NSR catalyst. The NO_x storage capacities of catalysts using AZT calcined at different temperatures were measured after sulfur aging. The solid triangles joined by the dotted line in Fig. 1 show the amount of NO_x storage measured at 773 K after sulfur aging. The P-AZT1073Cat has a larger NO_x storage capacity than P-AZT773, 873 and 973Cats after sulfur aging. Sulfur durability is related to the basicity of supports [7], and acidic metal oxides with low basicity, such as TiO_2, show excellent sulfur durabilities due to the facilitation of the decomposition of sulfate materials [7,8]. AZT contains TiO_2 as ZrO_2-TiO_2 solid solution. However, basicity may change depending on the calcination temperature, followed by the change of the NSR performance. Using CO_2-TPD, the basicities of AZT773 and 1073 were determined to be 10.8 μmol/g and 2.7 μmol/g, respectively. Therefore, the main reason of excellent NSR performance of the P-AZT1073Cat after sulfur aging is thought to be its low basicity.

These results suggest that AZT1073 is structurally well suited for NSR performance, exhibiting both thermal stability and sulfur durability. For this reason, AZT1073 was used as the standard AZT support in the following section.

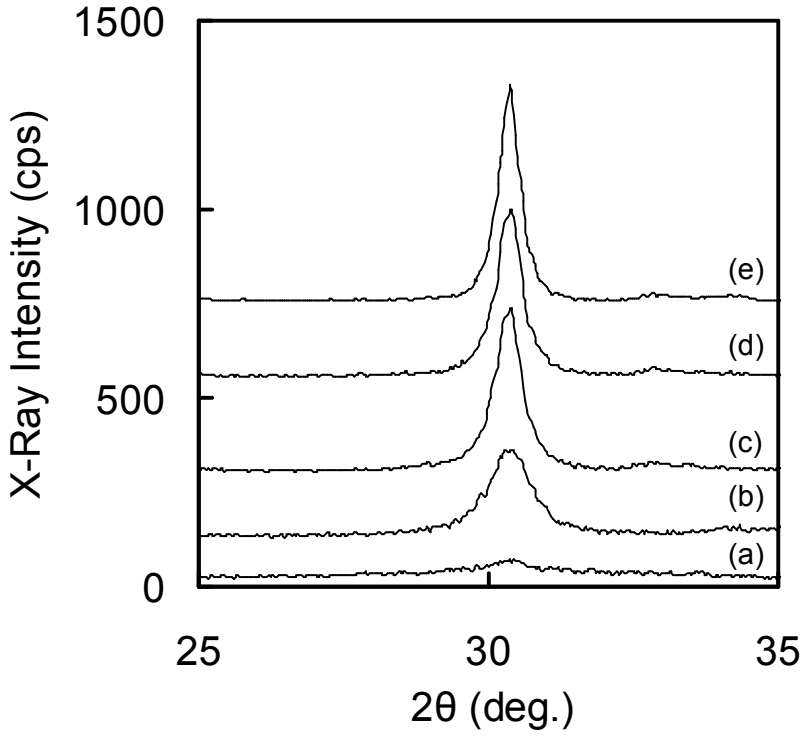

Fig. 3. XRD patterns of AZT1073 and a solid solution of pure ZrO_2-TiO_2 at various calcination temperatures. (a) 873 K (b) AZT1073 (c) 923 K (d) 973 K (e) 1073 K

Table 4. Particle size of ZT calcined at various temperatures.

Temperature (K)	ZT particle size (nm)
1073 (AZT)	10
873	-
923	14
973	17
1073	24

3.2. Analysis of the AZT catalyst for sulfur durability

3.2.1. NSR performance after sulfur aging at high temperature

NSR catalysts become deactivated through the complex processes of thermal deterioration and sulfur poisoning. Therefore, monolithic catalysts were aged at 973 K or higher under the model exhaust gas atmosphere with SO_2, and exposed to a feed-stream alternating between rich and lean atmospheres to desorb and decompose the sulfur species. AZT is a nanocomposite of Al_2O_3 and ZT primary particles within the same secondary particle. Therefore, a catalyst with a physical mixture of Al_2O_3 and ZT as a support was selected as the reference catalyst to confirm the effect of the nanocomposite structure of AZT on sulfur durability.

Figure 4 shows the NO_x storage capacity measured at 673 K in the monolithic AZT catalyst and the physically mixed catalyst after sulfur aging at 973, 1023, and 1073 K. The monolithic AZT catalyst has a larger NO_x storage capacity than the physically mixed catalyst at each temperature, although the amount of NO_x storage decreased with an increase in the aging temperature. This increased storage capacity was attributed to the unique structure of AZT. One such quality is the diffusion barrier of Al_2O_3 to ZT, which provides thermal stability [22] and low basicity for sulfur durability [18]. One critical difference observed between the monolithic AZT catalyst and the physically mixed catalyst can be seen in the deteriorated state of the NO_x storage materials, which, at 673 K, reflects the performance of both potassium and barium storage materials. Potassium stores NO_x as potassium nitrate above 623 K, whereas barium stores NO_x as barium nitrate in the low temperature region from 573 to 723 K [26,27]. Therefore, analysis and characterization of NO_x storage materials after aging must be conducted in order to understand the mechanism of optimal performance of the monolithic AZT catalyst.

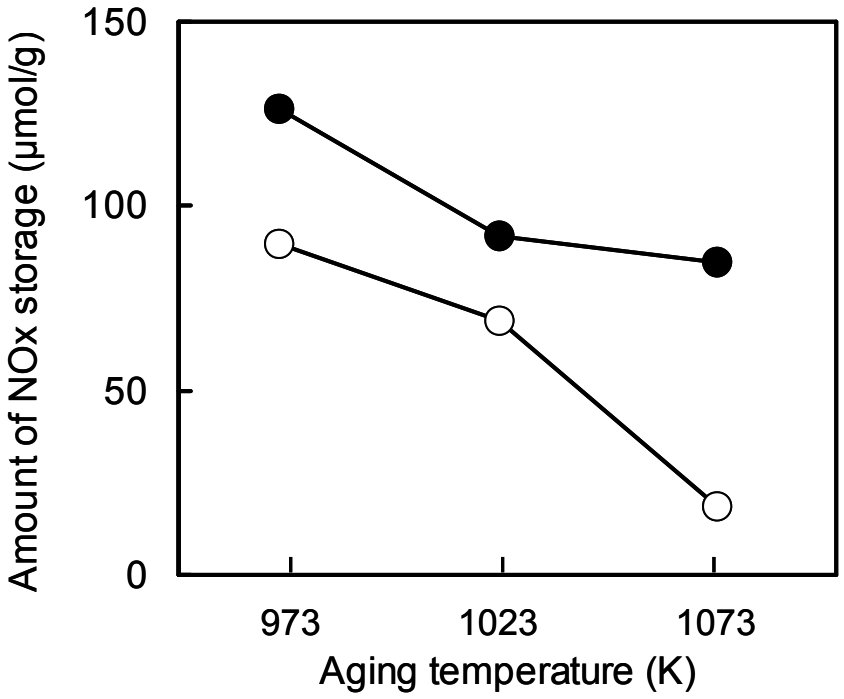

Fig. 4. NO_x storage after sulfur aging as a function of aging temperature. ●: monolithic AZT catalyst, ○: monolithic physically mixed catalyst.

3.2.2. Analysis of potassium species

The deteriorated states of NO_x storage materials were classified as the active state, which is capable of storing NO_x, the solid phase-reacted state, which arises due to the thermal reaction between storage materials and support materials, and the sulfate-formed state, which arises due to sulfur poisoning.

Table 5 shows the state of potassium in monolithic catalysts after aging at 1023 and 1073 K. The amount of active potassium in the monolithic AZT catalyst is larger than

that in the physically mixed catalyst when samples were aged at 1023 K. The ratio of the solid phase reacted potassium in the monolithic AZT catalyst is almost half that in the physically mixed catalyst. Therefore, the primary reason for the large amount of active potassium in the monolithic AZT catalyst was attributed to the small amount of the solid phase reacted potassium. This trend remained even after aging at 1073 K, and also led to high NO_x storage performance of the monolithic AZT catalyst. The monolithic AZT catalyst inhibits the formation of solid phase reacted potassium at high temperatures, because the ZT phase has already been stabilized, as described in section 3.1. The ratio of sulfate-formed potassium was relatively small for both samples, although the ratio decreased with an increase in aging temperature. Therefore, the primary reason for potassium deterioration at high temperatures was attributed to thermal deterioration, and the difference in the amount of solid phase-reacted potassium affected the NSR performance.

Interestingly, the EPMA results reveal that potassium species easily move to the monolith substrate in the physically mixed catalyst with an increase in the aging temperature. The physically mixed oxide has a broad pore distribution relative to AZT, and a macropore around 60 nm was observed after calcination at 1073 K due to the sintering of ZT. On the other hand, AZT was shown to form a single mesopore measuring approximately 15 nm [22]. These results indicate that potassium can easily move outside the catalyst layer and that the total amount of potassium species contained in the catalyst layer in the physically mixed catalyst was less than that added in catalyst preparation. This suggests that the amount of active potassium in the physically mixed catalyst is less than that shown in Table 5. This trend also contributes to the difference in the amount of NO_x storage for the monolithic AZT catalyst and the physically mixed catalyst.

Table 5. The state of potassium in monolithic catalysts after sulfur aging test at high temperature

Sulfur aging temperature	Catalyst	Active pottasium (%)	Solid phase reacted pottasium (%)	Sulfate formed pottasium (%)
1023 K	Monolithic AZT	84	9	7
	Physically mixed	78	17	5
1073 K	Monolithic AZT	85	13	2
	Physically mixed	78	20	2

3.2.3. Analysis of barium species

The state of barium in the samples after sulfur aging is shown in Table 6. The ratio of active barium in the monolithic AZT catalyst was larger than that in the physically mixed catalyst at both aging temperatures. Moreover, compared with the physically mixed catalyst, the AZT catalyst had twice the amount of active barium after aging at 1023 K effectively increasing the NO_x storage capacity of the monolithic AZT catalyst.

Table 6. The state of barium in monolithic catalysts after sulfur aging test at high temperature

Sulfur aging temperature	Catalyst	Active barium (%)	Other barium (%)
1023 K	Monolithic AZT	35	65
	Physically mixed	16	84
1073 K	Monolithic AZT	31	69
	Physically mixed	22	78

Further characterization of the barium species may be useful to elucidate the mechanism of action. In order to further examine the barium species, the sulfur species were identified because, as shown in Table 5, sulfur poisoning in potassium species is almost negligible. The adsorption of sulfur species on the support surface is thought to be negligible in this aging temperature region [8,18]. In addition, since the barium component in $Ba/CeO_2/Al_2O_3$ is also known to be selectively poisoned by sulfur [28], it is possible to consider that the difference in sulfur poisoning reflects the barium state for each catalyst.

The residual sulfur after sulfur aging is shown in Fig. 5. The sulfur content in the monolithic AZT catalyst is less than that in the physically mixed catalyst. Specifically, the amount of sulfur in the monolithic AZT catalyst is less than half of that of the physically mixed catalyst at more than 1023 K. While sulfur was also observed in the catalysts layered on the monolithic substrate using EPMA (Fig. 6), almost no sulfur was detected in the AZT catalyst after the sulfur-aging test at 1023 K. The low basicity of AZT surface facilitates facile desorption and degradation of sulfated materials during the alternating lean and rich atmosphere gas conditions [18]. Therefore, the difference in the basicities of AZT and the physically mixed oxide may be one reason why a large amount of active barium is maintained in the AZT catalyst.

Figure 7 shows the sulfur to barium ratio in relation to the distance from a Pt particle observed in the monolithic AZT catalyst after the sulfur-aging test at 1023 K. The S/Ba ratio increases with distance from the Pt particle, because the decomposition of sulfates includes the reduction of SO_4^{2-} to SO_2, which is catalyzed by Pt [8]. In Chapter 2, the dispersion of noble metals in the AZT catalyst was reported to be twice that in the physically mixed catalyst after thermal aging at 1073 K [22]. This is because AZT inhibits sintering and aggregation of ZT and maintains a stable surface. Consequently,

recovery from barium sulfate to active barium in NO_x storage is facilitated by the AZT support, which may contribute to the large amount of active barium in the monolithic AZT catalyst.

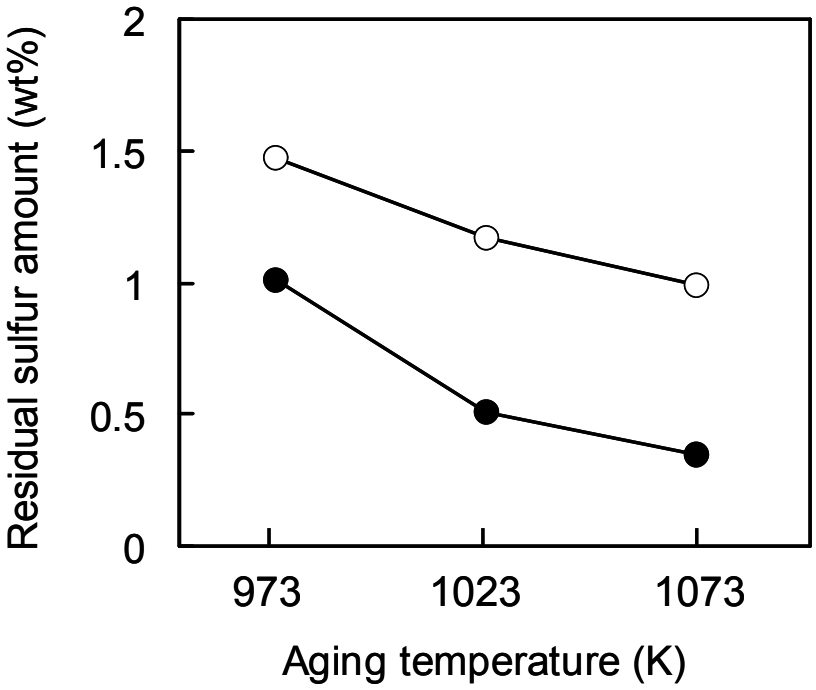

Fig. 5. Residual sulfur after sulfur aging as a function of aging temperature. ●: monolithic AZT catalyst, ○: monolithic physically mixed catalyst.

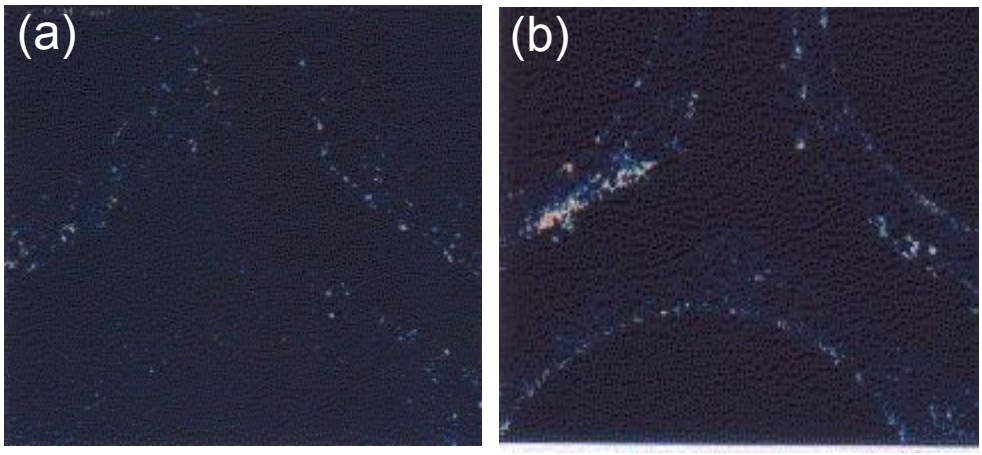

Fig. 6. EPMA images of S atom in the wash-coat layer after sulfur aging at 1023 K. (a) monolithic AZT catalyst, (b) monolithic physically mixed catalyst.

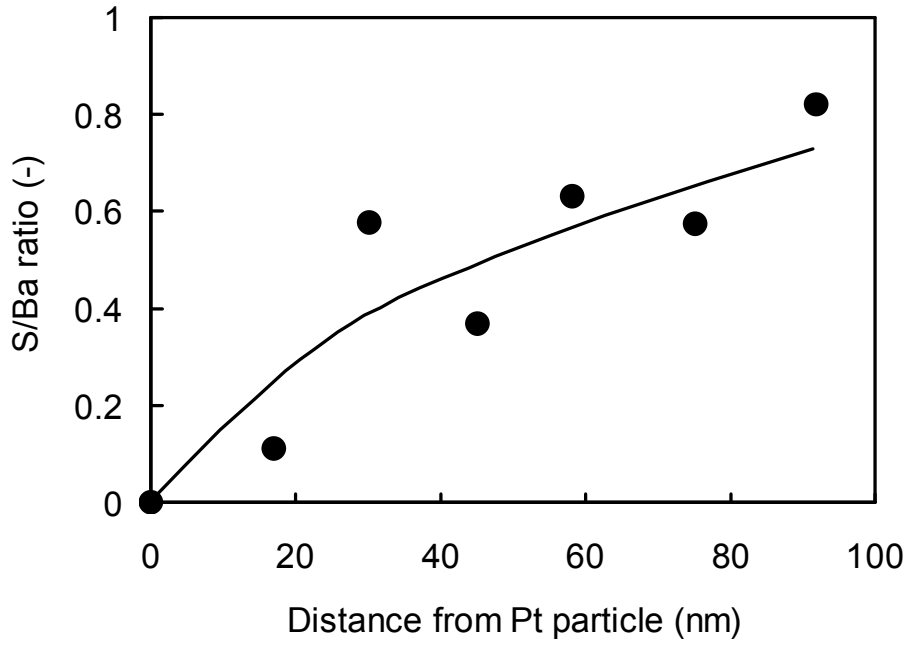

Fig. 7. Relationship between S/Ba ratio and distance from Pt particle in AZT catalyst after sulfur aging.

4. Conclusions

The effect of calcination temperature of AZT was investigated to assess the thermal stability of NSR catalysts. AZT calcined at 1073 K showed significant NO_x storage ability after thermal aging as a catalyst, because the ZT phase was already crystallized and thermally stable. Therefore, the solid phase reaction of potassium with support materials was inhibited, and a high ratio of active potassium remained in the AZT catalyst at 1073 K.

The AZT catalyst showed superior NO_x storage performance after sulfur aging at 973 K or higher compared to that of the physically mixed catalyst. The monolithic AZT catalyst inhibited the solid phase reaction of potassium with support materials and a high ratio of active potassium was maintained. In addition, barium in the monolithic AZT catalyst prevented sulfur poisoning and maintained NO_x storage based on low basicity and high Pt dispersion. Given the optimal balance that exists between thermal stability and sulfur durability, AZT calcined at 1073 K is a promising support for NSR catalysts.

Acknowledgements

The author thanks Mr. Yuzo Kawai for ICP analysis, Mr. Yasuhito Kondou for conducting the combustion infrared absorption analyses, and Ms. Kumi Amano for S atom mapping by EPMA.

References

[1] S. Sato, Y. Yu-u, H. Yahiro, N. Mizuno, M. Iwamoto, *Appl. Catal.* 70 (1991) L1.

[2] Y. Kintaichi, H. Hamada, M. Tabata, M. Sasaki, T. Ito, *Catal. Lett.* 6 (1990) 239.

[3] R. Burch, P. J. Millington, *Catal. Today* 26 (1995) 185.

[4] T. Ishihara, M. Ando, K. Sada, K. Takiishi, K. Yamada, H. Nishiguchi and Y. Takita, *J. Catal.* 220 (2003) 104.

[5] N. Miyoshi, S. Matsumoto, K. Katoh, T. Tanaka, J. Harada, N. Takahashi, K. Yokota, M. Sugiura, K. Kashahara, *SAE Paper 950809*, 1995.

[6] N. Takahashi, H. Shinjoh, T. Iijima, T. Suzuki, K. Yamazaki, K. Yokota, H. Suzuki, N. Miyoshi, S. Matsumoto, T. Tanizawa, T. Tanaka, S. Tateishi, K. Kasahara, *Catal. Today* 27 (1996) 63.

[7] N. Takahashi, A. Suda, I. Hachisuka, M. Sugiura, H. Sobukawa, H. Shinjoh, *Appl. Catal. B: Environ.* 72 (2006) 187.

[8] S. Matsumoto, Y. Ikeda, H. Suzuki, M. Ogai, N. Miyoshi, *Appl. Catal. B: Environ.* 25 (2000) 115.

[9] E. C. Corbos, X. Courtois, N. Bion, P. Marecot, D. Duprez, *Appl. Catal. B: Environ.* 80 (2008) 62.

[10] X. Wei, X. Liu, M. Deeba, Appl. *Catal. B: Environ.* 58 (2005) 41.

[11] J. Dawody, M. Skoglundh, L. Olsson, E. Fridel, *Appl. Catal. B: Environ.* 70 (2007) 179.

[12] Z. Liu, J. Anderson, *J. Catal.* 228 (2004) 243.

[13] J. H. Kwak, D. H. Kim, J. Szanyi, C. H. F. Peden, *Appl. Catal. B: Environ.* 84 (2008) 545.

[14] S. Hammache, L. R. Evans, E. N. Coker, J. E. Miller, *Appl. Catal. B: Environ.* 78 (2008) 315.

[15] K. Yamamoto, R. Kikuchi, T. Takeguchi, K. Eguchi, *J. Catal.* 238 (2006) 449.

[16] T. Kanazawa, *Catal. Today* 96 (2004) 171.

[17] K. Ito, S. Kakino, K. Ikeue, M. Machida, *Appl. Catal. B: Environ.* 74 (2007) 137.

[18] H. Imagawa, T. Tanaka, N. Takahashi, S. Matsunaga, A. Suda, H. Shinjoh, *Appl. Catal. B: Environ.* 86 (2009) 63.

[19] K. M. Adams, G. W. Graham, *Appl. Catal. B: Environ.* 80 (2008) 343.

[20] M. Casapu, J. Grunwaldt, M. Maciejewski, M. Wittrock, U. Göbel, A. Baiker, *Appl. Catal. B: Environ.* 63 (2006) 232.

[21] N. Takahashi, S. Matsunaga, T. Tanaka, H. Sobukawa, H. Shinjoh, *Appl. Catal. B: Environ.* 77 (2007) 73.

[22] H. Imagawa, T. Tanaka, N. Takahashi, S. Matsunaga, A. Suda, H. Shinjoh, *J. Catal.* 251 (2007) 315.

[23] J. A. Anderson, R. A. Daley, S. Y. Christou, A. M. Efstathiou, *Appl. Catal. B: Environ.* 64 (2006) 189.

[24] N. Takahashi, K. Yamazaki, H. Sobukawa, H. Shinjoh, *J. Chem. Eng. Jpn.* 39 (2006) 437.

[25] Y. Liu, M. Meng, X.G. Li, L.H. Guo and Y.Q. Zha, *Chem. Eng. Res. Des.* 86 (2008), 932.

[26] I. Hachisuka, T. Yoshida, H. Ueno, N. Takahashi, A. Suda, S. Sugiura, *SAE paper* 2002-01-0732, 2002.

[27] M. Takeuchi, S. Matsumoto, *Top. Catal.* 28 (2004) 151.

[28] F. Rohr, S.D. Peter, E. Lox, M. Kögel, A. Sassi, L. Juste, C. Rigaudeau, G. Belot, P. Gelin and M. Primet, *Appl. Catal. B: Environ.* 56 (2005), 201.

Chapter 4

The effect of titanium-doping in AZT on sulfur durability for NO_x storage reduction catalyst

Abstract

A nanocomposite of Al_2O_3 and a ZrO_2-TiO_2 solid solution (AZT) doped with Ti (Ti-AZT) was synthesized as a support for a NO_x storage-reduction (NSR) catalyst in order to achieve sulfur durability. Ti-AZT maintained the original structure of AZT after the Ti doping step and exhibited lower basicity. Energy dispersive X-ray spectroscopy revealed that the Ti concentration on the Al_2O_3 particles was more than 10 atom% on average for a sample containing 3.3 atom% of doped titanium. Doped titanium was homogeneously distributed on the surface without the formation of isolated TiO_2 particles. SO_2-temperature programmed desorption at less than 823 K indicated that the catalyst containing Ti-AZT had larger sulfur desorption than that containing AZT. After sulfur aging tests, the Ti-AZT catalyst provided a large amount of NO_x storage. The improved sulfur durability in the NSR catalyst resulted from the presence of TiO_2 as a Al_2O_3-TiO_2 solid solution in Ti-AZT.

1. Introduction

The lean-burn engine system is one of the most attractive methods to reduce the emission of carbon dioxide (CO_2) from vehicles, with regard to global environmental practices. However, in this system, conventional three-way catalysts cannot reduce nitrogen oxides (NO_x) into nitrogen (N_2) under lean conditions, because excess oxygen is present in the exhaust gases. Therefore, a number of challenging catalyst systems have been developed to reduce NO_x in lean systems [1-3].

The NO_x storage-reduction catalyst (NSR catalyst) has been proposed as one of the promising methods for the purification of NO_x from lean-burn engines [4-6]. But the NSR catalyst has two main technical problems as shown in the introduction in Chapter 2 and 3: sulfur poisoning and thermal deterioration. Sulfur poisoning is caused by the presence of sulfur dioxide (SO_2) in the gas exhaust. SO_2 adsorbs onto the catalysts and then reacts with the storage materials. Finally, the catalysts cannot store NO_x, due to the formation of sulfates. In an attempt to solve this problem, the effect of sulfur on storage materials has been well studied [7-11]. Recent studies on sulfur durability in catalysts have reported that TiO_2 in support materials provides high tolerance against sulfur poisoning, due to its high acidity/low basicity [6,7,12-14]. TiO_2 is often contained in the ZrO_2-TiO_2 solid solution to prevent the solid-phase reaction of the NO_x storage materials with TiO_2 under heating [6,13]. The properties of ZrO_2-TiO_2 have also been well demonstrated in terms of weak basicity [6,14].

Thermal deterioration of the catalyst occurs due to aggregation of the support particles and precious metals [15], in addition to the solid-phase reaction of the NO_x storage materials [16,17]. Therefore, Al_2O_3 is added to the support, because of its excellent thermal stability. A nanocomposite of Al_2O_3 and ZrO_2-TiO_2 (AZT) as a support

has been developed as shown in Chapter 2 and 3. In this nanocomposite, Al_2O_3 primary particles and ZrO_2-TiO_2 primary particles coexist within the same secondary particle. AZT has been shown to inhibit the thermal aggregation of ZrO_2-TiO_2, because Al_2O_3 acts as a diffusion barrier to ZrO_2-TiO_2 particles in the form of secondary particles [18]. Particle growth of not only ZrO_2-TiO_2, but also of precious metals on the supports is prevented, and high NSR performance is achieved. Furthermore, AZT has been found to have low basicity, which is expected, due to the presence of the small amount of TiO_2 in Al_2O_3. Therefore, the NSR catalyst containing AZT as a support is expected to exhibit not only excellent thermal stability, but also higher sulfur durability, because all of the particles contain TiO_2. It is also postulated that the additional presence of TiO_2 on AZT may actively enhance sulfur durability.

The purpose of this investigation is to improve the sulfur durability of NSR catalyst supports. In this investigation, the sulfur durability of AZT was verified, and the effect of titanium doping (presence of TiO_2 onto AZT) on sulfur durability was examined.

2. Experimental

2.1. Preparation of supports

AZT was prepared by a conventional coprecipitation method [18]. The mole ratio of Al_2O_3:ZrO_2:TiO_2 was 50:30:20 (mol%).

Titanium-doped AZT (Ti-AZT) was synthesized by impregnation with titanium citrate [19]. AZT was added to an aqueous solution of titanium citrate and the solution was then evaporated at 373 K. The obtained product was then calcined at 1073 K for 5 h in air. The amount of doped Ti was 3.3 atom%, based on the metal atom composition of Ti-AZT (3.3 atom% Ti-AZT). 3.3 atom% Ti-AZT was used as the standard sample for all experiments. The final mole ratio of Al_2O_3:ZrO_2:TiO_2 was 48.3:28.0:23.7 (mol%). To clarify the dependency of the structural change on the amount of titanium added, Ti-AZT with 1.6 and 6.2 atom% of doped titanium (1.6/6.2 atom% Ti-AZT, respectively) were also synthesized as reference samples.

Pure γ-Al_2O_3 was prepared by the same method as that used for AZT. Pure ZrO_2-TiO_2 was prepared by the same method, as reported in literature [6]. A reference support was obtained by physically mixing pure γ-Al_2O_3 and ZrO_2-TiO_2 (physically mixed oxide). The composition of the physically mixed oxide was the same as that of AZT.

2.2. Characterization of Ti-AZT

The crystal structures were characterized by powder X-ray diffraction (XRD). XRD patterns were recorded using a Rigaku RINT-2100 (Cu Kα radiation λ= 1.5418 Å, 40 kV, 30 mA). To analyze the distribution of doped titanium and the composition of Al, Zr and Ti, field-emission transmission electron microscopy (FE-TEM) and energy

dispersive X-ray analysis (EDX) were performed using a Hitachi HF-2000. The diameter of the EDX analysis area was approximately 1 nm. The Brunauer-Emmett-Teller (BET) surface area was measured by N_2 adsorption at 77 K using a Micro Data, Micro Sorp 4232II. The pore size distribution was calculated from the intrusion curve obtained by mercury porosimetry using a Quantachrome Pore Master GT60-1.

The surface base properties of the supports were measured by CO_2-temperature programmed desorption (CO_2-TPD). Samples were formed into 0.3-0.7 mm diameter pellets. For CO_2-TPD, samples were pretreated at 773 K under a He atmosphere. After the samples were exposed to CO_2 in a stream of He at 373 K, they were heated to 773 K at a rate of 20 K/min. CO_2 desorbed from samples under a N_2 atmosphere was observed using a non-dispersive infrared (NDIR) analyzer attached to a Horiba MEXA-7100 exhaust gas evaluation system.

To investigate the thermal stability, samples were heated at 1073, 1173 and 1273 K for 5 h in air containing 3% water. The crystal structure after this thermal treatment was then analyzed using XRD and the particle size of ZrO_2-TiO_2 was calculated using Scherrer's formula [20]. The peak at $2\theta = 30.4°$, assigned to the tetragonal ZrO_2 (101) phase, was used to calculate the particle size of ZrO_2-TiO_2. The BET surface area was also measured at each thermal treatment temperature by N_2 adsorption at 77 K using a Micro Data, Micro Sorp 4232II.

2.3. Sulfur desorption test

Catalysts were prepared by impregnating $Pt(NH_3)_2(NO_2)_2$ and $Rh(NO_3)_3$ (Tanaka Precious Metals), then dried at 383 K for 12 h, and finally calcined at 523 K for 3 h in air. The amount of Pt and Rh loading was 1.23 and 0.06 wt%, respectively. The powder obtained was then added to an aqueous solution containing $(CH_3COO)_2Ba$ and

CH_3COOK (Wako Pure Chemical Industries) as precursors to the storage materials. The loading amounts of barium as BaO and potassium as K_2O were 18.8 and 5.8 wt%, respectively. After the catalysts were dried at 383 K for 12 h, they were calcined at 773 K for 3 h in air. The powder obtained was formed into 0.3-0.7 mm diameter pellets.

For the sulfur desorption tests at fixed temperature, the catalysts were exposed to the SO_2 adsorption gas atmosphere (Table 1) for 30 min at 823, 873 and 923 K. After the condition was switched to the SO_2 desorption gas atmosphere, the sulfur species desorbed from the catalysts were measured using a Best Sokki Bex-5900 with a flame photometric detector (FPD) at fixed temperature.

For SO_2-TPD, catalysts were exposed to a SO_2 adsorption gas atmosphere (Table 1) at 873 K for 30 min. After the samples were cooled to 373 K, they were heated to 1023 K at a rate of 15 K/min under the SO_2 desorption gas atmosphere. The sulfur species desorbed from catalysts were measured using a FPD.

Both desorption experiments detailed above were performed under the same gas conditions. The gas flow rate was 4000 cm^3/min for the adsorption step and 3000 cm^3/min for the desorption step. The gas hourly space velocities (GHSV) were 240 000 h^{-1} and 180 000 h^{-1} for the adsorption and desorption steps, respectively. The mole ratio of SO_2 to the storage materials was S/(Ba+0.5K) = 1.4. All the SO_2 was adsorbed on the catalysts under these conditions.

The residual amount of sulfur deposit in the SO_2 aged catalysts was measured using a combustion infrared absorption analyzer (Horiba EMIA-1200). The SO_2 aged sample was prepared at 873 K by switching the lean and rich gas atmospheres (Table 1) every 30 s with 1000 ppm SO_2. The mole ratio of SO_2 to the storage materials was S/(Ba+0.5K) = 1.5.

Table 1. Gas composition for Sulfur desorption test at fixed temperature, SO_2-TPD, and NOx storage measurement.

Atmosphere	C_3H_6 (%C)	CO (%)	H_2 (%)	NO (ppm)	CO_2 (%)	SO_2 (ppm)	O_2 (%)	H_2O (%)
Sulfur desorption test and SO_2 -TPD [a]								
SO_2 adsorption	0	0	0	0	0	400	6.6	3
SO_2 desorption	0.34	5.6	1.9	50	11	0	0	3
NO_x storage measurement [b]								
Lean	0.02	0	0	800	11	0	6.6	3
Rich	0.11	5.6	1.9	0	11	0	0.3	3
Rich Spike	0.11	5.6	1.9	50	11	0	0	3

[a] N_2 balance. [b] He balance.

2.4. NOx storage measurement after the sulfur aging test

Catalysts were prepared in the same manner as the method given in section 2.3. The sulfur aging test was carried out at 873 K under the SO_2 adsorption gas atmosphere shown in Table 1. The gas flow rate was 4000 cm^3/min and the GHSV was 240 000 h^{-1}. The mole ratio of SO_2 to storage materials was S/(Ba+0.5K) = 1.4.

The amount of NO_x stored in the sulfur-aged catalysts was measured using a conventional fixed-bed flow reactor system at atmospheric pressure. Table 1 shows the composition of the feedstreams used to simulate actual engine exhaust gases for this measurement. After the catalyst was exposed to a rich atmosphere at 873 K for 5 min as the pretreatment, the catalyst was cooled to 573 K under the rich atmosphere. The gas was

switched to the lean atmosphere until the outlet NO_x concentration reached a constant value, and then a 3 s rich spike was introduced to the catalyst. Subsequently, the gas was switched to the lean atmosphere until the outlet NO_x concentration reached a constant value. The amount of NO_x stored was calculated as the difference in the NO_x amount between the inlet and the outlet gases after the rich spike.

The amounts of NO_x stored at 673 and 773 K were measured in the same manner as for 573 K, and these measurements were carried sequentially after the experiment at 573 K. The gas flow rate was 3000 cm^3/min and the GHSV was 180 000 h^{-1}. The NO_x concentration was measured using a chemiluminescence NO_x meter attached to a Horiba MEXA-7100 gas exhaust evaluation system.

3. Results and discussion

3.1. Effect of TiO_2 on sulfur desorption in AZT

3.1.1. EDX analysis of titanium on Al_2O_3 in AZT

AZT has low basicity [18]; therefore, it may be inferred that this low basicity results from the presence of a small amount of TiO_2 on Al_2O_3, because TiO_2 has high acidity/low basicity. To confirm this, EDX analysis of an Al_2O_3 primary particle in AZT was carried out.

The compositions shown in Table 2 are from three selected analysis spots of randomly sampled Al_2O_3 primary particles. Ti was observed in all the analysis spots. Zr was also detected in several spots, but the amount of Zr was smaller than that of Ti. The original Zr concentration in AZT was larger than the Ti concentration. Therefore, small amounts of Ti tend to be present in the Al_2O_3 primary particles, due to the coprecipitation

synthesis step. Ti is thought to be present as an Al_2O_3-TiO_2 solid solution, because discrete TiO_2 particles were not observed on the Al_2O_3 particles by TEM and XRD examination [18]. Furthermore, a small amount of TiO_2 is soluble in Al_2O_3 [21,22].

This support structure suggests that it is possible to inhibit the adsorption of SO_x onto the surface. The desorption of sulfur compounds will be also easily promoted under a rich condition after SO_x adsorption onto the surface [23].

Table 2. Ti/Zr/Al composition on Al_2O_3 primary particles of AZT and Ti-AZT observed in EDX analysis.

	Composition (atom%)		
	Ti	Zr	Al
AZT			
Spot 1	1.6	0	98.4
Spot 2	4.0	2.5	93.5
Spot 3	3.8	2.4	93.8
Ti-AZT			
Spot 1	11.6	1.6	86.8
Spot 2	11.5	1.8	86.7
Spot 3	12.6	3.7	83.7

3.1.2. Sulfur desorption test

In practical use, the NSR catalyst is exposed to SO_2. To confirm the effect of the presence of TiO_2 in Al_2O_3 on the sulfur durability, the desorption of sulfur from catalysts was observed at a fixed temperature. Figure 1 shows the amounts of sulfur desorption at each measured temperature. For all temperatures, the AZT catalyst had a larger amount of sulfur desorption than the catalyst containing the physically mixed oxide. In particular, AZT showed a larger amount of sulfur desorption at less than 873 K. The sulfur desorption at less than 873 K mainly corresponds to desorption from the surface of the support [7]. Therefore, SO_2 adsorbed onto the AZT catalyst is easily desorbed at low temperature, because of the lower basicity as the effect of the presence of TiO_2 on the Al_2O_3 surface emerges.

On the basis of this result, Ti-AZT was conceptualized and synthesized in order to enhance the total sulfur durability.

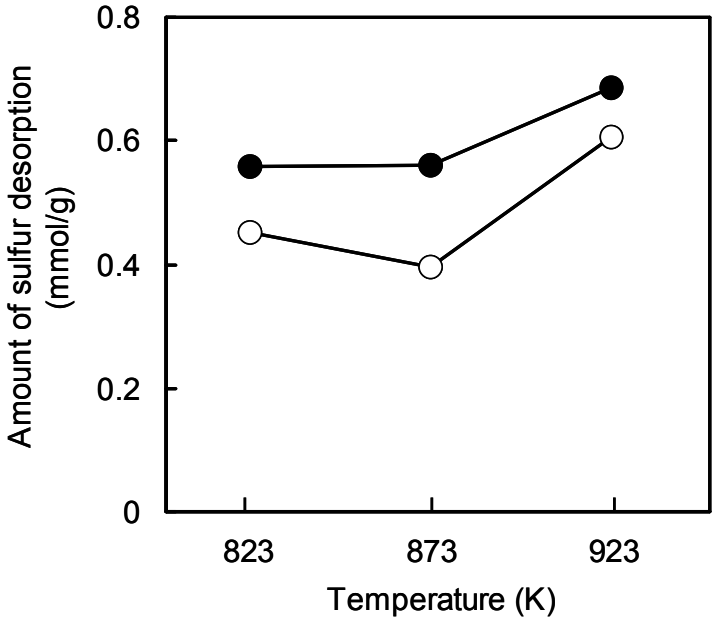

Fig. 1. Amount of sulfur desorption from NSR catalysts at a fixed temperature. (●) AZT catalyst, (○) physically mixed catalyst.

3.2. Characterization of Ti-AZT

3.2.1. Analysis of the structure and the composition by TEM and EDX

Figure 2 shows a TEM image of the 3.3 atom% Ti-AZT sample. The structure of Ti-AZT is the same as that of AZT [18]. Al_2O_3 primary particles (amorphous–shape particles) and ZrO_2-TiO_2 primary particles (distinct-shape particles) also coexisted in the same secondary particles. No discrete TiO_2 particles were observed in Ti-AZT. This indicates that Ti is present homogeneously on the AZT surface and may be dissolved in the Al_2O_3 phase as an Al_2O_3-TiO_2 solid solution. TiO_2 is simultaneously dissolved in the ZrO_2-TiO_2 solid solution, because the synthesis method involved the impregnation of AZT with the Ti salt solution.

In order to clarify the Ti concentration on the Al_2O_3 particles, random analysis spots of Al_2O_3 primary particles were examined using EDX. The compositions of three selected spots are listed in Table. 2. The Ti concentration was more than 10 atom% in each analysis spot, although the amount of Ti doped was 3.3 atom%. Therefore, the surface of the Al_2O_3 particle was modified with Ti in a dispersed state, and this surface localization is expected to work effectively for sulfur resistance.

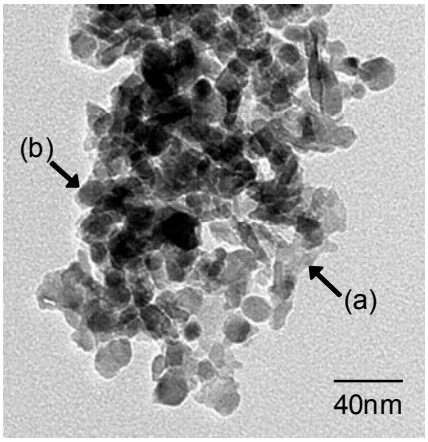

Fig. 2. FE-TEM micrograph of 3.3 atom% Ti-AZT. Arrows (a) and (b) indicate examples of an Al_2O_3 primary particle and a ZrO_2-TiO_2 primary particle, respectively.

3.2.2. Analysis of the structure by XRD

In order to confirm the presence of discrete TiO_2 particles and analyze the crystal structure, XRD patterns of Ti-AZT with different Ti amounts were measured, and are shown in Fig. 3. AZT has the γ-Al_2O_3 phase and tetragonal ZrO_2 phase with a peak shift at the (101) peak due to the formation of the ZrO_2-TiO_2 solid solution [18]. All of the Ti-AZT samples contained the same AZT structure. Although the doped Ti is thought to be present on both ZrO_2-TiO_2 and γ-Al_2O_3, further shift of the (101) diffraction peak for the tetragonal ZrO_2 phase was not observed. This is because the amount of Ti doped in the ZrO_2-TiO_2 is too small to observe further peak shift.

The 1.6 and 3.3 atom% Ti-AZT samples revealed no crystalline TiO_2 phase. This indicates that doped Ti is present on the surface of both the Al_2O_3 particles, as an Al_2O_3-TiO_2 solid solution, and ZrO_2-TiO_2 solid solution particles. On the other hand, 6.2 atom% Ti-AZT revealed a crystalline rutile TiO_2 peak. It has been reported that the formation of an Al_2O_3-TiO_2 solid solution depends on the amount of doped Ti [21,22]. Therefore, the excess amount of Ti in 6.2 atom% Ti-AZT is considered to form isolated rutile TiO_2 particles. TiO_2 particles have weak thermal stability and cause poor catalytic performance after thermal aging, because TiO_2 easily aggregates and reacts with the NO_x storage materials [6]. In this system, it is better to maintain the doped titanium amount at less than 3.3 atom% for the support of a NSR catalyst; therefore, 3.3 atom% Ti-AZT was used as the standard sample in the subsequent experiments.

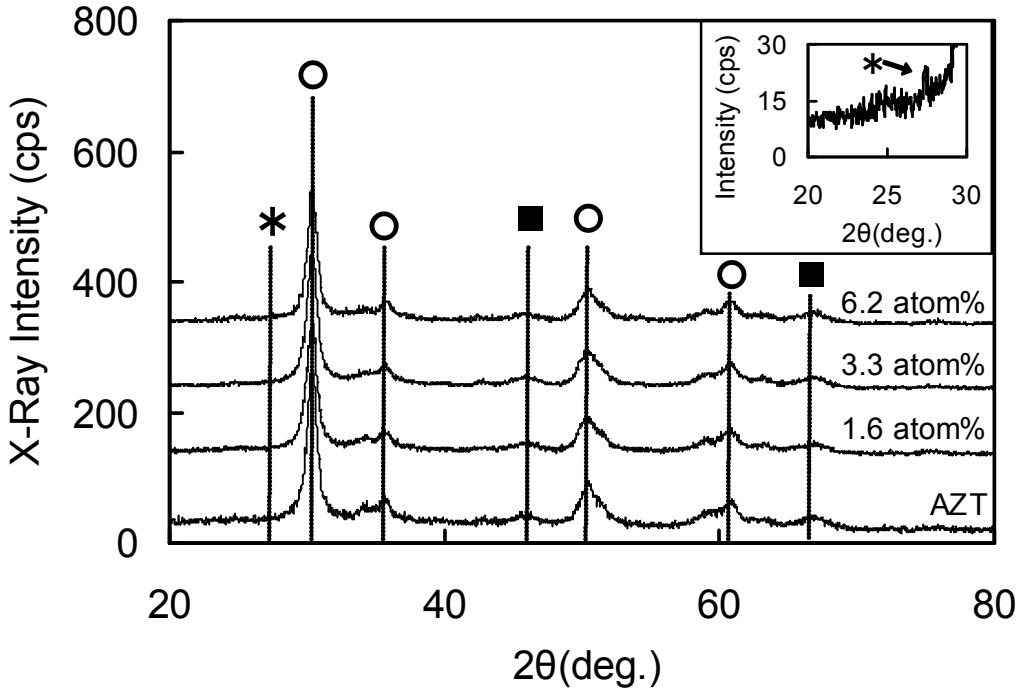

Fig. 3. XRD patterns of Ti-AZT with various amounts of Ti doping. The inset shows an enlarged view of 6.2 atom% Ti-AZT around the rutile-TiO_2 (100) peak. (○) tetragonal ZrO_2, (■) γ-Al_2O_3, (∗) rutile-TiO_2.

3.2.3. Base property

Table 3 shows the amount of base determined by CO_2-TPD. Although the CO_2 desorption of Ti-AZT was found at the same temperature region as that for AZT, the maximum CO_2 concentration of Ti-AZT was small compared with that of AZT. The amount of base in Ti-AZT was reduced by 25% relative to that in AZT, and by more than 80% relative to that of the physically mixed oxide, which has 12.1 μmol/g of base [18]. The amount of base is in good inverse proportion to the amount of Ti on Al_2O_3. Therefore, the basicity of Al_2O_3 is canceled by the acidic TiO_2, and the increased presence of TiO_2 is effective in further lessening the affinity of the catalyst support with acidic gases.

Table 3. Base amount, surface area, and meso-pore volume.

	Base amount (μmol/g)	SSA (m^2/g)	Meso-pore volume (cc/g)
AZT	2.7	128	0.41
Ti-AZT	2.1	112	0.39

3.2.4. Surface area and pore distribution

Table 3 shows the specific surface area (SSA) of Ti-AZT and AZT. Ti-AZT maintained a high SSA, although it was slightly decreased compared with AZT. From the results of TEM and XRD, it was determined that this slight drop in SSA results not from discrete TiO_2 particles, but from the formation of a TiO_2-Al_2O_3 solid solution [21].

Figure 4 shows the pore diameter distribution, and Table 3 lists the mesopore volume of each sample. Ti-AZT had a single sharp mesopore peak around 15 nm (Fig. 4, black line) and almost the same mesopore volume as AZT. These results indicate the morphology of the original AZT structure was maintained after the Ti doping step.

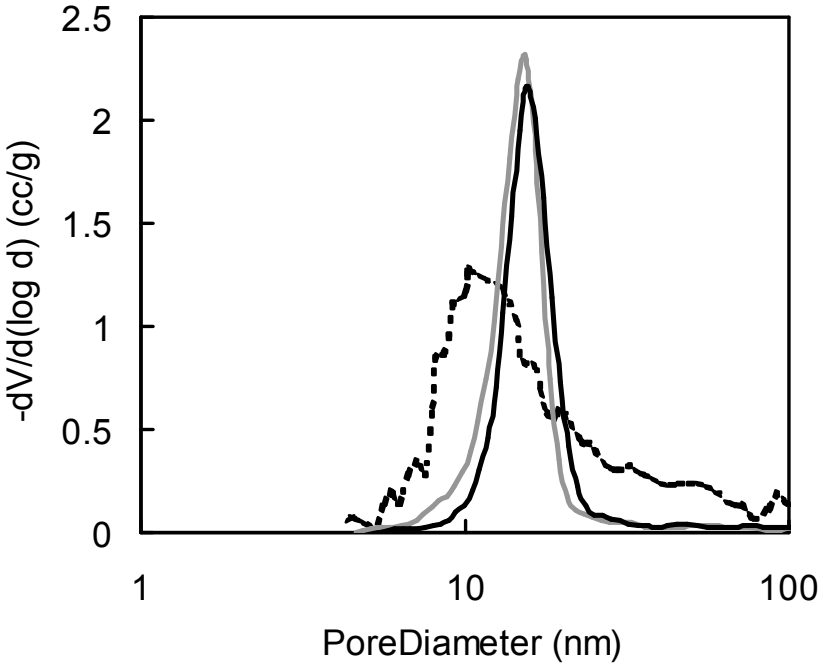

Fig. 4. Pore distribution of samples. Ti-AZT (———); AZT (———); physically mixed Al_2O_3 and ZrO_2-TiO_2 (– – –).

3.2.5. Thermal stability

To confirm the thermal stability of Ti-AZT, the particle size of ZrO_2-TiO_2 after thermal treatment was investigated by XRD, based on the ZrO_2 (101) peak data. Figure 5 shows the average particle size of ZrO_2-TiO_2 at each thermal treatment temperature. The particle size of ZrO_2-TiO_2 in Ti-AZT was almost identical to that in AZT at each temperature. The SSA for each thermal treatment temperature showed that Ti-AZT has the same SSA variation as AZT, as shown in Fig. 6.

As previously shown, the morphology of AZT is maintained through the Ti doping step; therefore, Ti-AZT has the same thermal stability as AZT, and is expected to exhibit high NO_x storage performance with not only sulfur durability, but also thermal stability.

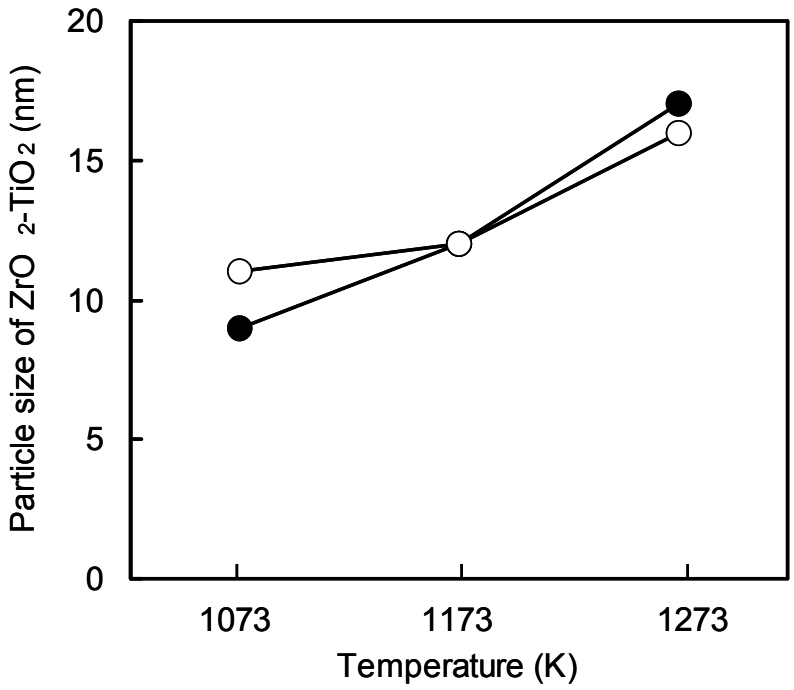

Fig. 5. Average particle size of ZrO_2-TiO_2 determined by XRD data as a function of thermal treatment temperature. (●) Ti-AZT; (○) AZT

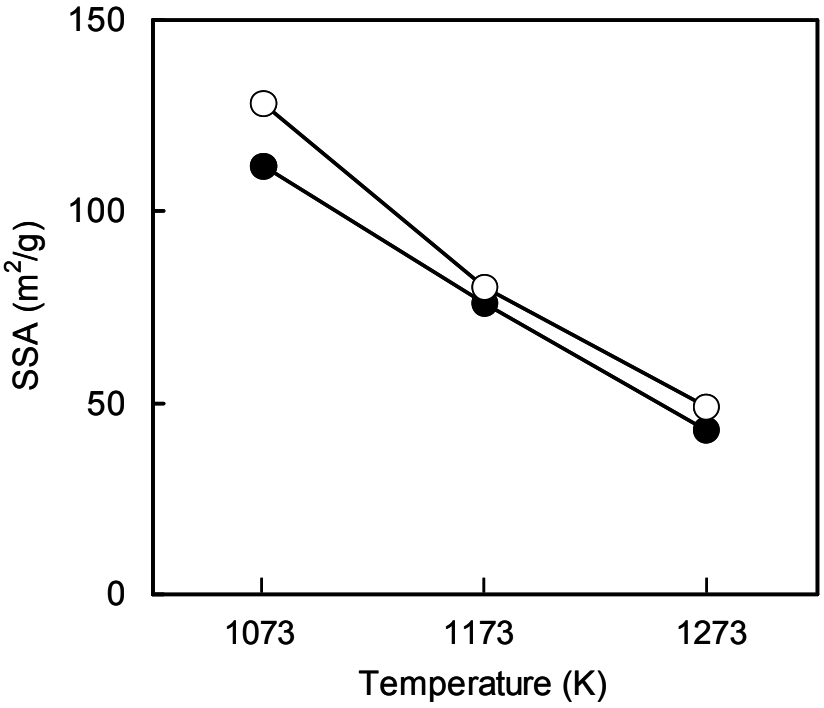

Fig. 6. SSA of samples as a function of thermal treatment temperature. (●) Ti-AZT; (○) AZT

3.3. Catalytic application of Ti-AZT

3.3.1. SO_2-TPD

The inhibition of SO_x adsorption and the promotion of sulfur species desorption are required to improve the sulfur durability of NSR catalysts. Figure 7 shows the SO_2-TPD spectra for the catalysts from 623 to 1023 K. The Ti-AZT catalyst has a larger amount of sulfur desorption at low temperature around 750 K than the AZT catalyst. In addition, the starting temperature of sulfur desorption from the Ti-AZT catalyst is 700 K, which is approximately 20 K lower temperature than that for the AZT catalyst. Sulfur species desorb from γ-Al_2O_3 surfaces at less than 873 K [7]; therefore, it was determined that the Ti-AZT catalyst facilitates sulfur desorption from the support. In addition, the starting temperature of sulfur desorption from Ti-AZT is decreased, in accordance with the Ti doping concept.

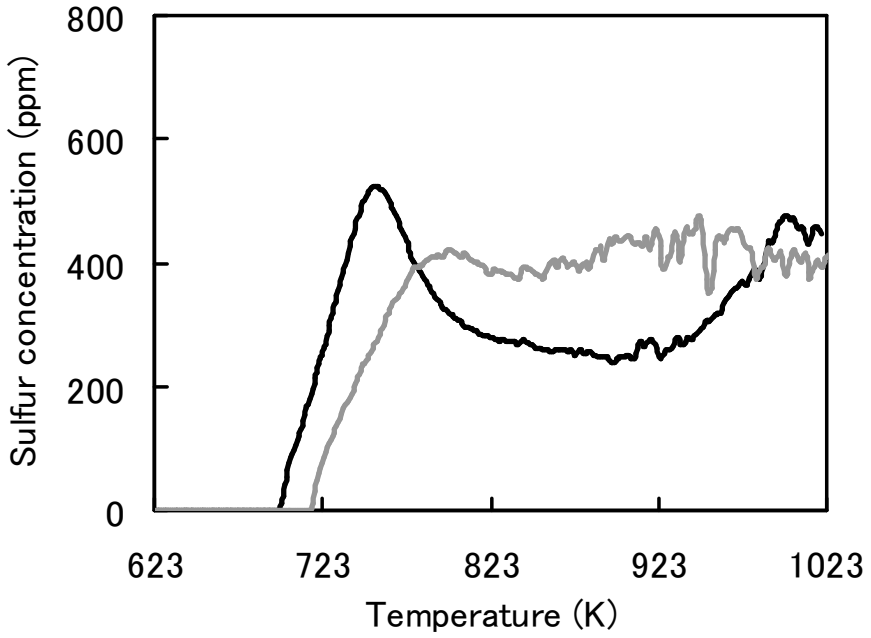

Fig. 7. Sulfur desorption spectra of samples. Ti-AZT catalyst (——), AZT catalyst (——).

Furthermore, the sulfur concentration of the Ti-AZT catalyst was low from 823 to 980 K, although both catalysts had the same sulfur concentration at around 1000 K. It has been understood that desorbed sulfur species are derived from the decomposition of barium sulfate at more than 873 K in the Pt/Ba/γ-Al_2O_3 system [7]. Therefore, there is a possibility that the amount of sulfate materials in the Ti-AZT catalyst is smaller than that in the AZT catalyst. To confirm this, the amount of residual sulfur deposit was examined following the SO_2 aging test at 873 K. As a result, the SO_2 aged Ti-AZT catalyst had 2.5 wt% of residual sulfur deposit, and the AZT catalyst had 2.8 wt%. This indicates that the amount of sulfur derived from sulfur poisoned NO_x storage materials is small in the Ti-AZT catalyst. Therefore, a close relationship between the following two kinds of sulfur poisoning is suggested: sulfur coverage resulting in SO_x adsorption on catalysts and sulfate formation of NO_x storage materials. The inhibition of SO_x adsorption may introduce the inhibition of sulfate formation of neighboring NO_x storage materials, considering that the main improvement in this novel support is the lowered basicity. Clarification of the detailed relationship should be carried out in the future; however, this attribute is expected to lead to NSR catalysts with higher performance for NOx storage.

3.3.2. NO_x storage performance

To verify the effect of the Ti-AZT catalyst on sulfur durability as a NSR catalyst, the NO_x storage of the catalysts was measured after the sulfur aging test. These catalysts were pretreated at 873 K under a rich gas condition before the NOx storage measurements.

Figure 8 shows the amount of NO_x storage at each temperature. The Ti-AZT catalyst has a larger amount of NO_x storage than the AZT catalyst. This difference results from the reduction in not only the affinity of the catalyst surface with SO_2, but also in the

amount of sulfur poisoned NO_x storage materials, as mentioned in section 3.3.1. The active Ba and K NO_x storage species are assumed to form nitrate species such as $Ba(NO_3)_2$ and KNO_3 under lean conditions, as reported in the literature [5,24,25].

NSR catalysts continuously suffer from SO_x poisoning, as well as thermal deterioration, in the presence of actual exhaust gases from lean-burn engines. Ti-AZT has acquired sulfur durability in addition to the thermally stability characteristics of the original AZT support. Therefore, Ti-AZT is an ideal material for practical use as a NSR catalyst support.

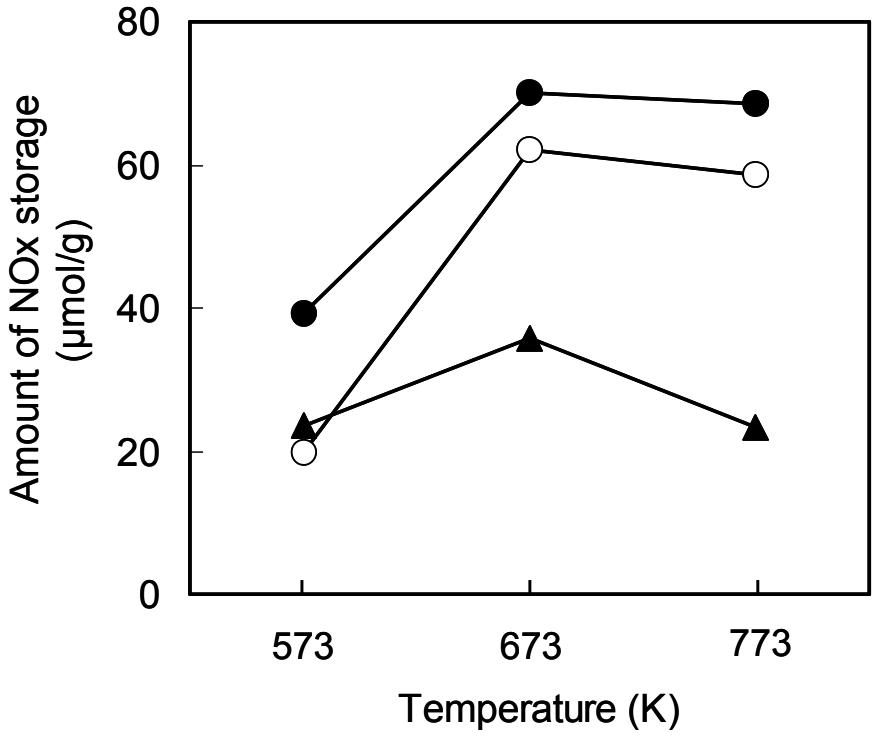

Fig. 8. NOx storage performance after sulfur aging tests as a function of the reaction temperature. (●) Ti-AZT catalyst; (○) AZT catalyst; (▲) physically mixed catalyst.

4. Conclusion

Ti-AZT was synthesized as a support for NSR catalyst based on AZT. All Al_2O_3 primary particles in Ti-AZT had higher Ti concentrations than those in AZT. Ti-AZT maintains the original AZT structure with thermal stability after Ti doping, and provides a support with low basicity.

From the SO_2-TPD results, the Ti-AZT catalyst promotes significant sulfur desorption relative to the AZT catalyst. After sulfur aging tests, the Ti-AZT catalyst had a larger amount of NO_x storage than the AZT catalyst.

The improved sulfur durability of this NSR catalyst has resulted from the doping of Ti as an Al_2O_3-TiO_2 solid solution in AZT. Therefore, Ti-AZT has acquired sulfur durability and maintained the thermal stability of the original AZT support, thereby meeting the requirements for NSR catalysts.

References

[1] S. Sato, Y. Yu-u, H. Yahiro, N. Mizuno, M. Iwamoto, *Appl. Catal.* 70 (1991) L1.

[2] Y. Kintaichi, H. Hamada, M. Tabata, M. Sasaki, T. Ito, *Catal. Lett.* 6 (1990) 239.

[3] R. Burch, P. J. Millington, *Catal. Today* 26 (1995) 185.

[4] W. Bögner, M. Krämer, B. Krutzsch, S. Pischinger, D. Voigtländer, G. Wenninger, F. Wirbeleit, M. S. Brogan, R. J. Brisley, D.E. Webster, *Appl. Catal. B: Environ.* 7 (1995) 153.

[5] N. Takahashi, H. Shinjoh, T. Iijima, T. Suzuki, K. Yamazaki, K. Yokota, H. Suzuki, N. Miyoshi, S. Matsumoto, T. Tanizawa, T. Tanaka, S. Tateishi, K. Kasahara, *Catal. Today* 27 (1996) 63.

[6] N. Takahashi, A. Suda, I. Hachisuka, M. Sugiura, H. Sobukawa, H. Shinjoh, *Appl. Catal. B: Environ.* 72 (2006) 187.

[7] S. Matsumoto, Y. Ikeda, H. Suzuki, M. Ogai, N. Miyoshi, *Appl. Catal. B: Environ.* 25 (2000) 115.

[8] E. C. Corbos, X. Courtoins, N. Bion, P. Marecot, D. Duprez, *Appl. Catal. B: Environ.* 80 (2008) 62.

[9] X. Wei, X. Liu, M. Deeba, *Appl. Catal. B: Environ.* 58 (2005) 41.

[10] J. Dawody, M. Skoglundh, L. Olsson, E. Fridel, *Appl. Catal. B: Environ.* 70 (2007) 179.

[11] Z. Liu, J. Anderson, *J. Catal.* 228 (2004) 243.

[12] K. Yamamoto, R. Kikuchi, T. Takeguchi, K. Eguchi, *J. Catal.* 238 (2006) 449.

[13] T. Kanazawa, *Catal. Today* 96 (2004) 171.

[14] K. Ito, S. Kakino, K. Ikeue, M. Machida, *Appl. Catal. B: Environ.* 74 (2007) 137.

[15] K. M. Adams, G. W. Graham, *Appl. Catal. B: Environ.* 80 (2008) 343.

[16] M. Casapu, J. Grunwaldt, M. Maciejewski, M. Wittrock, U. Göbel, A. Baiker, *Appl.*

Catal. B: Environ. 63 (2006) 232.

[17] N. Takahashi, S. Matsunaga, T. Tanaka, H. Sobukawa, H. Shinjoh, *Appl. Catal. B: Environ.* 77 (2007) 73.

[18] H. Imagawa, T. Tanaka, N. Takahashi, S. Matsunaga, A. Suda, H. Shinjoh, *J. Catal.* 251 (2007) 315.

[19] M. Milanova, M. Arnaudov, M. Getsova, D. Todorovsky, *J. Alloys Comp.* 264 (1998) 95

[20] Y. Xie, C. Yuan, *Appl. Catal. B: Environ.* 46 (2003) 251.

[21] W. Zhaobin, X. Qin, G. Xiexian, *Appl. Catal*. 63 (1990) 305.

[22] L. O. Öhman, J. Paul, *Mater. Chem. Phys.* 73 (2002) 242.

[23] H. Y. Huang, R. Q. Long, R. T. Yang, *Appl. Catal. B: Environ.* 33 (2001) 127.

[24] M. Takeuchi, S. Matsumoto, *Top. Catal.* 28 (2004) 151.

[25] N. Takahashi, K. Yamazaki, H. Sobukawa, H. Shinjoh, *J. Chem. Eng. Jpn.* 39 (2006) 437.

Part II

CeO_2 nanostructure formation for O_2 storage and release

Chapter 5

Synthesis of monodisperse CeO_2 nanoparticles and their application to O_2 storage and release

Abstract

Monodisperse polyhedral nanoparticles (NPs) of cerium dioxide, CeO_2, were synthesized by thermal decomposition of ammonium cerium(IV) nitrate, $(NH_4)_2Ce(NO_3)_6$, at 180ºC in an organic solution of oleylamine (OAm) and/or oleic acid (OA). The 4 nm CeO_2 NPs were synthesized in diphenyl ether solution of OAm and OA with the molar ratio of Ce/OAm/OA = 1/3/3, while the 6 nm CeO_2 NPs were made in 1-octadecene solution of OAm with Ce/OAm = 1/6. The CeO_2 NPs were assembled on γ-Al_2O_3 via polyvinylpyrrolidone and were annealed at 500 ºC under air to remove organic coating. They were well dispersed on Al_2O_3 and showed the increased oxygen storage capacity compared to the physical mixture of aggregated CeO_2 and γ-Al_2O_3 powder. The reported CeO_2 NPs are promising for oxygen storage/release applications.

1. Introduction

Nanoscale cerium (IV) dioxide (CeO_2), commonly known as ceria, is an important material for solid oxide fuel cell and for catalytic applications due to their enhanced capability in absorbing and releasing oxygen via the Ce^{4+}/Ce^{3+} redox cycle [1-5]. For example, the oxygen storage/release properties of the nanostructured ceria are often applied to the three way catalyst in the automobile exhaust system where oxygen concentration needs to be constant around the catalyst so that the catalytic performance of noble metal catalysts can be maximized [3-5]. Catalysts based on ceria are also promising for low temperature CO oxidation [6], soot oxidation [7], and water gas shift reactions [8]. One key requirement during catalytic optimization of these ceria-based catalysts is the control of nanoscale sizes and morphologies of ceria. Despite recent advances in the syntheses of nanostructured ceria with sub-10 nm sizes via hydrothermal [9-13], microemulsion [14,15], and organic phase methods [16-19] it is still challenging to stabilize these ceria in aqueous dispersions [9-15], or to disperse them on solid supporting materials[16-19]. Therefore, the chemical properties, especially oxygen storage/release capacity (OSC) and low temperature oxidation catalysis, of the dispersed nano-ceria have rarely been studied.

Here the author reports a facile synthesis and assembly of monodisperse 4 nm and 6 nm CeO_2 nanoparticles (NPs) and study their OSC. The NPs are made by thermal decomposition of ammonium cerium(IV) nitrate, $(NH_4)_2Ce(NO_3)_6$ in diphenyl ether or 1-octadecene in the presence of oleylamine (OAm) and/or oleic acid (OA). Depending on the surfactants used in the reaction, polyhedral NPs of CeO_2 can be obtained. The as-synthesized CeO_2 NPs are deposited on the γ-Al_2O_3 support via poly(vinylpyrrolidone) (PVP)-mediated assembly and the organics around NPs are

removed by oxidative thermal annealing in air. The author demonstrates that once deposited on γ-Al_2O_3, the CeO_2 NPs stay well-dispersed and show much enhanced OSC than the aggregated CeO_2 NPs. The results shown in this chapter is consistent with what have been observed that CeO_2 supported on Al_2O_3 often show high catalytic activities [20,21], and offer a promising approach to nanoscale CeO_2 for advanced catalytic applications.

2. Experimental

All chemicals used in the synthesis were purchased from Sigma-Aldrich and were in regular grade of purity.

2.1. Synthesis of 4 nm CeO_2 NPs

Ammonium cerium(IV) nitrate ($(NH_4)_2Ce(NO_3)_6$) (0.5 mmol), diphenyl ether (10 mL), OA (1.5 mmol), and OAm (1.5 mmol) were mixed under N_2 with magnetic stirring. The mixture was then heated to 180 ºC and kept at this temperature for 2 h. After the reaction solution was cooled down to room temperature, ethanol (30 mL) was added and the NP product was separated by centrifugation at 8000 rpm for 8 min. After washing with ethanol one time, the NP precipitate was redispersed in 10 mL of hexane for further use.

2.2. Synthesis of 6 nm CeO_2 NPs

$(NH_4)_2Ce(NO_3)_6$ (0.5 mmol), 1-octadecene (90 %, 10 mL), and OAm (3 mmol) were mixed under N_2 with magnetic stirring. The reaction conditions and the following work-up procedures were the same as those reported in the synthesis of 4 nm CeO_2 NPs.

2.3. Characterization of CeO_2 NPs

CeO_2 NP morphology and structure were characterized by transmission electron microscopy (TEM). TEM samples were prepared by depositing one drop of diluted NP dispersion in hexane on amorphous carbon coated copper grids. TEM images were acquired with a Philips EM 420 (120 kV) or a JEOL 2010 TEM (200 kV). Statistical size of the NPs was calculated based on randomly selected 35 NPs in high resolution TEM (HRTEM) images, and shown as a combination of the mean value and the standard deviation.

The average size and crystal structure of an assembly of NPs was characterized by x-ray diffraction (XRD) using a Bruker AXS D8 with Cu-Kα radiation (λ=1.5418 Å). The average diameter of CeO_2 NPs was estimated using Scherrer's formula based on the (111) peak of the fluorite cubic CeO_2 structure at $2\theta = 28.5^{o}$.

2.4. CeO_2 NP Deposition on γ-Al_2O_3

The surface of γ-Al_2O_3 (Sigma-Aldrich, 135 m^2/g) was first coated by PVP (MW = 10,000, Sigma-Aldrich) by immersing the Al_2O_3 powder (1 g) into 10 wt% PVP solution in ethanol (6 mL) for 30 min [22]. Then, the powder was washed with ethanol, and dried at 110 ºC. The PVP-Al_2O_3 powder was then immersed into the hexane dispersion of CeO_2 NPs (0.066 mmol/mL for 1.5 mL) and the mixture was stirred at room temperature for 2 h. The solvent was evaporated and the solid powder was further baked at 110 ºC for 2 h and annealed at 500 ºC for 30 min under air to remove the surfactants and PVP. The sample prepared from 4 nm CeO_2 NPs is referred as 4 nm CeO_2 NPs/Al_2O_3, and that prepared from 6 nm CeO_2 NPs as 6 nm CeO_2 NPs/Al_2O_3 throughout evaluations. The composition of CeO_2: γ-Al_2O_3 was measured by inductively coupled

plasma atomic emission spectroscopy (ICP-AES, Rigaku, CIROS 120EOP) to be 15: 85 by weight. Pt loaded samples were prepared by the impregnation of CeO_2 NPs/Al_2O_3 powder in water solution of chloroplatinic acid hexahydrate (Stream Chemical, 1.07 μmol/mL for 10 mL) for 2 h, and then calcined at 500 ºC for 3 h. The total Pt loaded onto the CeO_2 NPs/Al_2O_3 was measured by ICP-AES to be 4 wt%.

2.5. Preparation of physical mixture of CeO_2 and γ-Al_2O_3

The physical mixture of the γ-Al_2O_3 powder and the aggregated CeO_2 NPs (~8 nm) obtained by evaporating the 4 nm CeO_2 NP dispersion solution on a ceramic plate and annealing at 500 ºC for 30 min under air was used as a reference sample. Pt loaded samples were prepared in the same manner as that of the CeO_2 NPs deposited samples. The composition of the reference samples was the same as that of the CeO_2 NPs/Al_2O_3 samples.

2.6. Characterization of CeO_2 NPs/Al_2O_3 samples and their OSC measurement.

The average diameter of CeO_2 primary particles was estimated using Scherrer's formula based on the (111) peak of the fluorite cubic CeO_2 structure at $2\theta = 28.5^{o}$ in XRD patterns. All samples were aged at 700 and 1000 ºC for 3 h under air atmosphere in order to survey the change of CeO_2 NP size by heating. BET surface area of the CeO_2 NPs/Al_2O_3 samples was measured by N_2 adsorption at 77 K using an automatic surface analyzer, Micro Data MicroSorp 4232 II. The surface area of the 4 nm CeO_2 NPs/Al_2O_3 was 134 m^2/g, and that of the 6 nm CeO_2 NPs/Al_2O_3 was 137 m^2/g. The surface area of the reference sample was 137 m^2/g.

OSC of CeO_2 NPs/Al_2O_3 was measured using thermogravimetry, Shimadzu TGA-50. The outline of OSC measurement is shown in Fig. 1. The sample (15 mg) was

pretreated at 500 °C for 15 min under O_2 (29 %)/N_2 (balance), and then, exposed to H_2 (17 %)/N_2 (balance) until the weight decrease was not observed [23]. Then, O_2/N_2 gas was introduced again. The gas flow rate was 50 cc/min. This cycle was repeated twice to confirm the reproducibility, and OSC, reflecting the total amount of O_2 released from CeO_2 at 500 ºC, was calculated based on the average amount of weight increase and decrease in each step. The OSC's were further measured from the samples aged at 700 ºC for 3 h in air and compared with those obtained from the as-prepared samples. OSC's of the Pt/CeO_2 NPs/Al_2O_3 samples were normalized by the deduction of the OSC of Pt/Al_2O_3 from totally observed OSC in order to remove the contribution of the OSC from Pt/Al_2O_3. The commercial CeO_2 powder (Anan Kasei Co., Ltd., 99.9 %, 120 m^2/g) was also used as a control during the OSC measurement.

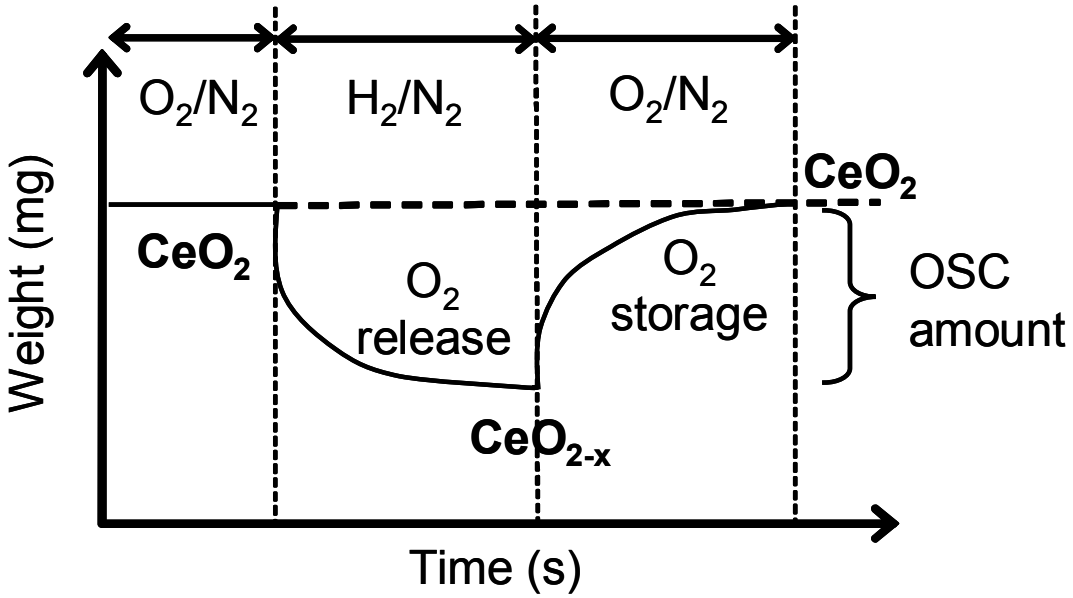

Fig. 1. Measurement of OSC. Original weight (▬ ▬ ▬), Weight change during measurement (———).

3. Results and discussion

3.1. Synthesis and characterization of CeO_2 NPs

The monodisperse CeO_2 NPs were synthesized by thermal decomposition of $(NH_4)_2Ce(NO_3)_6$. The 4 nm CeO_2 NPs were made by mixing $(NH_4)_2Ce(NO_3)_6$, OAm and OA in diphenyl ether, and heating the reaction mixture at 180 ºC for 2 h. In this synthesis, OAm and OA were added as surfactants and the molar ratio of Ce/OAm/OA was controlled to be 1/3/3. Under this synthetic condition, the binding between OA and Ce-ion might facilitate CeO_2 nucleation in diphenyl ether, leading to the formation of smaller CeO_2 NPs [24,25]. The 6 nm CeO_2 NPs were prepared by mixing $(NH_4)_2Ce(NO_3)_6$ and OAm in 1-octadecene, and heating the reaction mixture at 180 ºC for 2 h. Although only OAm was added as a surfactant in this synthesis, the author found that the total amount of surfactant should be kept the same as that in the 4 nm CeO_2 NP synthesis (the molar ratio of Ce/OAm in 1/6) in order to obtain CeO_2 NPs with narrow size distribution. Due to the weak binding of amine to Ce^{4+}, CeO_2 nucleation in 1-octadecene might not reach its threshold as early as that in diphenyl ether, giving larger 6 nm CeO_2 NPs. Figure 2A and 2B show the TEM images of the 4 nm and 6 nm CeO_2 NPs obtained as the final product from the two syntheses. Measuring 35 NPs in each group gives statistical sizes at 4.17 nm ± 0.23 nm and 5.78 nm ± 0.56 nm. HRTEM images (Fig. 2C and 2D) reveal that both NPs are in single crystalline structure with interplanar fringes of 0.32 nm and 0.27 nm representing {111} and {200} lattices in fluorite cubic CeO_2 crystal structure.

In the synthetic condition reported here, the quality of the CeO_2 NPs was dependent on the amount of OAm present in the reaction mixture. Smaller amount of OAm resulted in CeO_2 NPs with irregular shapes and broad size distribution, as seen from

the TEM image of the 6 nm CeO_2 NPs (Fig. 2E). TEM analysis further indicated that the 6 nm CeO_2 NPs started to form at reaction temperature around 150 ºC (Fig. 2F) and then developed into more uniformed size and shape during the heating at 180 ºC. The same tendency was observed in the synthesis of 4 nm CeO_2 NPs.

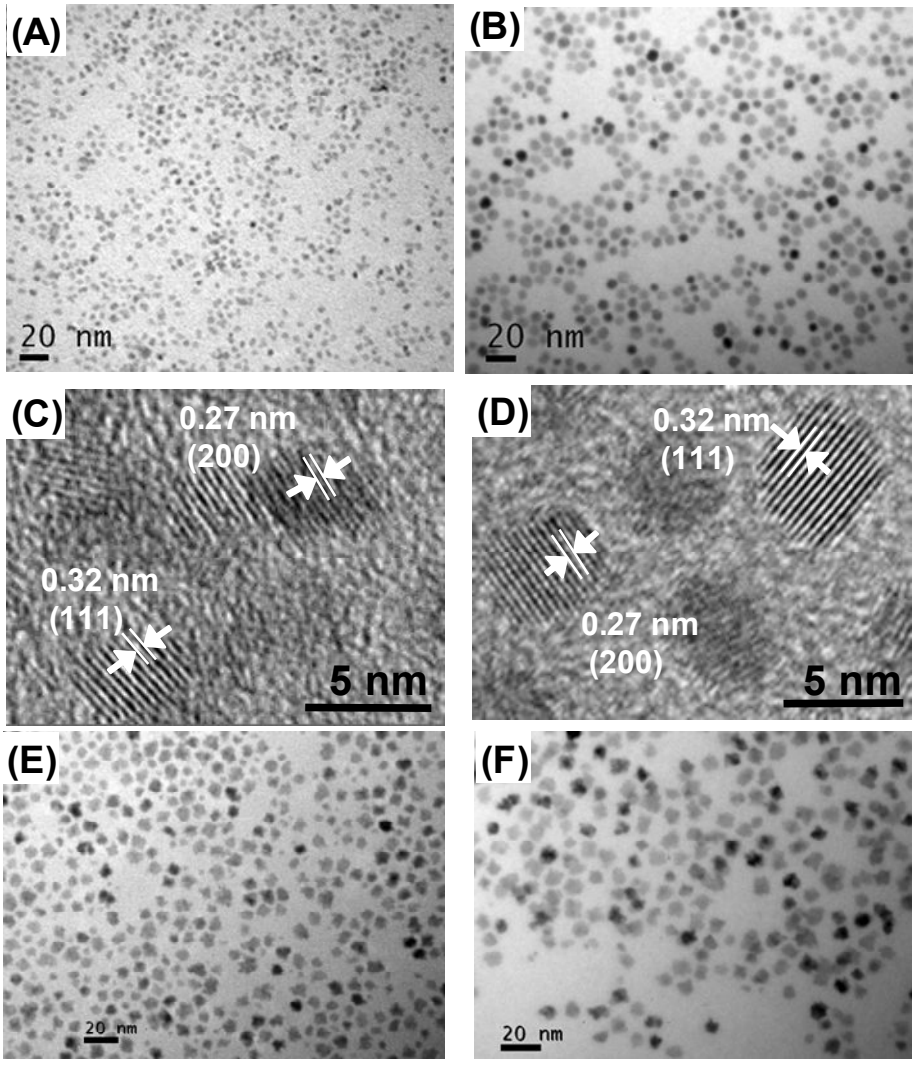

Fig. 2. TEM images of (A) the 4 nm CeO_2 NPs and (B) the 6 nm CeO_2 NPs; HRTEM images of (C) the 4 nm CeO_2 NPs and (D) the 6 nm CeO_2 NPs; TEM images of CeO_2 NPs synthesized in 1-octadecene with the molar ratio of (E) Ce/OAm = 1/1.5 at 180 ºC and (F) Ce/OAm = 1/6 at 150 ºC.

XRD patterns of both 4 nm and 6 nm CeO_2 NP assemblies show the typical cubic fluorite (CaF_2) structure (Fig. 3A and B). Using Scherrer's formula based on the (111) peak at $2\theta = 28.5^{\circ}$, the estimated average diameters of these two kinds CeO_2 NPs were 3.7 nm and 5.1 nm respectively. These are close to the sizes of 4 nm and 6 nm measured by TEM, indicating that both kinds of NPs are in good crystallinity.

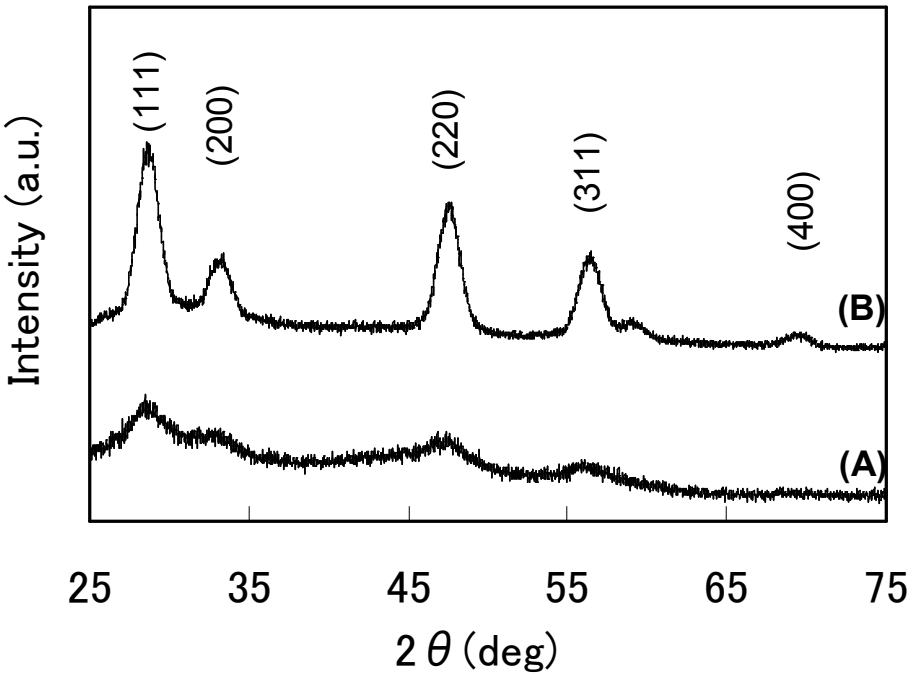

Fig. 3. XRD patterns of (A) the 4 nm CeO_2 NPs, (B) the 6 nm CeO_2 NPs.

3.2. Preparation of dispersed CeO_2 NPs on Al_2O_3.

Previous studies on the Ce^{4+}/Ce^{3+} redox cycle of CeO_2 NPs have indicated that well-dispersed CeO_2 NPs with smaller size should show the enhanced OSC [26,27]. To study OSC of the monodisperse CeO_2 NPs prepared in this work, these NPs were

annealed to remove the surfactant and to activate them for oxygen storage and release. The unannealed NPs show negligible OSC due to the presence of surfactants around the NP surface. To prevent NPs from aggregation/sintering during this high temperature annealing treatment, γ-Al_2O_3 as the CeO_2 NP support were selected. To ensure that the hydrophobic CeO_2 NPs could be deposited on the hydrophilic γ-Al_2O_3 surface, the author first immersed the γ-Al_2O_3 into the ethanol solution of PVP to have PVP absorbed on the Al_2O_3 according to the literature [22]. The subsequent washing with ethanol removed the extra PVP attached to the γ-Al_2O_3, giving PVP-Al_2O_3. Upon mixing the hexane dispersion of CeO_2 and PVP-Al_2O_3 followed by hexane wash, CeO_2 NPs on the PVP-Al_2O_3 surface was obtained. Annealing at 500 ºC under air for 30 min removed organic species around NPs, giving a CeO_2 NPs/Al_2O_3 sample with 15 wt % CeO_2 NPs supported on γ-Al_2O_3.

Figure 4A and 4B show the TEM images of the 4 nm CeO_2 NPs and 6 nm CeO_2 NPs deposited on γ-Al_2O_3 after 500 ºC annealing. CeO_2 NPs are well dispersed on γ-Al_2O_3 surface without noticeable aggregation/sintering. This is further confirmed by XRD of the annealed CeO_2 NPs/Al_2O_3 in Fig. 5A(1) and 5B(1), where the diffraction patterns stay the same as those shown in Fig. 3 and the CeO_2 NPs are better stabilized by the γ-Al_2O_3 support under the annealing condition. As a comparison, CeO_2 NPs without this γ-Al_2O_3 stabilization grew into ~8 nm after annealing (Fig. 5A(2) and 5B(2)). The stabilization effect of CeO_2 NPs by γ-Al_2O_3 was confirmed by higher temperature annealing at 700 and 1000 ºC after which the average size of the CeO_2 NPs stayed under 20 nm while the NPs in the physical mixture with γ-Al_2O_3 grew into 50 nm (Table 1).

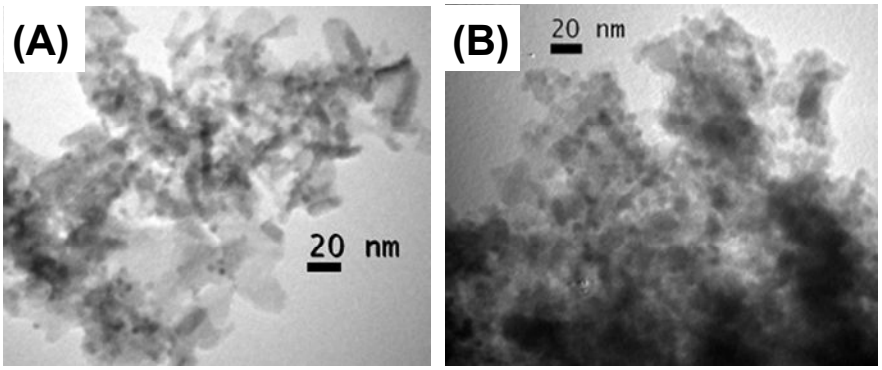

Fig. 4. TEM images of (A) the 4 nm CeO_2 NPs/Al_2O_3 and (B) the 6 nm CeO_2 NPs/Al_2O_3 after annealing at 500 ºC.

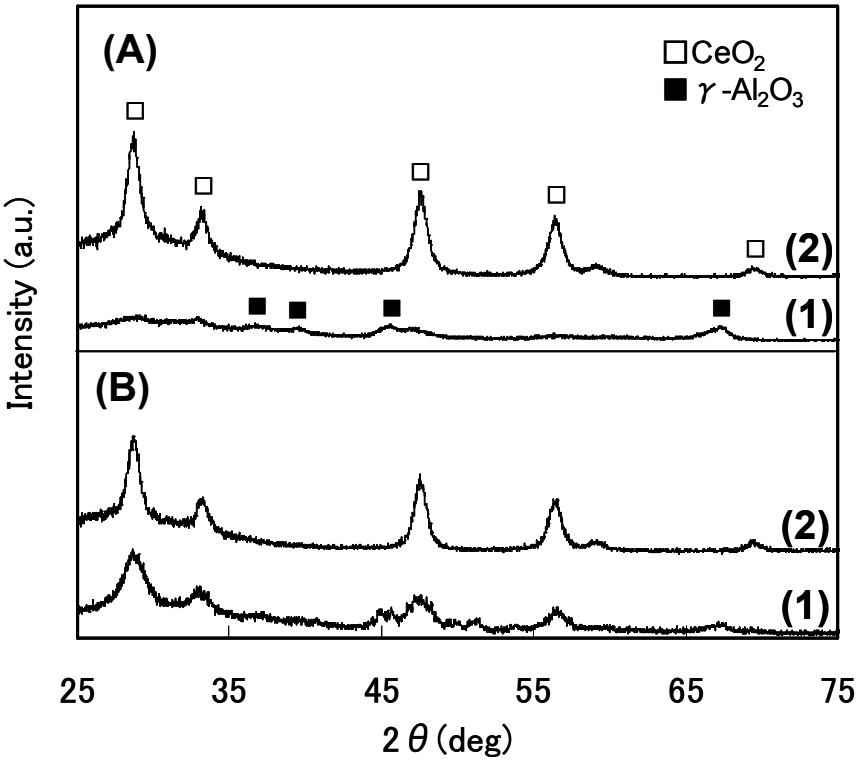

Fig. 5. XRD patterns of the annealed (A) 4 nm CeO_2 NPs with (1) and without (2) the Al_2O_3 support, and (B) 6 nm CeO_2 NPs with (1) and without (2) the Al_2O_3 support.

Table 1. CeO_2 particle size, and OSC of CeO_2 NPs/Al_2O_3 and Pt/CeO_2 NPs/Al_2O_3.

Samples	CeO_2 particle size (nm)			OSC (μ mol-O_2/g sample)		
	500 °C	700 °C	1000 °C	As prepared	After aging	Pt loaded
4nm CeO_2 NPs/Al_2O_3	3.9	5.8	16.0	65.2	29.2	120.8
6nm CeO_2 NPs/Al_2O_3	5.3	6.7	17.7	43.8	20.2	101.6
Physical mixture of CeO_2/Al_2O_3	8.0	22.4	50.9	10.0	trace	30.3
Pure CeO_2*	12.2	15.8	43.5	32.3	4.2	-

* Commercial CeO_2 without Al_2O_3

3.3. Oxygen storage and release properties of CeO_2 NPs

OSC of the 4 nm and 6 nm CeO_2 NPs/Al_2O_3 was measured at 500 ºC, which reflects the total available OSC in order to assess the potential activity for catalytic reaction. Physical mixture of the aggregated 8 nm CeO_2 NPs and γ-Al_2O_3 was used as a reference sample. All samples were exposed to O_2/N_2 and H_2/N_2 alternately every 10 min for oxygen storage (O_2 association with CeO_2) and release (O^{2-} dissociation from CeO_2) tests [23,28-30]. The weight changes of these samples during the tests are normalized and given in Fig. 6. Figure 6A shows the oxygen absorption data under O_2/N_2 and Fig. 6B is the oxygen release data under H_2/N_2. These profiles and OSC shown in Table 1 reveal that the CeO_2 NP-Al_2O_3 sample absorbs and releases more oxygen than the reference sample. Moreover, the smaller CeO_2 NPs (4 nm) have larger OSC than the 6 nm CeO_2 NPs. The OSC of the CeO_2 NPs annealed at 700 ºC was also investigated. Although the OSC was decreased in all samples due to the increase of the CeO_2 NP size, the smaller

CeO_2 NPs still show larger OSC (Table 1). This is attributed to the larger surface area exposed by the smaller NPs and further indicates that oxygen molecules involved in the oxygen storage/release process locate mainly on the CeO_2 NP surface [27,31]. The result obtained is consistent with what have been reported that CeO_2 particles can be stabilized more efficiently on Al_2O_3 and show the increased OSC [32,33]. It is worth to note that CeO_2 particles can interact with Al_2O_3 at high temperature under reducing atmosphere, forming $CeAlO_3$ that deactivates their O_2 storage/release property. This $CeAlO_3$ formation occurs at 600-800 ºC for CeO_2 particles smaller than 18 nm [34,35]. Under the current 500 ºC annealing condition, the formation of $CeAlO_3$ was not detected.

The association of O_2 and dissociation of O^{2-} on CeO_2 can be further enhanced by Pt [28,36], and as a result, Pt loaded on CeO_2 is often catalytically more active [5]. The Pt loaded CeO_2 NPs/Al_2O_3 samples were prepared by impregnation of the CeO_2 NPs/Al_2O_3 powder in water solution of chloroplatinic acid hexahydrate followed by calcinations at 500 ^oC for 3 h. The OSC of the Pt/CeO_2 NPs/Al_2O_3 samples was evaluated in the same way as in CeO_2 NPs/Al_2O_3 and was given in Fig. 6 and Table 1. From the OSC data, Pt does promote O_2 absorption and O^{2-} dissociation for all samples and the trend in the OSC change is similar to what is observed from the non-Pt CeO_2 NPs/Al_2O_3 with small CeO_2 NPs showing larger OSC. The data prove that the CeO_2 NPs prepared in this work have great potential as an efficient OSC material for catalytic applications.

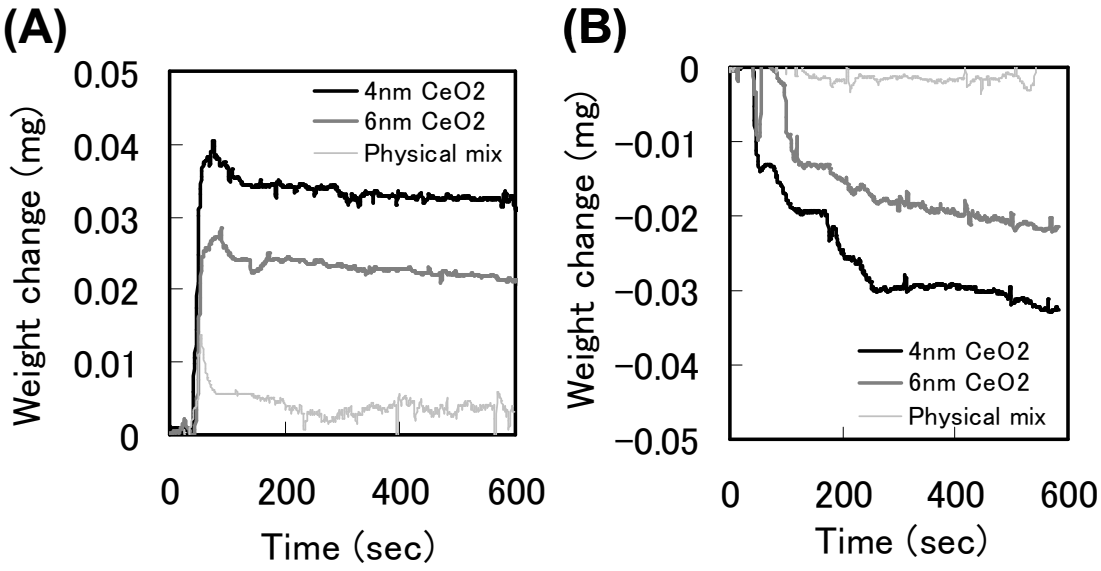

Fig. 6. OSC profile of the 500 ºC annealed CeO_2 NPs/Al_2O_3 samples (A) under O_2/N_2 atmosphere and (B) under H_2/N_2 atmosphere measured at 500 ºC.

4. Conclusions

A facile synthesis of monodisperse CeO_2 NPs by thermal decomposition of $(NH_4)_2Ce(NO_3)_6$ at 180 ºC in an organic solution of oleylamine and/or oleic acid was carried out successfully. The sizes and shapes of the CeO_2 NPs are controlled by reaction solvents and the molar ratio of Ce-precursor and surfactants present in the reaction mixture. The CeO_2 NPs are assembled on γ-Al_2O_3 via PVP and are annealed at 500 ºC under air to remove organic coating. The annealed CeO_2 NPs/Al_2O_3 are active for oxygen storage/release and small NPs show high OSC. The work demonstrates that the CeO_2 NPs made in the sub-10 nm from organic phase synthesis can be activated and are promising OSC materials for advanced catalytic applications.

ACKNOWLEDGEMENT. The author thanks Mr. Anthony McCormick of Brown University for the assistance of HR-TEM analysis, and Mr. Satoru Kosaka of Toyota Central R&D Labs for ICP analysis.

References

[1] X. Zhang, K. J. Klabunde, *Inorg. Chem.* 31 （1992) 1706-1709.

[2] A. Trovarelli, *Catal. Rev.-Sci. Eng.* 38 (1996) 439-520.

[3] H. C. Yao, Y. F. Yao Y. *J. Catal.* 86 (1984) 254-265.

[4] M. Haneda, T. Mizushima, N. Kakuta, A. Ueno, Y. Sato, S. Matsuura, K. Kasahara, M. Sato, *Bull. Chem. Soc. Jpn.* 66 (1993) 1279-1288.

[5] J. Kaspar, P. Fornasiero, M. Graziani, *Catal. Today* 50 (1999) 285-298.

[6] P. Singh, M. S. Hegde, *Chem. Mater.* 21 (2009) 3337–3345.

[7] L. Katta, P. Sudarsanam, G. Thrimurthulu, B. M. Reddy, *Appl. Catal. B: Environ.* 101 (2010) 101-108.

[8] D. Tibiletti, A. A. Fonseca, R. Burch, Y. Chen, J. M. Fisher, A. Goguet, C. Hardacre, P. Hu, D. Thompsett, *J. Phys. Chem. B* 109 (2005) 22553-22559.

[9] M. Hirano, Y. Fukuda, H. Iwata, Y. Hotta, M. Inagaki, *J. Am. Ceram. Soc.* 83 (2000) 1287-1289.

[10] H. X. Mai, L. D. Sun, Y. W. Zhang, R. Si, W. Feng, H. P. Zhang, H. C. Liu, C. H. Yan, *J. Phys. Chem. B* 109 (2005) 24380-24385.

[11] A. Sehgal, Y. Lalatonne, J.-F. Berret, M. Morvan, *Langmuir* 21 (2005) 9359-9364.

[12] S. Yang, L. Gao, *J. Am. Chem. Soc.* 128 (2006) 9330-9331.

[13] F. Zhang, S. W. Chan, J. E. Spanier, E. Apak, Q. Jin. R. D. Robinson, I. P. Herman, *Appl. Phys. Lett.* (2002) 127-129.

[14] T. Masui, K. Fujiwara, K. Machida, G. Adachi, *Chem. Mater.* 9 (1997) 2197-2204.

[15] A. Bumajdad, M. I. Zaki, J. Eastoe, L. Pasupulety, *Langmuir* 20 (2004) 11223-11233.

[16] R. Si, Y. W. Zhang, L. P. You, C. H. Yan, *Angew. Chem., Int. Ed.* 44 (2005) 3256-3260.

[17] H. Gu, M. D. Soucek, *Chem. Mater.* 19 (2007) 1103-1110.

[18] T. Yu, J. Joo, Y. I. Park, T. Hyeon, *Angew. Chem., Int. Ed.* 44 (2005) 7411-7414.

[19] M. Inoue, M. Kimura, T. Inui, *Chem. Commun.* (1999) 957-958.

[20] M. Cargnello, N. L. Wieder, T. Montini, R. J. Gorte, P. Fornasiero, *J. Am. Chem. Soc*. 132 (2009) 1402–1409.

[21] N. L. Wieder, M. Cargnello, K. Bakhmutsky, T. Montini, P. Fornasiero, R. J. Gorte, *J. Phys. Chem. C* 115 (2011) 915–919.

[22] S. Sun, S. Anders, H. F. Hamann, J. U. Thiele, J. E. E. Baglin, T. Thomson, E. E. Fullerton, C. B. Murray, B. D. Terris, *J. Am. Chem. Soc.* 124 (2002) 2884-2885.

[23] R. K. Hailstone, A. G. DiFrancesco, J. G. Leong, T. D. Allston, K. J. Reed, *J. Phys. Chem. C* 113 (2009) 15155-15159.

[24] N. Shukla, C. Liu, P. M. Jones, D. Weller, *J. Magn. Magn. Mater.* 266 (2003) 178-184.

[25] S. Sun, *Adv. Mater.* 18 (2006) 393-403.

[26] F. Zhang, P. Wang, J. Koberstein, S. Khalid, S.-W. Chan, *Surf. Sci.* 563 (2004) 74-82.

[27] T. X. T. Sayle, S. C. Parker, D. C. Sayle, *Phys. Chem. Chem. Phys.* 7 (2005) 2936-2941.

[28] M. Hirano, A. Suda, *J. Am. Ceram. Soc.* 86 (2003) 2209-2211.

[29] B. M. Reddy, P. Saikia, P. Bharali, Y. Yamada, T. Kobayashi, M. Muhler, W. Gru¨nert, *J. Phys. Chem. C* 112 (2008) 16393–16399.

[30] J. Ouyang, H. Yang, *J. Phys. Chem. C* 112 (2009**)** 6921–6928.

[31] S. Kim, R. Merkle, J. Maier, *Surf. Sci.* 549 (2004) 196-202.

[32] N. Hickey, P. Fornasiero, J. Kaspar, M. Graziani, G. Blanco, S. Bernal, *Chem. Commun.* (2000) 357-358.

[33] R. Di Monte, P. Fornasiero, J. Kaspar, M. Graziani, J. M. Gatica, S. Bernal, A. Gomez-Herrero, *Chem. Commun.* (2000) 2167-2168.

[34] J. Z. Shyu, W. H. Weber, H. S. Gandhi, *J. Phys. Chem.* 92 (1988) 4964-4970.

[35] S. Damyanova, C.A. Perez, M. Schmal, J.M.C. Buenoc, *Appl. Catal. A: Gen.* 234 (2002) 271-282.

[36] A. Suda, K. Yamamura, Y. Ukyo, T. Sasaki, H. Sobukawa, T. Tanabe, Y. Nagai, M. Sugiura, *J. Ceram. Soc. Jpn.* 112 (2004) 623-627.

Chapter 6

Controlled synthesis of monodisperse CeO_2 nanoplates and nanorods

Abstract

Surfactant-mediated synthesis of monodisperse CeO_2 nanoplates (15 nm ×50 nm, 2 nm width) was conducted by the thermal decomposition of cerium acetate in 1-octadecene. X-ray diffraction patterns indicated selective (200) plane growth of fluorite cubic CeO_2 in the CeO_2 nanoplates, and transmission electron microscopy revealed that most of the side surfaces exhibited {200} lattice fringes. Smaller amounts of surfactants provided larger nanoplates composed of assemblies of small CeO_2 nanoparticles (NPs). The formation of this polycrystalline structure of assembled NPs is preferable for inducing stability by the decrease of surface energy and positive charge of the NPs. The bandgap energy of CeO_2 nanoplates for direct transitions was larger than that for polyhedral CeO_2 NPs.

Synthesis of CeO_2 nanorods was also carried out by the thermal decomposition of cerium ammonium nitrate in 1-octadecene. The length of CeO_2 nanorods tend to extend from 12 to 47 nm in the addition of larger amount of oleylamine under the constant amount of oleic acid, according to ripening.

1. Introduction

Monodisperse nanostructures of various inorganic materials have recently attracted much attention due to their unique physical properties. Thus, controlled synthesis to obtain uniform size and shape of nanostructures such as nanoparticles (NPs) is a desirable approach for practical applications. Various nanostructures have been known to form, especially in the presence of surfactants [1-3] that inhibit crystal growth of specific planes in the nanostructures, due to their selective attachment to the surface during ripening. Those unique structures have also been obtained by the assembly of small NPs using a bottom-up approach [4-6], where small NPs function as building blocks to provide uniform nanostructures.

Cerium(IV) dioxide (CeO_2) is an important material for solid oxide fuel cells and catalytic applications due to its enhanced capability for oxygen storage and release via the Ce^{4+}/Ce^{3+} redox cycle [7,8]. CeO_2 is also an ultraviolet (UV) absorbent, due to its bandgap energy of ca. 3.2 eV, and has been applied for UV protection of window glass, lenses, and as an additive in cosmetics [9]. In particular, monodisperse CeO_2 NPs has been reported to be useful for selective shielding against harmful UV-B/-C ranges at less than 310 nm [10,11]. A quantum size effect on the bandgap energy has been also reported for CeO_2 NPs [10,12]. A key requirement for those applied optimization processes is control of the nanoscale size and morphology of ceria, which has lead to recent advances in the syntheses of nanostructured ceria with sub-10 nm sizes via hydrothermal [13-17], microemulsion [18,19] and organic phase methods [11,12,20,21]. Especially in organic phase methods, thermal decomposition of metal salts with suitable surfactants is a quite useful method, which easily provides monodisperse metal oxide nanostructures with homogeneous size distribution and consistent morphology [11,21-24]. Metal oxides

nanostructures are formed effectively from the chelated nuclei with surfactants such as carboxylic acids and/or amines in high-boiling organic solvents.

With respect to the morphology control of monodisperse CeO_2 nanostructures, NPs are often discussed; however, the facile synthesis of nanorods [6,24,25,26], nanowires [21], nanosheets [27] and nanoplates [23,24] remains a challenge. Recently, the synthesis of 2-nm-thick CeO_2 nanosheets (two-dimensional structure) with random shapes (>4 μm diameter) in the aqueous phase was reported [27]. Single crystal CeO_2 nanosheet forms as a two-dimensional network of ceria nanocrystals, and the formation of polycrystalline CeO_2 sheets as a precursor has an important role in this synthesis. Such sheet formation by the self assembly of nanocrystals has been also reported [5]. Concerning smaller two-dimensional CeO_2, square nanoplates with 12-15 nm has been obtained by [100] oriented growth using thermal decomposition method, and the effective morphology control by the timely addition of surfactants has been shown [24]. Another recent report on two-dimensional CeO_2 has focused on nanoplate structures with lengths of 80-150 nm [23]. Thus, the synthesis of two-dimensional CeO_2 structures with uniform size and shape and further clarification of their formation mechanism are attracting much attention.

Here the author reports a simple one-step synthesis of monodisperse CeO_2 rectangular nanoplates in an organic solvent system based on the addition of surfactants by thermal decomposition method. Especially, the author focuses on a nanoplate growth mechanism based on assembled NPs by changing the surfactant concentration for two-dimensional morphology control of CeO_2 nanostructures. In this synthesis, polycrystalline CeO_2 nanoplates composed of assembled CeO_2 NPs that selectively exhibit {200} lattice fringes are formed by employing effective surfactants in an organic solvent.

2. Experimental

All chemicals used in the synthesis were purchased from Sigma-Aldrich and were in regular grade of purity.

2.1. Synthesis of CeO_2 nanoplates

$Ce(CH_3COO)_3 \cdot H_2O$ (0.25 mmol), 1-octadecene (95%, 10 mL), oleic acid (OA, 0.3 mmol), and oleylamine (OAm, 0.3 mmol) were magnetically stirred under a N_2 atmosphere. The mixture was heated to 120 °C, and kept for 2 h to dissolve the reagents and remove H_2O from cerium acetate. The solution was then refluxed at 310 °C for 1 h. The solution was exposed to air for 1 h after cooling to room temperature. It was then centrifuged at 8000 rpm for 8 min with isopropyl alcohol in order to separate the formed nanoplates. The precipitate obtained after centrifugation was redispersed in 10 mL of hexane.

Control experiments in the presence of an excess amount of surfactants were carried out using the same synthesis method. The ratios of OA/OAm for the control experiments were 0.45 /0.45 mmol and 0.9 /0.9 mmol for the conformation of nanoplates. A control experiment for a longer reflux time of 3 h during synthesis was also carried out using the same reagents and conditions as that for the nanoplate synthesis. Another control experiment with a decreased amount of OA was performed with OA/OAm = 0.15 /0.3 mmol for the conformation of a two-dimensional nanostructure.

Reference CeO_2 NPs for UV-vis absorption experiments were prepared according to the synthesis of 6-nm CeO_2 NPs [26].

2.2. Synthesis of CeO_2 NRs

$(NH_3)_2Ce(NO_3)_6$ (0.5 mmol), 1-octadecene (90 %, 10 mL), OA (0.75 mmol), and OAm (1.5 mmol) were mixed under N_2 with magnetic stirring. The reaction conditions and the following work-up procedures were the same as those reported in the synthesis of 4 nm CeO_2 NPs.

In order to check the effect of OAm amount on CeO_2 nanorod length, 1.2, 1.8, and 2.1 mmol of OAm were added to the solution under the constant amount of OA (1.5 mmol). All synthesis was carried out based on the same synthesis method as that of the standard CeO_2 nanorods.

2.3. Characterization of CeO_2 nanostructures

CeO_2 nanostructures were characterized using transmission electron microscopy (TEM), high resolution TEM (HRTEM), X-ray diffraction (XRD) and UV-vis absorption spectroscopy.

TEM samples were prepared by depositing one drop of the diluted sample dispersed in hexane on an amorphous carbon coated copper grid. TEM images were obtained using a Philips EM 420 (120 kV). HRTEM analysis was conducted using a JEOL 2010 TEM (200 kV). The statistical size of the nanoplates was calculated based on 20 randomly selected NPs in the TEM images, and is presented as a combination of the mean value and standard deviation.

The crystal structure was characterized using XRD (Bruker AXS D8) with Cu Kα radiation (λ=1.5418 Å).

UV-vis absorption spectra of CeO_2 nanostructures in hexane were measured with a Perkin Elmer Lambda 35 spectrometer using a quartz cell with a 1-cm path length. The bandgap energy was calculated based on the obtained absorption spectra in the

following manner. The optical absorption coefficient α is obtained by the following equation [18]:

$$\alpha = (2.303\times10^{3} A\rho)/lC, \quad (1)$$

where A is the absorbance of a sample, ρ is the density of CeO_2 (7.28 g cm^{-3}), C is the loading of particles (g L^{-1}), and l is the path length of the cell;

The optical absorption coefficient α near the absorption edge is given by the following relation [18]:

$$\alpha \propto (hv\text{-}E_d)^{1/2}/hv, \quad (2)$$

where hv is the photon energy and E_d is the bandgap energy for direct transition. E_d for the samples was determined from plots of $(\alpha hv)^2$ as a function of photon energy;[18] the intersection of a linear extrapolation of the plot with zero $(\alpha hv)^2$ provided the bandgap energy for direct transition.

3. Results and discussion

3.1. Synthesis and characterization of CeO_2 nanoplates

Monodisperse CeO_2 nanoplates were successfully synthesized by mixing $Ce(CH_3COO)_3$, OA and OAm in 1-octadecene, and heating at 310 °C for 1 h using thermal decomposition method. OA and OAm were added as surfactants and the mole ratio of Ce/OAm/OA was 1:1.2:1.2. Heating in 1-octadecene at a reflux temperature of 310 °C is favorable for this synthesis, because nanoplate formation did not reach the threshold at lower reflux temperatures. Moreover, other organic solvents, such as phenyl ether or benzyl ether, or other Ce(III) or Ce(IV) salts, did not result in nanoplate

formation, which indicates that this synthesis is sensitive to the solvent conditions and precursor salts.

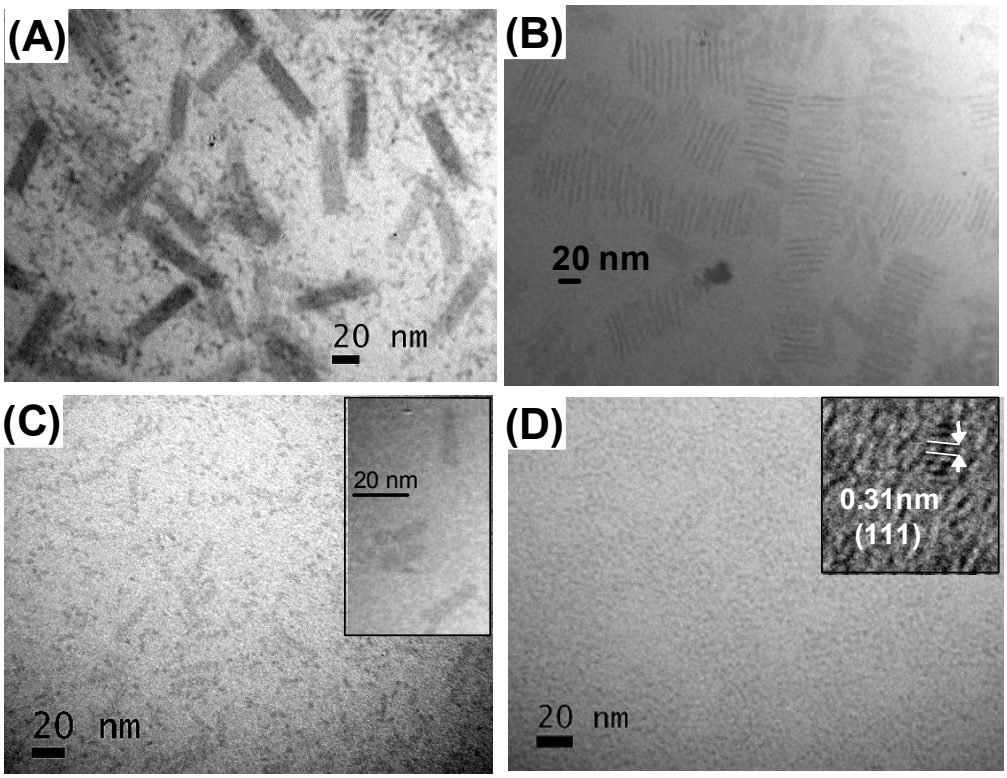

Fig. 1. TEM images of (A) 15 nm×50 nm CeO_2 nanoplates synthesized using 0.3/0.3 mmol of OA/OAm, (B) nanoarray of 15 nm×50 nm CeO_2 nanoplates, (C) CeO_2 nanostructure synthesized using 0.45/0.45 mmol of OA/OAm (inset: enlarged image of front surface of nanoplates), (D) CeO_2 nanostructure synthesized using 0.9/0.9 mmol of OA/OAm (inset: HRTEM images of CeO_2 NPs).

A TEM image of the CeO_2 nanoplates is shown in Fig. 1A. 15 nm×50 nm rectangular nanoplates were obtained in a monodisperse state. These nanoplates formed self-assembled nanoarrays, showing their long side surfaces (Fig. 1B) or short side surfaces. The width of the side surface is ca. 2 nm, and measurement of 20 nanoplates gives a statistical length of 51.7±3.2 nm. The reason for this uniform morphology may be due to synthesis in a non-polar organic solvent with the combination of effective surfactants, which could lead to accurate morphology control relative to the polar solvent. Another important factor for the nanoplate formation may be the synthesis under N_2 atmosphere. The control experiment under air atmosphere resulted in the failure of CeO_2 nanoplate formation, and brought only aggregated precipitation without morphology control provably due to the rapid oxidation. Therefore, mild and slow oxidation from Ce^{3+} to Ce^{4+} by chelating surfactants is preferable for the CeO_2 nuclei formation in this synthesis.

An excess amount of surfactants did not result in good CeO_2 nanoplate formation. Figure 1C shows the CeO_2 nanostructure under the condition of Ce/OAm/OA = 1:1.8:1.8 (mole ratio), which contained 1.5 times the amount of surfactants than that used in the synthesis of the 15 nm×50 nm CeO_2 nanoplates. Smaller CeO_2 nanoplates (ca. 25 nm long) and NPs were observed, but NPs become the dominant species with increased surfactants and the self-assembled nanoplate arrays were rarely observed. A mole ratio of Ce/OAm/OA = 1:3.6:3.6 resulted in only CeO_2 NP (3-nm diameter) formation (Fig. 1D). Therefore, a smaller amount of surfactants selectively provides larger nanoplates by this synthesis method.

HRTEM images of the side surfaces of the CeO_2 nanoplates are shown in Fig. 2A. The side surface exhibits {200} lattice fringes with an interplanar distance of 0.27 nm, which corresponds to the cubic fluorite structure. Figure 2B shows HRTEM images of the

nanoplate front surface. The nanoplate is a polycrystalline structure with crystal domains approximately 2 nm in size, due to the assembly of small sized NPs as building blocks. These NPs appear to be randomly orientated in the front surface of the nanoplate. Furthermore, Fig. 2C shows that some side surfaces of nanoplates are also composed of randomly oriented polycrystalline domains exhibiting {200} lattice fringes.

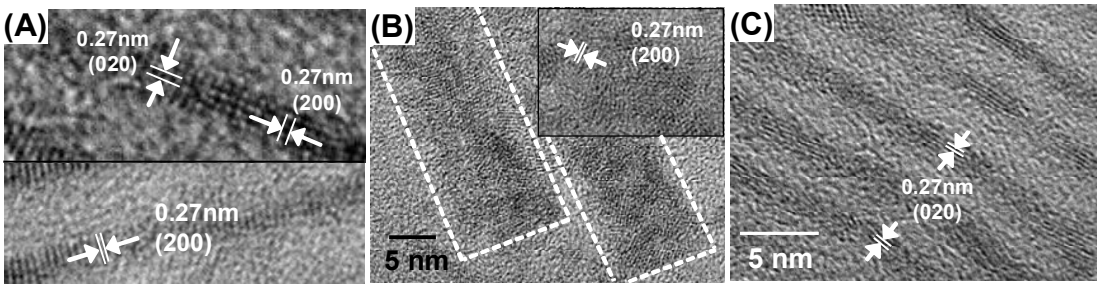

Fig. 2. HRTEM images of 15 nm×50 nm CeO_2 nanoplates: (A) side surface, (B) front surface, and (C) side surface with assembled nanocrystals.

XRD patterns of CeO_2 nanoplates are shown in Fig. 3A for confirmation of the crystal structures. The CeO_2 nanoplates were identified as having a cubic fluorite structure and exhibited clear peaks due to (200) and (220) planes (Fig. 3A), which indicates that selective diffraction of oriented crystals occurs on these planes. The peak growth is specific to the CeO_2 nanoplate structure, and became smaller with increased surfactants (Fig. 3B, Ce/OAm/OA = 1:1.8:1.8 (mole ratio)), although no specific peak growth was detected in the CeO_2 nanostructures synthesized with a large excess amount of surfactants (Fig. 3C, Ce/OAm/OA = 1:3.6:3.6 (mole ratio)). This result corresponds to the presence of {200} lattice fringes in HRTEM images of the front and side surfaces of the CeO_2 the nanoplates.

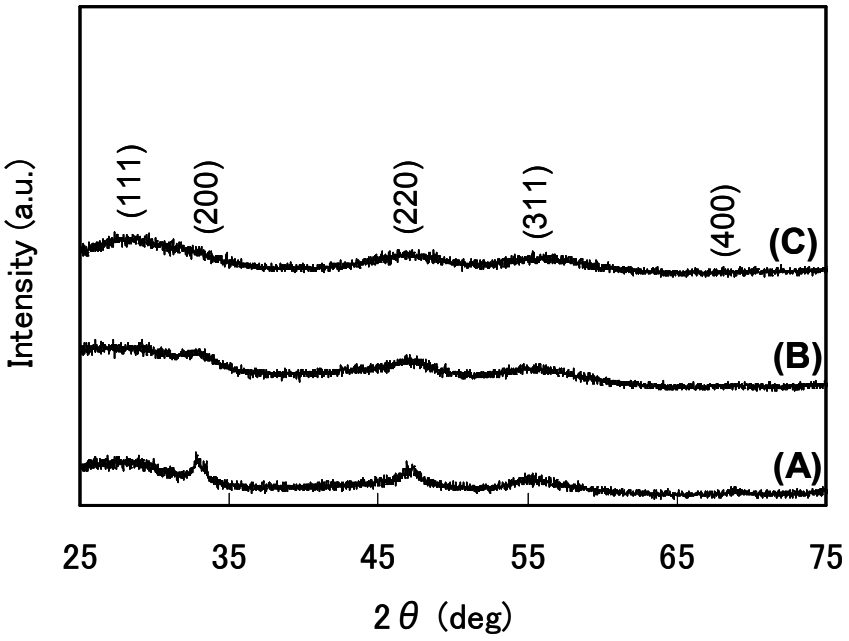

Fig. 3. XRD patterns of (A) 15 nm×50 nm CeO_2 nanoplates synthesized using 0.3/0.3 mmol of OA/OAm, (B) CeO_2 nanostructure synthesized using 0.45/0.45 mmol of OA/OAm, and (C) CeO_2 nanostructure synthesized using 0.9/0.9 mmol of OA/OAm.

In order to evaluate the stability of the nanoplates produced during synthesis, the reflux time was extended from 1 to 3 h. Figure 4 shows a TEM image of the sample refluxed for 3 h. The shape and monodispersity of the CeO_2 nanoplates were almost maintained, even after the long reflux, which indicates that the nanoplates are stable and are not an intermediate species for other unique formations.

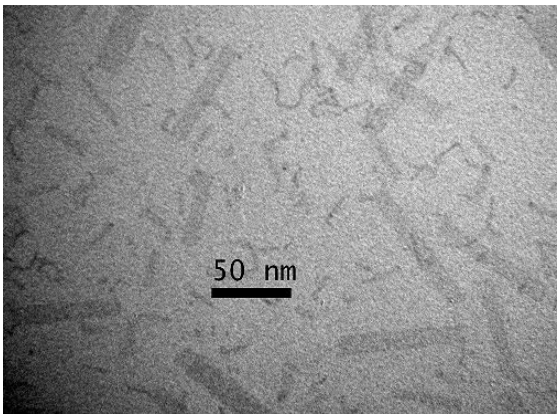

Fig. 4. 15 nm×50 nm CeO_2 nanoplates heated at 310 ºC for 3 h.

3.2. UV absorption analysis and bandgap energy

CeO_2 exhibits a characteristic absorption in the UV region due to the charge transfer transition from O 2p to Ce 4f. The absorption of CeO_2 nanoplates was analyzed and compared with that of 6-nm polyhedral CeO_2 NPs [26] and the results are shown in Fig. 5A. Both spectra exhibit an absorption around the UV region due to charge transfer, and a blue-shift of the absorption edge around 400 nm was observed for the CeO_2 nanoplate solution compared with the edge for the CeO_2 NP solution.

The bandgap energy of this charge transfer was calculated based on UV-vis spectra to help clarify the CeO_2 nanostructure properties. The relationship between $(\alpha h\nu)^2$ and the photon energy calculated based on the UV-vis absorption spectra is shown in Fig. 5B. From the edge of the extrapolated absorption slope shown in Fig. 5B, the direct bandgap energy of CeO_2 nanoplates is ca. 3.47 eV, which is larger than that for 6-nm CeO_2 NPs (3.32 eV). The bandgap energy of bulk CeO_2 is ca. 3.2 eV [27]; therefore, both monodisperse nanostructures exhibit larger bandgap energies than the bulk sample. This

phenomenon is thought to be due to the NP size and thickness of the sheet-like structures. A quantum size effect has been reported for CeO_2 particles, similar to that for TiO_2, and smaller NPs often exhibit a larger bandgap energy, which is significantly enhanced for NPs with sizes of less than 3 nm [11,12,28]. With respect to sheet-like structures, an increase in the bandgap energy has also been reported for very thin CeO_2 films [29,30] and CeO_2 nanosheets [27], regardless of their total surface size. The thickness of the synthesized nanoplates led to the increased bandgap energy, although the value obtained in this experiment is slightly smaller than other cases [11,27]. This property is promising for applications of CeO_2 nanoplates in the field of UV light shielding as an absorbent due to the large bandgap energy.

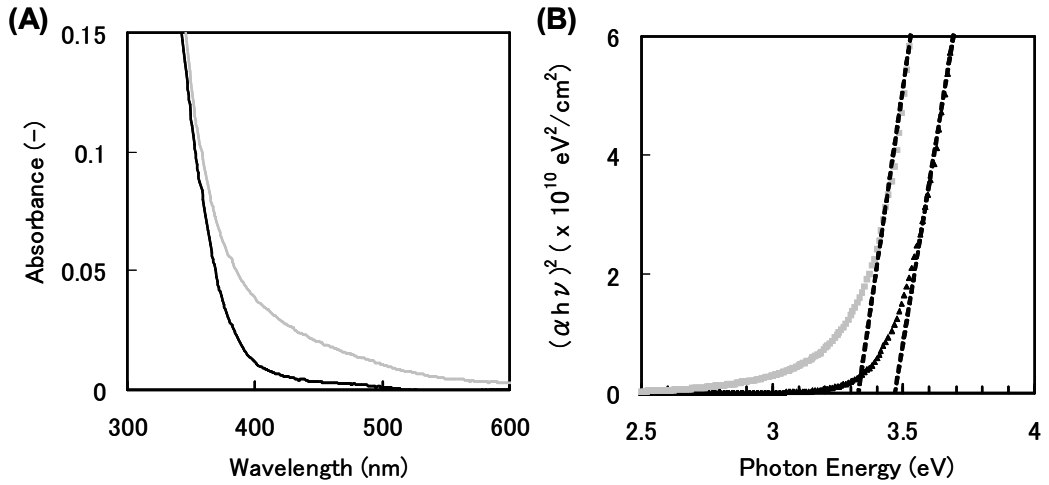

Fig. 5. (A) UV-vis absorbance spectra, and (B) $(\alpha h\nu)^2$ as a function of photon energy for CeO_2 nanoplates and 6-nm CeO_2 NPs.

3.3. Mechanism for nanoplate formation.

Considering the formation of a CeO_2 nanoplate as an assembly of small CeO_2 NPs, the dependency of nanoplate formation on the amount of surfactants is explained by the following formation steps. Firstly, 2-nm NPs are synthesized as nuclei and simultaneously assemble to form nanoplates in order to minimize their surface energy, depending on the amount of surfactants present. In the presence of a small amount of surfactants, the monodispersity of the CeO_2 NPs is unstable and they tend to assemble with each other, which may be facilitated by surface hydroxyls, to maintain the balance between the amount of surfactants and the surface energy (Scheme 1A). Therefore, a smaller amount of surfactants is thought to provide larger CeO_2 nanoplates, as shown in Fig. 1.

In terms of the selective plane formation, (100) planes in NPs seem to be formed selectively with a small amount of surfactants, probably due to selective adsorption of surfactants on the {100} surface and subsequent formation of the {100} surface caused by the low growth rate in the [100]. Carboxylic groups have been known to stably absorb on the CeO_2 {100} surface [31]. which leads to the selective (100) plane formation by OA.[24] Therefore, OA plays an important role for this selective plane formation. However, selective crystal growth and assembly do not occur with the addition of a large amount of surfactants, because all facets are randomly covered with excess surfactants [32], which results in the synthesis of only monodisperse polyhedral CeO_2 NPs (Scheme 1B). Thus, the amount of surfactants also effects the selective crystal growth and plane formation during synthesis, which could be exploited to achieve morphology control.

If the decrease in surface energy is the only decisive factor for the assembled formation, three-dimensional or random aggregation should also occur at the same time; however, no such structures were observed, which implies the presence of an additional

factor. The charge of the NPs may also have an influence on nanoplate formation. It has been reported that electrostatic interaction influences the anisotropy of NP interaction, and positively charged NPs tend to form sheet-like structures, from both experimental and theoretical studies [33]. The addition of half the amount of OA (Ce/OAm/OA = 1:1.2:0.6 (mole ratio)), where NPs are positively charged due to the excess amine groups from OAm, still resulted in nanoplate/nanosheet formation, although their size was not uniform and monodispersity was absent (Fig. 6). Therefore, the presence of OAm is also one of the necessary factors for nanoplate formation without random three-dimensional aggregation. This formation mechanism may be applied not only to this case, but also to other similar CeO_2 two-dimensional structures. Moreover, this unique nanostructure could lead to catalyst applications due to the selective (100) plane formation and UV absorbent properties due to the plate structure, in addition to use as precursors for the formation of higher-order structures such as nanotubes [34].

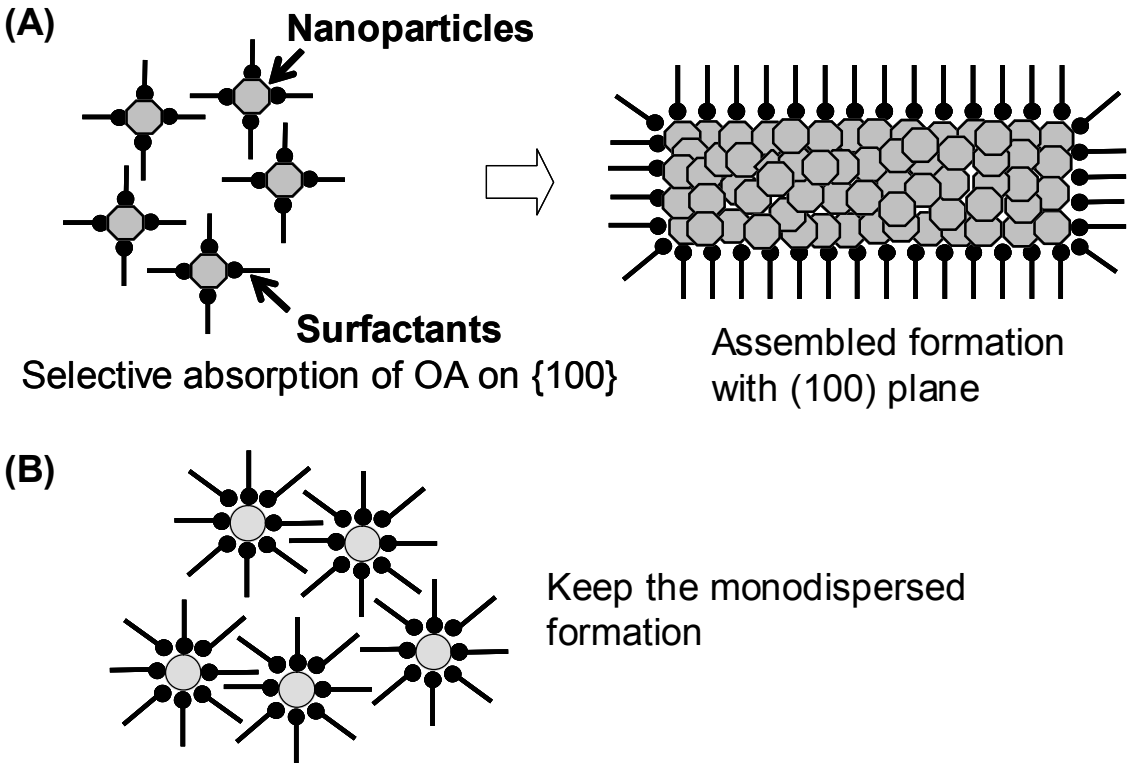

Scheme 1. Schematic illustrations of CeO_2 nanostructure growth under conditions of (A) a small amount of surfactants (nanoplate formation) and (B) a large amount of surfactants (NP formation).

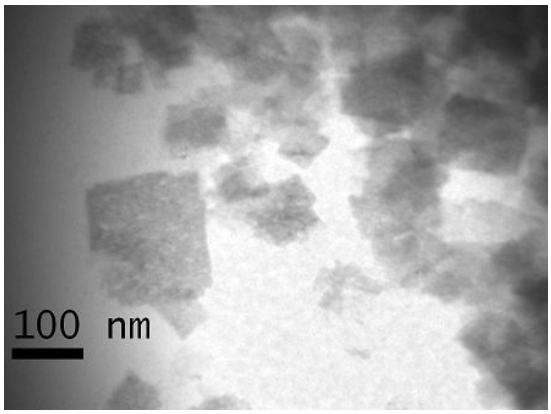

Fig. 6. CeO_2 nanostructure synthesized using 0.15/0.3 mmol of OA/OAm.

3.4. Synthesis and characterization of CeO_2 nanorods

Monodisperse CeO_2 nanorods were also synthesized by mixing $(NH_3)_2Ce(NO_3)_6$, OA and OAm in 1-octadecene in the same procedure as in the NP synthesis. OA and OAm were added as surfactants, and the mole ratio of Ce/OAm/OA was controlled to be 1/3/1.5. Although the reduced usage of OAm caused CeO_2 NPs to grow into irregular shapes, the addition of small amount of OA in the reaction mixture helped the consistent nanorod formation. Figure 7A shows the TEM image of the CeO_2 nanorods. Thin CeO_2 nanorods with 2 nm in diameter and 18 nm in length were obtained. HRTEM image of a representative nanorod (Fig. 7B) reveals that this nanorod is composed of {200} lattice fringes with interplanar distance of 0.27 nm, corresponding to the fluorite cubic CeO_2. The fluorite cubic structure of the CeO_2 nanorods was further confirmed by XRD (Fig. 8A).

In order to clarify the CeO_2 nanorods formation mechanism, the change of aspect ratio depending on OAm amount was investigated. In the addition of smaller amount of OAm, 12 nm nanorod was formed under the mole ratio of Ce/OAm/OA = 1/2.4/1.5 (Fig. 7C). On the other hand, 33 and 47 nm nanorods were obtained in the mole ratio of Ce/OAm/OA = 1/3.6/1.5 and 1/4.2/1.5, respectively (Fig. 7D and 7E). Diameter of these nanorods is identical to the standard 18 nm CeO_2 nanorod in all conditions. The number of CeO_2 nanoparticles as a byproduct was increased with the increase of the OAm amount. Figure 8 shows the XRD patterns of a variety of CeO_2 nanorods. All nanorods are identified as fluorite cubic CeO_2, and the increased peak intensity due to the crystal growth was observed with the increase of nanorod length [35].

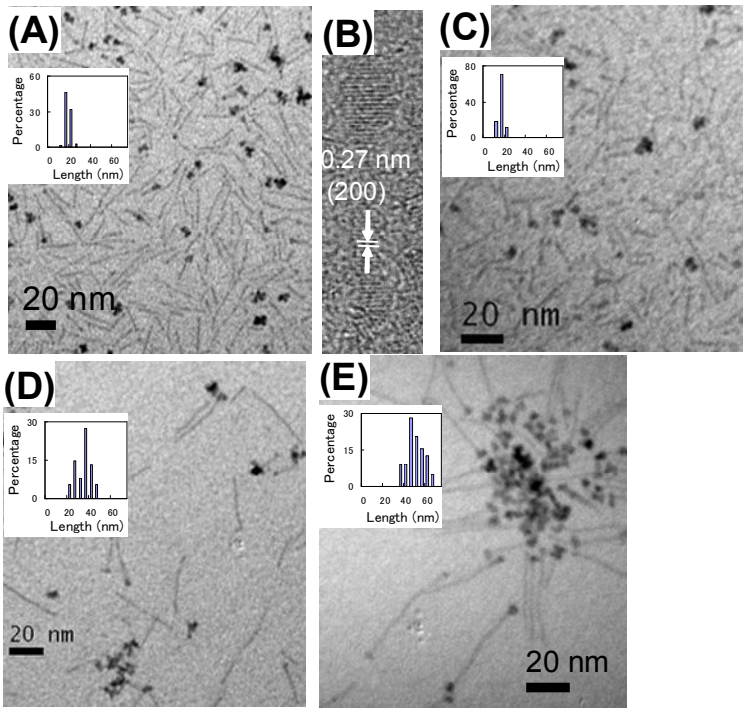

Fig. 7. (A) TEM image of 18 nm CeO_2 nanorods. Inset: histogram of the nanorod length distribution. (B) HR-TEM image of a representative 18 nm CeO_2 nanorod; TEM images of (C) 12 nm, (D) 33 nm and (E) 47 nm CeO_2 nanorods.

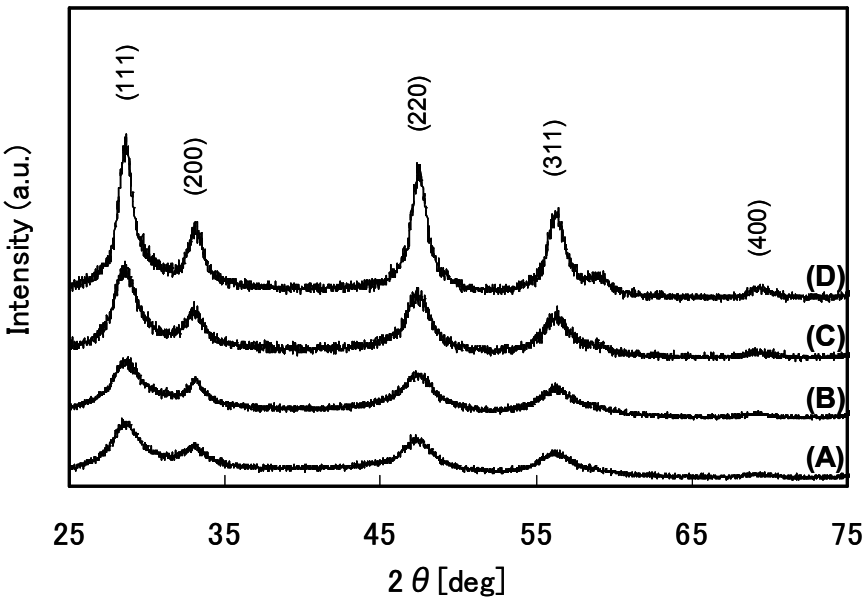

Fig. 8. XRD patterns of (A) 12 nm, (B) 18 nm, (C) 33 nm, and (D) 47 nm CeO_2 nanorods.

The relationships between the aspect ratio and OAm amount is demonstrated in Fig. 9. The aspect ratio of nanorod is just proportional to the amount of OAm. The effect of OA on CeO_2 nanorod morphology was also surveyed, but increase and decrease of OA amount resulted in the failure of nanorod formation. The mole ratio of Ce/OA = 1/1.5 provides the CeO_2 nanorods in the presence of OAm selectively. On the other hand, only OAm addition as a surfactant into $(NH_3)_2Ce(NO_3)_6$ in 1-octadecene has been found to result in polyhedron CeO_2 nanoparticle formation due to the random attachment to nuclei surface. Therefore, a specific amount of OA addition is indispensable for CeO_2 nanorod formation in this synthesis.

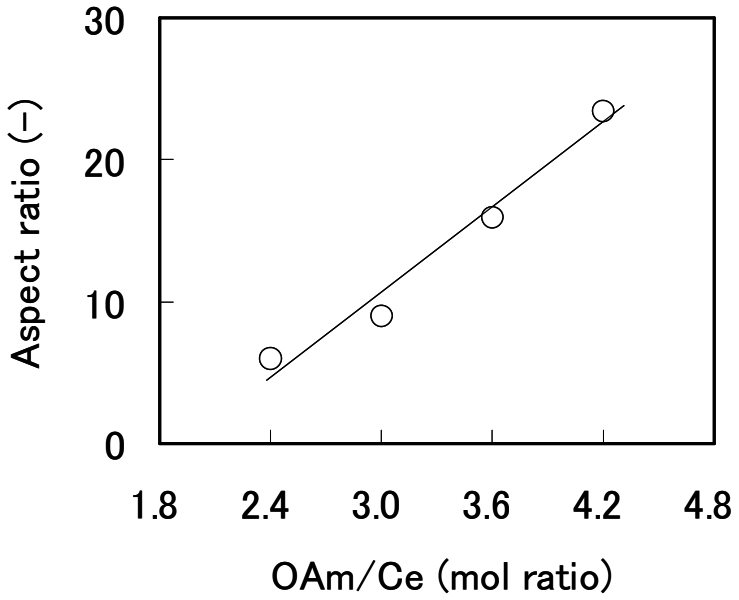

Fig. 9. Aspect ratio of nanorods as a function of OAm/Ce mol ratio.

3.5. Mechanism for nanorod formation.

Judging from the results mentioned above, surfactant condition is a main factor for the control of CeO_2 nanorod morphology. In this study, the width of CeO_2 nanorod is identical, regardless of OAm amount. The binding between OA and Ce-ion may facilitate nucleation of the nanorods, and the width of primary nanorod nuclei, which is almost 2 nm, is dependent on the presence of OA. On the other hand, the stability of long side surface will be increased with the increase of OAm amount. Moreover, the amount of surfactants covering the both ends of nanorod is smaller than that covering the side surface [36]. These factors facilitate the crystal growth along [100] direction, and result in the increase of nanorod length during ripening.

4. Conclusions

Monodisperse CeO_2 nanoplates, composed of assembled CeO_2 NPs, were synthesized by the thermal decomposition of cerium acetate with OA and OAm in 1-octadecene. The nanoplates are polycrystalline and exhibit {200} lattice fringes in HRTEM images. The dependence of nanoplate formation of NP assembled structures on the surfactant conditions may be a result of the decrease in the surface energy of the NPs and the increase in positively charged NPs. The bandgap energy of CeO_2 nanoplates for direct transitions was calculated from the UV-vis absorption spectra and was larger than that for polyhedral CeO_2 NPs.

CeO_2 nanorods were also obtained by the thermal decomposition of $(NH_3)_2Ce(NO_3)_6$ with OA and OAm in 1-octadecene, and the length was controlled by the amount of OAm. Nanorod crystal growth was observed with the increase of OAm amount due to the covering of OAm over the long side surface.

These unique CeO_2 nanostructures with controlled morphology will be promising materials for CeO_2 nanostructure applications.

ACKNOWLEDGMENT. The author thanks Mr. Anthony McCormick for assistance with the HR-TEM analysis.

References

[1] L. Qingsheng, Z. Yan, N. L. Henderson, J. C. Bauer, D. W. Goodman, J. D. Batteas, R. E. Schaak, *J. Am. Chem. Soc.* 131 (2009) 5720-5721.

[2] V. F. Puntes, D. Zanchet, C. K. Erdonmez, A. P. Alivisatos, *J. Am. Chem. Soc*. 124, (2002) 12874-12880.

[3] Y. C. Cao, *J. Am. Chem. Soc*. 126 (2004) 7456-7457.

[4] C. Schliehe, B. H. Juarez, M. Pelletier, S. Jander, D. Greshnykh, M. Nagel, A. Meyer, S. Foerster, A. Kornowski, C. Klinke, H. Weller, *Science* 329 (2010) 550-553.

[5] Z. Tang, Z. Zhang, Y. Wang, S. C. Glotzer, N. A. Kotov, *Science* 314 (2006) 274-278.

[6] S.C. Kuiry, S.D. Patil, S. Deshpande, S. Seal, *J. Phys. Chem. B* 109 (2005) 6936-6939.

[7] S. D. Park, J. M. Vohs, R. J. Gorte, *Nature* 404 (2000) 265-267.

[8] Q. Fu, H. Saltsburg, M. Flytzani-Stephanopoulos, *Science* 301 (2003) 935-938.

[9] Y. Taga, *J. Non-Cryst. Solids.* 218 (1997) 335-341.

[10] S. Tsunekawa, T. Fukuda, A. Kasuya, *J. Appl. Phys.* 87 (2000) 1318-1321.

[11] R. Si, Y. W. Zhang, L. P. You, C. H. Yan, *Angew. Chem., Int. Ed.* 44 (2005) 3256-3260.

[12] M. Inoue, M. Kimura, T. Inui, *Chem. Commun.* (1999) 957-958.

[13] M. Hirano, Y. Fukuda, H. Iwata, Y. Hotta, M. Inagaki, *J. Am. Ceram. Soc.* 83 (2000) 1287-1289.

[14] H. X. Mai, L. D. Sun, Y. W. Zhang, R. Si, W. Feng, H. P. Zhang, H. C. Liu, C. H. Yan, *J. Phys. Chem. B* 109 (2005) 24380-24385.

[15] A. Sehgal, Y. Lalatonne, J.-F. Berret, M. Morvan, *Langmuir* 21 (2005) 9359-9364.

[16] S. Yang, L. Gao, *J. Am. Chem. Soc.* 128 (2006) 9330-9331.

[17] F. Zhang, S. W. Chan, J. E. Spanier, E. Apak, Q. Jin. R. D. Robinson, I. P. Herman,

Appl. Phys. Lett. (2002) 127-129.

[18] T. Masui, K. Fujiwara, K. Machida, G. Adachi, *Chem. Mater.* 9 (1997) 2197-2204.

[19] A. Bumajdad, M. I. Zaki, J. Eastoe, L. Pasupulety, *Langmuir* 20 (2004) 11223-11233.

[20] H. Gu, M. D. Soucek, *Chem. Mater.* 19 (2007) 1103-1110.

[21] T. Yu, J. Joo, Y. I. Park, T. Hyeon, *Angew. Chem., Int. Ed.* 44 (2005) 7411-7414.

[22] S. Sun, *Adv. Mater.* 18 (2006) 393-403.

[23] D. Wang, Y. Kang, V. Doan-Naguen, J. Chen, R. Kungas, N. L. Weider, K. Bakhmutsky, R. J. Gorte, R. J. Murray, *Angew. Chem., Int. Ed.* 50 (2011) 4378-4381.

[24] H. L. Lin, C. Y. Wu, R. K. Chaing, *J. Colloid Interface Sci.* 341 (2010) 12-17.

[25] A. Ahniyaz, Y. Sakamoto, L. Bergstrom, *Cris. Grow. & Design* 8 (2008) 1798-1800.

[26] H. Imagawa, A. Suda, K. Yamamura, S. Sun, *J. Phys. Chem. C* 115 (2011) 1740-1745.

[27] T. Yu, B. Lim, Y. Xia, *Angew. Chem., Int. Ed.* 49 (2010) 4484-4487.

[28] Y. W. Zhang, R. Si, C. S. Liao, C. H. Yan, *J.Phys. Chem. B* 107 (2003) 10159-10167.

[29] K. B. Sundaram, P. Wahid, *Phys. Stat. Sol. B* 161 (1990) K63-K66.

[30] Z. C. Orel. B. Orel, *Phys. Stat. Sol. B* 186 (1994) K33-K36.

[31] J. Stubenrauch, E. Brosha, J. M. Vohs, *Catal. Today* 28 (1996) 431-441.

[32] J. Zhang, S. Ohara, M. Umetsu, T. Naka, Y. Hatakeyama, T. Adschiri, *Adv. Mater.* 19 (2007) 203-206.

[33] Z. Zhang, Z. Tang, N. A. Kotov, S. C. Glotzer, *Nano Lett.* 7 (2007) 1670-1675.

[34] C. Pan, D. Zhang, L. Shi, *J. Solid State Chem.* 181 (2008) 1298-1306.

[35] N. Du, H. Zhang, B. Chen, X. Ma, D. Yang, *J.Phys. Chem. C* 111 (2007) 12677-12680.

[36] C. Wang, Y. Hou, J. Kim, S. Sun, *Angew. Chem., Int. Ed.* 46 (2007) 6333-6335.

Chapter 7

General Conclusions

The author investigated the synthesis and characterization of metal oxide nanomaterials and their application to automotive catalysts. In this thesis, two new approaches have been accomplished. First, novel nanocomposite of Al_2O_3 and ZrO_2-TiO_2 (AZT) was synthesized and applied to the support for NO_x storage reduction (NSR) catalyst. Second, novel CeO_2 nanostructures were synthesized and applied to the materials with O_2 storage capacity (OSC) for three-way catalyst (TWC).

In Part 1, synthesis and characterization of AZT was demonstrated. As an NSR support, Al_2O_3 is indispensable for thermal stability, and TiO_2 is also required for sulfur durability, which is combined with ZrO_2 as solid solution of ZrO_2-TiO_2 (ZT) in order to improve thermal stability of TiO_2. But conventional support is an only physical mixture of those metal oxides, which is the mixture of secondary particles and causes the limited effects on thermal stability and sulfur durability due to the lack of uniformity. Therefore, homogeneous distribution of metal oxides as a nanocomposite is promising for compensating each negative point and enhancing each advantage. Schematic and transmission electron microscopy (TEM) images for improvements in AZT system are shown in Fig. 1. General synthesis and characterization of AZT was exhibited in Chapter 2. Then, synthesis condition of AZT for thermal stability and clarification of improved NSR performance for sulfur durability based on the analysis of NO_x storage materials were demonstrated in Chapter 3. Finally, the effect of Ti doping to Al_2O_3 in AZT on sulfur stability was shown in Chapter 4. Detailed key points in each section are summarized as follows.

In Chapter 2, the author showed the synthesis of AZT by the coprecipitation method and NOx storage performance using AZT as a NSR catalyst support for thermal stability. The XRD and TEM results revealed that primary particles of γ-Al_2O_3 and ZT coexisted as secondary particles as shown in Fig.1. As one of the characteristic properties, the basicity of AZT was lower than that of the physically mixed oxide, probably due to the presence of TiO_2 in Al_2O_3 particles by canceling the basicity of Al_2O_3. This finding suggests the potential for sulfur durability, leading to the results in Chapter 4. After thermal treatment, aggregation of the ZT particles in AZT was inhibited relative to that in the physical mixture of Al_2O_3 powder and ZT powder, indicating a thermally stable support for NSR catalysts. This was attributed to the diffusion barrier against ZT created by primary Al_2O_3 particles in AZT. Finally, AZT was applied to the support for NSR catalyst. After a thermal aging test, the NSR catalyst containing AZT had a larger NO_x storage capacity than the catalyst containing the physically mixed oxide. This result revealed that AZT as a support is a promising and feasible material for NSR catalysts with thermal stability.

In Chapter 3, the author analyzed NO_x storage materials for the optimization of AZT synthesis and the clarification of the improved NSR performance using Pt/Rh/Ba/K/AZT catalyst. First, the reason why the catalyst containing AZT calcined at 1073 K had a high NO_x storage capacity after thermal aging was investigated in terms of calcination temperature. This enhanced storage capacity was attributed to the fact that ZT was crystallized and stabilized after the calcination at 1073 K, relative to AZT powders calcined at a low temperature. Therefore, AZT prevents potassium from solid-state reaction with TiO_2. As a result, the amount of active potassium in the AZT catalyst is larger than those containing AZT calcined at a low temperature. Second, the mechanism for the excellent NO_x storage performance of AZT catalyst after sulfur aging

compared with the catalyst containing physically mixed Al_2O_3 and ZT was investigated. One reason is that AZT catalysts inhibited the solid phase reaction of potassium with support materials and kept a high ratio of active potassium, which can store NO_x. Another reason is that the ratio of active barium in the AZT catalyst was also larger than that in the catalyst containing physically mixed Al_2O_3 and ZT, because of the low basicity and high Pt dispersion of AZT.

In Chapter 4, the author proposed the validity of Ti-doping to AZT as a support for a NSR catalyst in order to achieve sulfur durability, according to the prospect that TiO_2 in Al_2O_3 decreases the basicity of AZT in Chapter 2. Ti-doped AZT (Ti-AZT) maintained the original structure of AZT after the Ti doping step and exhibited lower basicity. Energy dispersive X-ray spectroscopy revealed that the Ti concentration on the Al_2O_3 particles was more than 10 atom% on average for Ti-AZT containing 3.3 atom% of doped titanium. Doped titanium was homogeneously distributed on the surface without the formation of isolated TiO_2 particles. SO_2-temperature programmed desorption at less than 823 K indicated that the catalyst containing Ti-AZT had larger sulfur desorption than that containing AZT. After sulfur aging tests, the Ti-AZT catalyst provided a large amount of NO_x storage. This is because the inhibition of sulfur adsorption and the promotion of sulfur desorption in the Ti-AZT catalyst, due to the decreased basicity. Therefore, Ti-AZT has acquired improved sulfur durability as well as the maintained thermal stability of the original AZT.

In Part 2, synthesis and characterization of a variety of monodisperse CeO_2 nanostructures were demonstrated for O_2 storage and release materials in TWC. One of the reasons for thermal deterioration of OSC materials is the decrease of the surface due to aggregation and sintering. Therefore, keeping highly dispersed nanoparticles (NPs) of OSC materials on thermally stable materials such as Al_2O_3 is promising structure so as

to inhibit aggregation and sintering by diffusion of OSC materials. For such a purpose, four kinds of monodisperse CeO_2 nanostructures were synthesized by thermal decomposition of cerium salt in organic solutions and shown in Fig. 2. First, different size of CeO_2 NPs were synthesized and applied to the O_2 storage and release reaction in Chapter 5. Second, CeO_2 nanoplates and nanorods were synthesized and characterized in Chapter 6.

In Chapter 5, the author showed monodisperse CeO_2 NPs synthesized by thermal decomposition of ammonium cerium(IV) nitrate in an organic solution with oleylamine (OAm) and/or oleic acid (OA) as surfactants. The 4 nm CeO_2 NPs were synthesized in diphenyl ether with OAm and OA, and the 6 nm CeO_2 NPs were made in 1-octadecene with OAm. In order to keep dispersed state of NPs on support, these CeO_2 NPs were assembled on γ-Al_2O_3 via polyvinylpyrrolidone and annealed at 773 K under air to remove organic coating. These NPs were well dispersed on Al_2O_3 with keeping the small size even after thermal aging and showed the increased OSC compared to the physical mixture of aggregated CeO_2 and γ-Al_2O_3 powder. Moreover, the sample prepared from 4 nm CeO_2 NPs showed larger OSC than that prepared from 6 nm NPs. Therefore, dispersed CeO_2 NPs is effective for OSC due to their smaller size even after exposed at high temperature.

In Chapter 6, the author demonstrated surfactant mediated synthesis of monodisperse CeO_2 nanoplates and nanorods and discussed their growth mechanisms. First, synthesis of monodisperse CeO_2 nanoplates (15 nm ×50 nm, 2 nm width) was conducted by the thermal decomposition of cerium acetate in 1-octadecene with OA and OAm. XRD patterns indicated selective (200) plane growth of fluorite cubic CeO_2 in the CeO_2 nanoplates, and TEM revealed that most of the side surfaces exhibited {200} lattice fringes. Interestingly, smaller amounts of surfactants provided larger nanoplates

composed of assemblies of small CeO_2 NPs with (100) plane, indicating CeO_2 nanoplates developed from assembled NPs. This polycrystalline structure formation of assembled NPs may be preferable for inducing stability by the decrease of surface energy and positive charge of the NPs. In addition, the bandgap energy of CeO_2 nanoplates for direct transitions was larger than that for polyhedral CeO_2 NPs. Second, CeO_2 nanorods were also obtained by the thermal decomposition of ammonium cerium nitrate in 1-octadecene, and the nanorod length was increased from 12 to 47 nm with the increase of OAm amount according to ripening. OA was indispensable for nanorod formation and OAm was found to control the aspect ratio of nanorods.

In conclusion, the author would like to propose that synthesis and morphology control of metal oxides on the nanoscale is possible to be applied to automotive catalyst components with novel properties and further improvement, through this thesis.

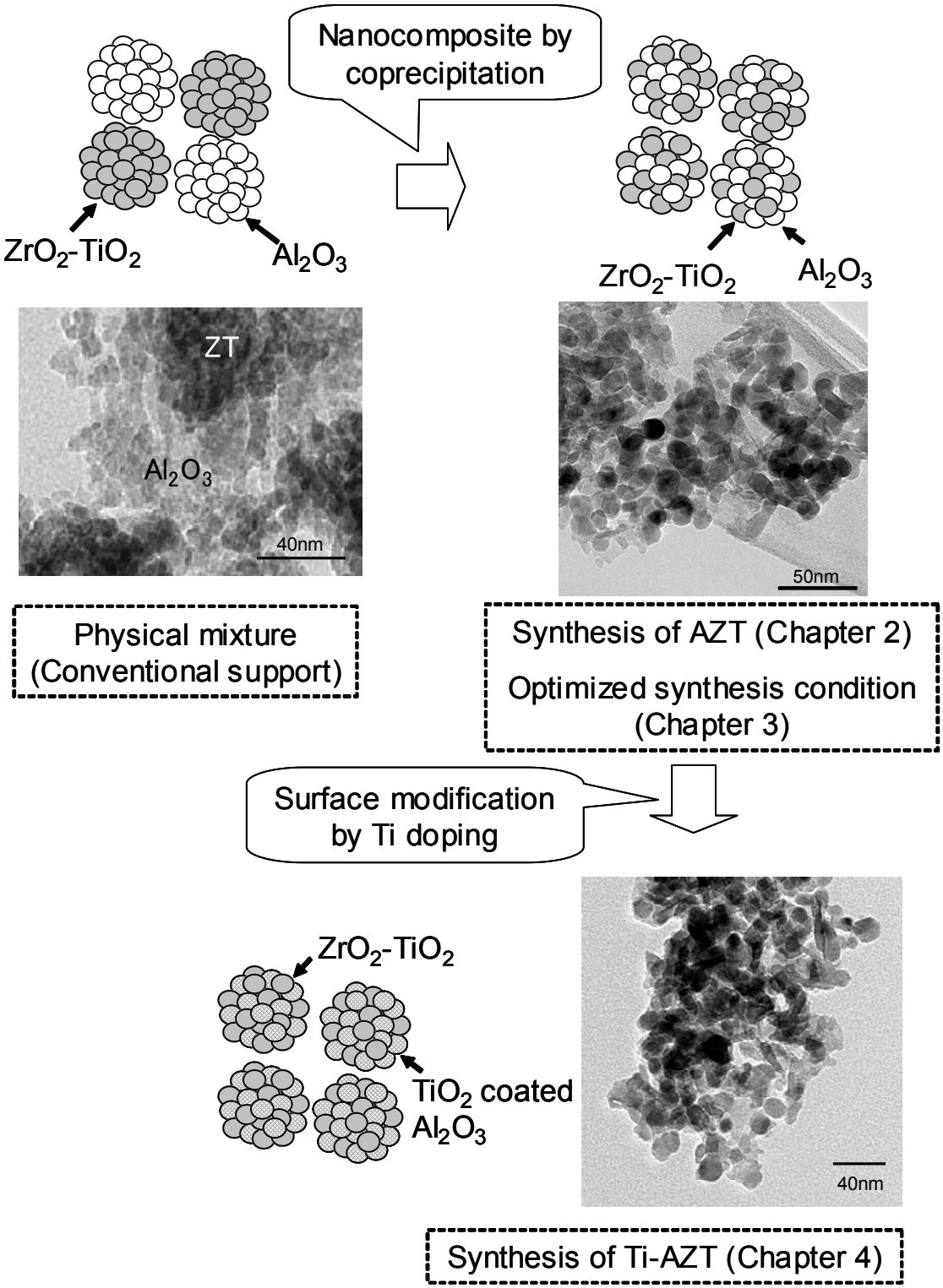

Fig.1. Improvement of Al_2O_3 and ZrO_2-TiO_2 system based on controlled structure.

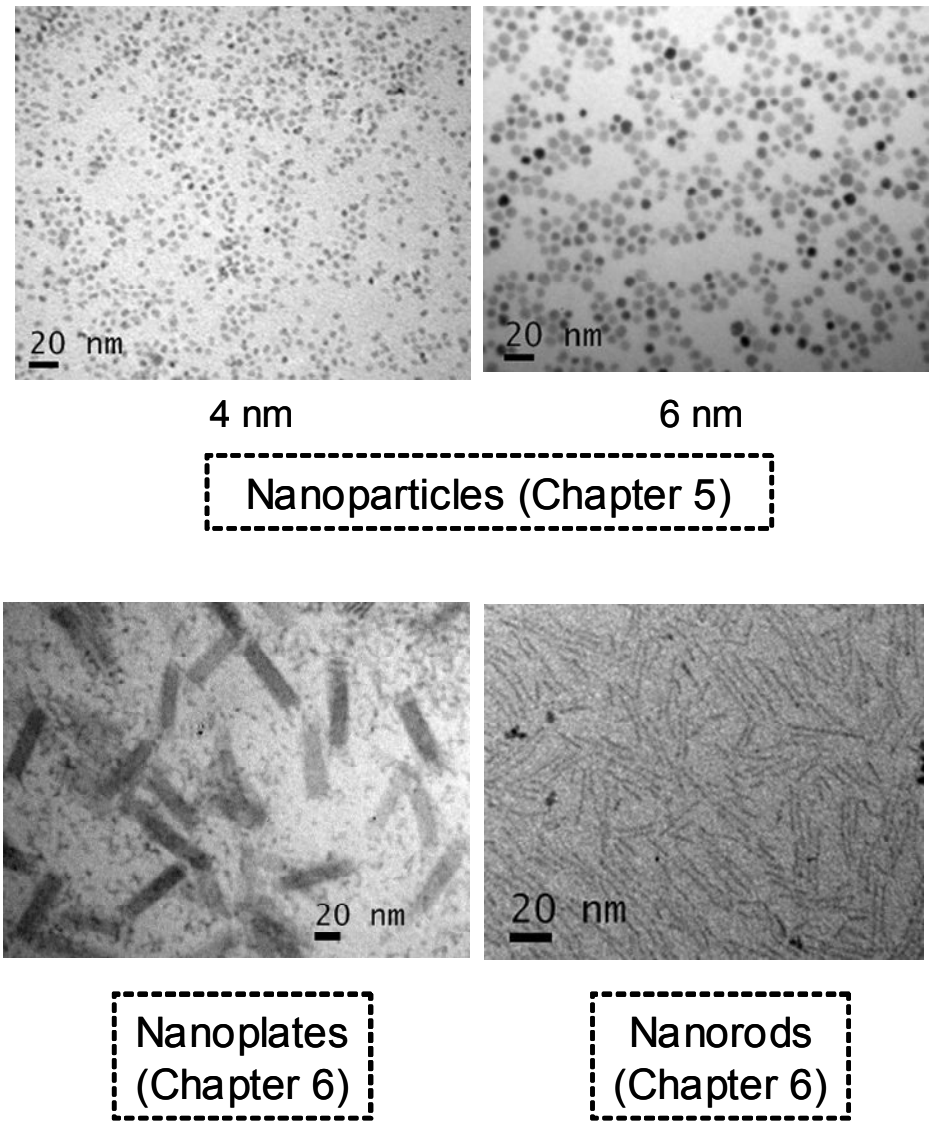

Fig.2. Synthesis of controlled CeO_2 nanostructures by thermal decomposition of Ce salts with surfactants in organic solvents.

List of Publications

Publications Related to Work Described in This Thesis

Part I

Chapter 2:

1. H. Imagawa, T. Tanaka, N. Takahashi, S. Matsunaga, A. Suda, H. Shinjoh, *Journal of Catalysis* 251 (2007) 315-320.

"Synthesis and Characterization of Al_2O_3 and ZrO_2-TiO_2 Nano-Composite as a Support for NO_x Storage-Reduction Catalyst"

Chapter 3:

2. H. Imagawa, N. Takahashi, T. Tanaka, S. Matsunaga, H. Shinjoh, *Applied Catalysis B: Environmental* 92 (2009) 23-29.

"Improved NO_x Storage-Reduction Catalysts Using Al_2O_3 and ZrO_2-TiO_2 Nanocomposite Support for Thermal Stability and Sulfur Durability"

Chapter 4:

3. H. Imagawa, T. Tanaka, N. Takahashi, S. Matsunaga, A. Suda, H. Shinjoh, *Applied Catalysis B: Environmental*, 86 (2009) 63-68.

"Titanium-doped Nanocomposite of Al_2O_3 and ZrO_2–TiO_2 as a Support with High Sulfur Durability for NO_x Storage-Reduction Catalyst"

Part II

Chapter 5:

4. H. Imagawa, A. Suda, K. Yamamura, S. Sun, *The Journal of Physical Chemistry C* 115 (2011) 1740-1745.

"Monodisperse CeO_2 Nanopartcles and Their Oxygen Storage and Release Properties"

Chapter 6:

5. H. Imagawa, S. Sun, *The Journal of Physical Chemistry C* 116 (2012) 2761-2765.

"Controlled Synthesis of Monodisperse CeO_2 Nanoplates Developed from Assembled Nanoparticles"

Publications Not Included in This Thesis

[Original Papers]

1. Y. Yazawa, M. Watanabe, M. Takeuchi, H. Imagawa, T. Tanaka, *SAE Technical Paper* (2007) 2007-01-1056.

"Improvement of NO_x Storage-Reduction Catalyst"

2. H. Imagawa, T. Tanaka, N. Takahashi, S. Matsunaga, A. Suda, H. Shinjoh, *Studies in Surface Science and Catalysis*172 (2007) 609-610.

"Nano-Composite of Al_2O_3 and ZrO_2-TiO_2 Solid Solution as a Support for NO_x Storage-Reduction Catalyst"

[Reviews]

1. N. Takahashi, H. Imagawa, *Journal of the Japan Petroleum Institute* 52 (2009) 90-101.

"Improvement of NO_x Storage and Reduction Catalysts for Gasoline-Fueled Automotive Exhaust"

2. H. Imagawa, *R&D Review of Toyota CRDL* 42 (2011) 63-70.

"Nanocomposite of Al_2O_3 and ZrO_2-TiO_2 as a Support for NO_x Storage-Reduction Catalyst"